Dynamics of electronic order in Magnetoresistive Manganites studied with time-resolved x-ray scattering

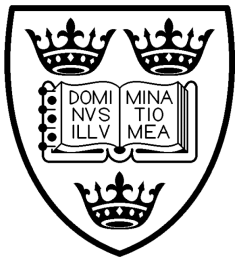

Henri P. Ehrke

Oriel College

University of Oxford

A thesis submitted for the degree of

Doctor of Philosophy

Michaelmas 2010

.

Success is the ability to go from one failure to another with no loss of enthusiasm.

Sir Winston Churchill British politician (1874 - 1965)

Abstract

This thesis presents studies on how photoexcitation disturbs the ordering of the electronic degree of freedom located at the manganese $3d$ orbitals. Throughout the thesis the model compound $La_{0.5}Sr_{1.5}MnO_4$ has been studied. This material exhibits two dimensional ordering of the charges and the orbitals (COO) and at a lower temperature also a three dimensional antiferromagnetic spin order.

In the first approach the sample was photoexcited at 560 nm and the ensuing dynamics was probed through the optical anisotropy at 630 nm. To this end two independent tunable noncollinear optical parameteric amplifiers (NOPA) were used. The cross correlation between them was measured to be 16 fs, much shorter than what previously has been used. The majority of the COO signal at 25 K was found to disappear with a time constant limited by the time-integral of the cross correlation between pump and probe pulse. This hints towards an electrically-driven melting of the COO.

To be more sensitive to the photo-induced changes in the COO, the technique of resonant soft x-ray diffraction was transferred from the static to the time-resolved domain. A diffractometer has been designed, built and comissioned which allows time-resolved experiments on the single-layered manganite $La_{0.5}Sr_{1.5}MnO_4$. In this way it was possible to separate the dynamics of the orbital from the spin ordering by measuring the intensities of the associated diffraction peaks.

The time resolution was as good as 10 ps. On this timescale the orbital peak responded profoundly differently compared to the magnetic ordering peak. It was found that it is possible to melt the magnetic peak completely within the time resolution, while the orbital ordered peak was much less affected. Through calculation and careful comparison with static data a temperature-driven effect could be excluded. Therefore, the experiments suggest that the quenching of the magnetic order is an electrically-driven process.

Role of the author

The ultrafast optical anisotropy measurements in chapter 7 were performed exclusively by the author. The NOPA's used for this measurement were originally built by Thomas Garl at the CFEL facility in Hamburg. Later they were improved by Christian Manzoni and the author.

The x-ray scattering experiment resulted out of a cooperation between the Diamond Light Source and the University of Oxford. Later this cooperation was joined by the University of Hamburg and the Max Planck Group for Structural Dynamics at CFEL. The design and construction of the chamber (chapter 8) was performed by the author under the guidance of Sarnjeet Dhesi. During the assembly process Richard Mott, Helder Marchetto and Stuart Cavill gave assistance. Stuart Cavill was the responsible person for the laser at the Diamond Light Source. The data acquisition for the results presented in Chapter 9 was performed by a multi-national team under the leadership of the author. People involved were: R. I. Tobey, S. Wall, M. Gensch, M. Foerst, S.A. Cavill, S.S. Dhesi, N. Stojanovic, Th. Garl and V. Khanna.

The author thanks the 'Engineering and Physical Science Research Council' (EPSRC) and the Diamond Light Source for primary funding the work for the present thesis. Further support came from the University of Hamburg and the Oriel College Oxford.

Acknowledgment

My time at Oxford University has taught me many lessons, most of them are connected with a person. First and foremost there is my supervisor, Andrea Cavalleri. During my time at the Diamond Light Source he directed my thoughts towards solving the problem, instead of repine over circumstances. A lesson for life. His vision and understanding of science often helped me to circumvent the 'black holes' of understanding that crossed my path. He found the right balance between freedom to pursue own ideas and the guidance not to go astray. I'm indebted and thankful for the opportunity of being his student.

Most of the long nights during beamtimes I spent together with Simon and Ron. First, I valued them as companions at the experiment. Later, I shared many fruitful discussions with, or learned lessons from them. I greatly appreciate your willingness to spend your precious time reading this thesis and to give me critical comments.

At Diamond Light Source I have to thank Sarnjeet Dhesi. Without his experience in static resonant x-ray scattering this work would not have been possible. The fascination about storage rings was revealed to me by Helder and Michael. Without Helders advice and friendship the first year would have been dreadful. Through Michael I gained insight into the operating principle of the inner core of big facilities, the people. My time in Hamburg I shared with Michael and Christian, both furthered my insight into ultrafast optics and laser science.

The group in Oxford gave me support and distraction especially during the weekly Friday night drinks. Other idle time I could spend with friends in Oxford giving me memorable events and making the stay enjoyable. Only to mention one, thanks Nish for going through the last version of the thesis and spotting all the spelling mistakes. All that are left, are due to my last minute changes.

Words do not come close to express the gratitude towards the support of my family. First there is to mention my mother, for being my mother. Then my grandparents,

especially Ralf, who passed away too early. Without his guidance and mental support I would not have been in a position to start this endeavor.

Finally, all this work would have been impossible without Anna, my wife. Her unquestioned support gave me the strength to fight through bad days and the passion to celebrate good ones.

Author's publications

- Transient Electronic Order in Photo-stimulated $La_{0.5}Sr_{1.5}MnO_4$

  H.P. Ehrke, R.I. Tobey, S. Wall, S.A. Cavill, M. Först, V. Khanna, Th. Garl, N. Stojanovic, D. Prabhakaran, A.T. Boothroyd, M. Gensch, A. Mirone, P. Reutler, A. Revcolevschi, S.S. Dhesi and A. Cavalleri

  Submitted for publication in Physical Review Letters

- Coherent Evolution of Mott Excitations Captured on the Time Scale of Electron Correlations

  S. Wall, D. Brida, H.P. Ehrke, S.R. Clark, D. Jaksch, A. Ardavan, S. Bonora, H. Matsusaki, H. Uemura, Y. Takahashi, T. Hasegawa, H. Okamoto, G. Cerullo and A. Cavalleri

  Accepted for publication in Nature Photonics

- Transient electronic structure of the photoinduced phase of $Pr_{0.7}Ca_{0.3}MnO_3$ probed with soft x-ray pulses

  M. Rini, Y. Zhu, S. Wall, R.I. Tobey, H.P. Ehrke, T. Garl, J.W. Freeland, Y. Tomioka, Y. Tokura, A. Cavalleri and R.W. Schoenlein

  Physical Review B 80, 155113 (2009)

- Ultrafast single-shot diffraction imaging of nanoscale dynamics

  A. Barty, S. Boutet, M.J. Bogan, S. Hau-Riege, S. Marchesini, K. Sokolowski-Tinten, N. Stojanovic, R. Tobey, H.P. Ehrke, A. Cavalleri, S. Düsterer, M. Frank, S. Bajt, B.W. Woods, M.M. Seibert, J. Hajdu, R. Treusch and H.N. Chapman

  Nature Photonics 2 415 (2008)

Contents

List of Figures

Chapter 1

Introduction

The central aim of solid state physics is to describe the macroscopic properties of materials, such as the electronic conductivity or the magnetic state, from a microscopic point of view. This is truly a daunting task especially when one considers 10^{23} electrons and nuclei per cm^3! In the absence of exact solutions, many successful approximations have been developed that reduce the complexity of the microscopic interactions. A prime example is the independent electron approximation from Drude and Sommerfeld [1] that explains simple metals. These early approaches led to band theory, where independent electrons occupy predetermined 'states'. Band theory predicts the conduction properties in a wide variety of condensed matter systems and provides the understanding of semiconductors which has driven the electronic revolution and to the widespread use of transistor based devices.

The central theme in the above theories is based on the assumption that the kinetic energy term is the dominating energy scale and that other interactions, like the Coulomb interaction between electrons is weak enough to be included via perturbation theory. These are far reaching approximations, but they carried the understanding so far that some scientist rendered the field of solid state physics mature [2]. Effects that were not understood, like the insulating behaviour of nickel oxides, were attributed

to chemical effects or to sample impurities.

However, there are many materials where these assumptions are invalid. Band theory and the perturbative approach will fail to predict the properties, like in the transition metal oxides. A prototypical example is the discovery of High T_c Superconductivity in 1986 by Bednorz and Mueller [3]. In these strongly correlated electron systems the complex interplay between spin [4], orbital [5], charge, and the lattice degree of freedom leads to exotic and competing phases.

In some of these materials, for example $Pr_{1-x}Ca_xMnO_3$, band theory predicts metallic behaviour but in reality an insulating phase is realised. Switching between these phases is possible by applying an external magnetic field, triggering resistance changes of many orders of magnitude - the colossal magneto resistance effect [4, 6]. This strong sensitivity to external stimuli is a basic characteristic of the strongly correlated electron system. The variety of phases in transition metal oxides makes them candidates to replace conventional semiconductor based devices [7]. However, the lack of real understanding of the microscopic physics inhibits further development. Conventional theories, like band theory, do not reflect the complexity present in these materials, hence new approaches are needed.

One experimental approach to study the complex interplay between the degrees of freedom is to excite one while looking at the response of others. An external stimuli to this end are visible light pulses. A strong 'pump' pulse perturbs the delicate balance and in some cases leads to a phase transition [8, 9, 10]. The evolution of the system can then be mapped by a temporally delayed 'probe' pulse. This time-resolved approach offers the possibility to disentangle the strongly intertwined degrees of freedom on the ultrafast timescale [11].

Currently the technical limits are moving forward in three directions. The first endeavour is to increase the time resolution to the few femtoseconds or, in some cases, the attosecond range [12]. The second goal is towards selective excitation of a single

degree of freedom, for example by using intense Terahertz radiation resonant to a phonon [13, 14]. Finally, different probe techniques are transferred from the static into the time domain. For example changes in lattice structure (using time-resolved hard x-ray diffraction [15, 16]) or maps of the Fermi surface (using time-resolved photoelectron spectroscopy [17]) have been measured after excitation with visible light pulses.

This thesis aims to measure photo-induced changes of the real space ordering of the electronic degrees of freedom using the prototypical compound $La_{0.5}Sr_{1.5}MnO_4$. In this material, the low temperature insulating state exhibits long range ordering of charges, orbital orientations, and spin orientations. By exciting the system with a short laser pulse, the interaction between these degrees of freedom, their dynamics and evolution of the non-equilibrium state can be followed in the time domain. In the present thesis these dynamics are studied from two sides: first the speed of the dynamic is assessed, by measuring changes of the optical anisotropy with a time resolution of a few femtoseconds: then time-resolved resonant soft x-ray diffraction (TR-SXRD) is used to study the dynamics of order located at specific degrees of freedom, here the time resoultion reaches 10 ps.

The thesis is structured as follows: In the next chapter basic concepts of solid state physics are explained which are important in the field of strongly correlated systems. In chapter three the structure of the manganites is presented and concepts are introduced which can be used to predict the magnetic coupling effects and some of the observed ordering phenomena. Chapter four then deals with the mathematical background of resonant x-ray diffraction. In chapter five the compound $La_{0.5}Sr_{1.5}MnO_4$ is explained, this compound is used exclusively throughout the thesis. In chapter 6 a short motivation and explanation of the time-resolved approach prepares the experimental section, which starts with chapter 7. This chapter presents the optical birefringence measurements in the ultrafast time domain. In chapter 8 the TR-SXRD

chamber is presented followed by the highlight of this thesis (chapter 9), the time-resolved resonant x-ray diffraction measurements. Chapter 10 then will summarize the findings and conclude with an outlook.

Chapter 2

Correlation effects in Condensed Matter Physics

2.1 Band theory

Band theory is used to describe the energy states an electron can or can not occupy in a solid. It is tremendously successful in predicting electronic and optical properties of vast classes of materials like metals, semiconductors or insulators. It can be arrived at by either considering free-electrons or a tight-binding picture. Both approaches can give similar results but the former highlights the delocalized, and the later the localized, character of the electron.

Starting in the free-electron picture: electrons are treated as plane waves interacting with the weak periodic potential of the underlying lattice, but not with one another. This leads to a modification of the free-electron dispersion relation, depicted in figure 2.1 (a). This approach is justified when the kinetic energy, given through $E_{kin} = (\hbar k)^2/2m$, is the dominating energy scale and when the electronic wavefunctions have a large extension compared to the lattice spacing. The ground state of the system will be given through a minimum in the kinetic energy leading to the occupa-

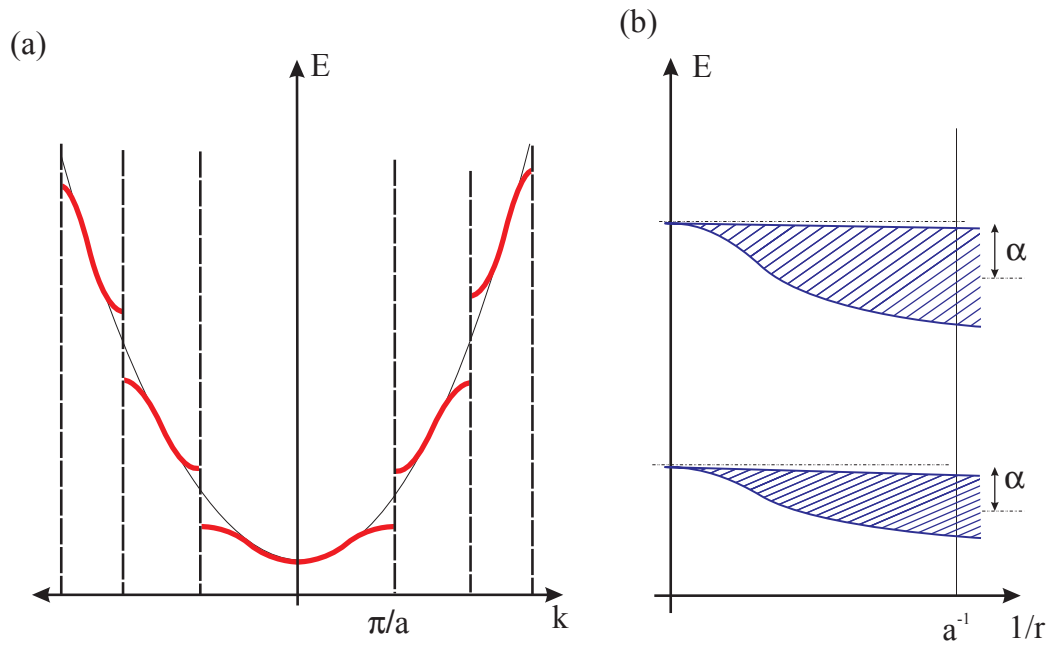

Figure 2.1: (a) Nearly free electron model: Thick red lines show the diversion from the free-electron dispersion curve which arises through interaction with the lattice. (b) Tight binding model: energy bands are formed between the single atom energy levels when the spacing is reduced.

tion of states with a small k vector (i.e. delocalized states). This nearly free-electron approach successfully predicts the properties of simple metals as done by Drude and Sommerfeld.

In other cases, like the transition metal oxides studied here, it can be more appropriate to calculate the band structure starting from the perspective of the isolated atom. In the tight-binding approximation energy bands are formed through hybridisation between neighbouring atomic orbitals (see figure 2.1 (b)). When the hybridisation is strong the formed bands are wide; when it is weak the bands are narrow. For example, different spatial extension of the s- and p- orbitals results in different bandwidths. The atomic orbitals also pass some of their symmetry properties over to the bands. The energy reduction of the band state compared to the atomic energy state (given by α in Figure 2.1 (b)) is due to Coulomb interaction between neighbouring ions.

Once the band structure of a crystal is calculated, electrons occupy the energy

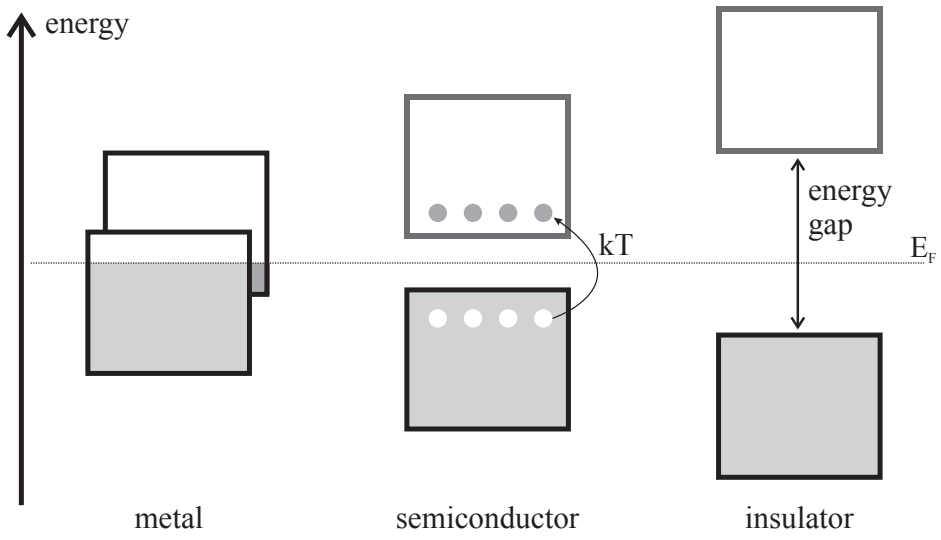

Figure 2.2: Shows a simplified diagram of the electronic band structure of metals, semiconductors and insulators. The Fermi energy E_F separates filled (grey shaded) from unfilled electronic states.

states independent from another up to the Fermi energy (E_F). At zero temperature the Fermi energy is identical to the chemical potential of the electron gas. Depending on the position of the Fermi energy relative to the bands it is possible to classify materials into insulator, semiconductors or metals (see Figure 2.2). When the Fermi energy lies in a band (as is always the case for an uneven number of electrons per unit cell) the application of a DC electric field will allow free propagation of the electrons in the crystal (left picture in 2.2). When the Fermi energy lies between bands, in an 'energy gap' then an applied DC electric field cannot give the electron enough energy to promote it over the gap into free states. The solid is then referred to as an insulator. In between these two scenarios lies the semiconductor. It has a gap small enough so that electrons can be excited thermally into the conduction band, exhibiting an increase in conductivity with temperature. Another way to change the conductivity in a semiconductor is by replacing one element with another one of different valency. In this way free states are induced in the valence band, and can be used to taylor the conductivity very precisely.

Band theory also allows the incorporation of weak correlation between electrons through perturbation theory; as in the description of excitons. This requires the kinetic energy to be the dominating energy scale in the system. If this is not the case other theories have to be used that include the different interactions on an equal footing.

2.2 Correlation effects

In contradiction to band theory, materials with a partially filled $3d$ shells can be insulating [18]. Nickel Oxide for example has a ground state with an unfilled valence d-shell. According to band theory calculations the Fermi energy lies in the middle of a band and, therefore, is expected to be metallic. However, experimentally it is found to be insulating with a very high bandgap of 4.3 eV. This is because the electron-electron interaction in elements with partially filled d-shell is strong. Such strong correlation effects can be illustrated by considering the Wigner crystal [19].

The consideration is based on the interplay between potential and kinetic energy for a varying electron separation a. The potential energy of the electrons can be formulated as $E_P \propto 1/a$. For a large distance between the electrons (i.e. at small density, $n \propto a^{-1/3}$) one might think that the Coulomb interaction between the electrons can be disregarded or approximated as a small perturbation. Taking account of the kinetic energy changes the picture. The kinetic energy of the electrons is given by $E_{kin} = p^2/2m$. Quantum theory states that the momentum depends on the Fermi surface and, therefore, also on the electron density. Using Heisenberg's uncertainty principle the momentum can be written as $p_F \propto \hbar/a$. This results in a kinetic energy of $E_{kin} \propto \hbar^2/(2ma^2)$ which falls off more strongly than the potential energy. Therefore, at low densities the Coulomb interaction leads to electron localization. They form a strongly correlated electron system, the Wigner crystal. Upon decreasing the

electronic separation (increasing the density) the kinetic energy dominates the potential energy and at a critical distance the Wigner crystal melts. This example shows that even in a simple system, strong correlations do occur and are of fundamental importance.

The Mott-Hubbard Model is a simple model which treats the kinetic energy and the electronic Coulomb repulsion equivalently. It was initially formulated by Mott and further investigated by Hubbard [20, 21]. The Mott-Hubbard Hamiltonian has two terms:

$$H = -t \sum c^{+}_{I\sigma} c_{I\sigma} + U \sum n_{\uparrow\sigma} n_{\downarrow\sigma} \tag{2.1}$$

$c^{+}_{I\sigma}/c_{I\sigma}$ is the creation/annihilation operator of the electrons with spin σ, $n_{i,j}$ is the occupancy operator.

The first term describes the kinetic energy of the electrons, as already used implicitly in the tight binding model and describes the tendency of the electrons to delocalize (H_T). It depends mainly on the size of the hopping amplitude which is given as

$$t = \langle \Phi(\underline{r}) | V(\underline{r}) | \Phi(\underline{r} + \underline{a}) \rangle \, . \tag{2.2}$$

Here Φ is the atomic wavefunction and V is the Coulomb potential of the core, $\underline{r}$ is the coordinate of an electron and $\underline{a}$ the distance between nearest neighbours. In the case of a strong overlap between neighbouring wavefunctions the hopping amplitudes will be large. This results in a large bandwidth given by $W = 2nt$ where n is the number of nearest neighbours[1].

The second term describes the on-site electrostatic Coulomb interaction between electrons (H_U), where U gives the energy of the Coulomb repulsion between two electrons on a single site, illustrated in Figure 2.3a.

[1]Bands are formed between atomic orbitals and, due to the Pauli exclusion principle, different orbitals cannot have the same energy. Therefore, the band width linearly increases with the number of interacting neighbours. The factor 2 is because the hopping can occur in either direction.

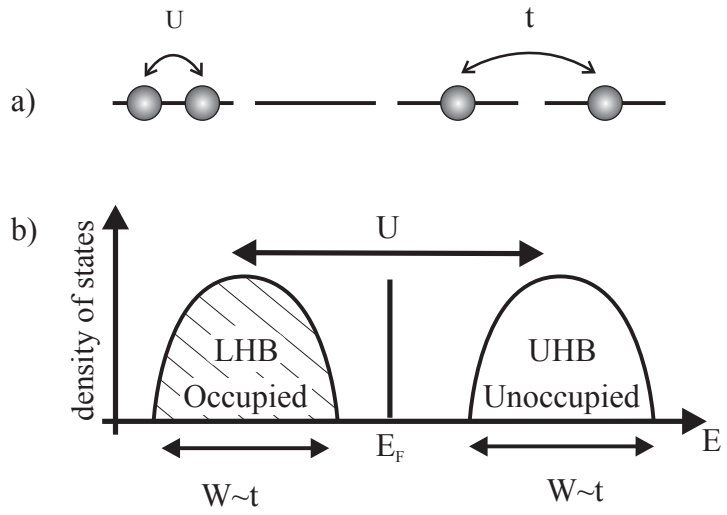

Figure 2.3: Due to the on-site Coulomb interaction U a band is split into two, separated by the energy U. In the case of half filling the lower lying band (lower Hubbard band, LHB) is completely filled while the higher lying one - the upper Hubbard band (UHB) - is empty.

The model has two extreme cases depending on the relative strength of the two energy scales present:

- in the limit of $t \gg U$ this model becomes identical to the tight binding model and describes a system where the electrons are delocalized over the whole crystal
- in the limit $t \ll U$ the electronic Coulomb interaction dominates. If an electron hops between sites it gains the energy t but the double occupancy costs the Coulomb energy U. In a simple model system of one energy level per site and at half filling, e.g. each energy state is only occupied by one electron, the original band splits into two bands separated by the energy U. In Figure 2.3b this scenario is shown, the energetically lower lying Hubbard band is completely filled while the upper Hubbard band is empty. Both bands are separated by an energy gap given by U.

When the hopping amplitude and the electronic Coulomb interaction are of similar strength they competes with one another. Whether a system is insulating or metallic depends on the interplay between t and U and the filling n, see Figure 2.4 for an

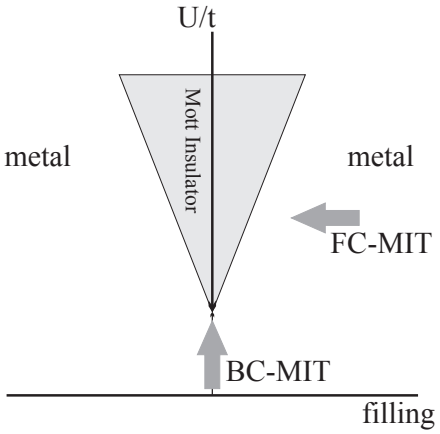

Figure 2.4: Phase diagram of a Mott insulator the ratio U/t is plotted over the filling n. A metal insulator transition (MIT) can either occur through controlling the ratio of U over t (band controlled filling BC) or through a change in the filling (FC) [22].

illustration. It is possible to reach the Mott Insulating region from two distinct directions. In the band controlled (BC) transition, the filling n is held constant and the ratio U/t is varied, like in the Wigner crystal discussed above. On the other hand, the filling can be changed by adding or removing electrons through chemical doping. This is seen as a horizontal cut through the diagram in Figure 2.4 and called filling controlled (FC) transition. Mott insulators have many interesting properties when compared to band insulators. Unlike in band theory, the local spin and orbital degree of freedom of the electron survives as an independent degree of freedom. A common consequence of this is the ordering of charge and orbitals. This ordering is stabilized by complex interactions between the electronic degree of freedom and the lattice. For example electron-phonon or electron-spin interactions can lead to new and very complex phases [5, 23]. These interactions are especially pronounced in transition metal oxides like manganites.

Chapter 3

Introduction to Manganites

Manganites are transition metal oxides with a varying concentration of trivalent and tetravalent manganese ions. Their collective electronic properties are dominated by the d-electrons which are located between the full valence and the empty conduction band of the s and p-orbitals. The wavefunction of the manganese $3d$-orbitals is spatially more confined compared to the s and p-orbitals, limiting the hybridisation with the neighbouring oxygen p-orbitals and resulting in a narrow bandwidth. Furthermore, the bandwidth is so narrow, that correlation effects can lead to the localization of electrons and the creation of novel ground states completely unexpected from a non-interacting electron picture. The different degrees of freedom of the electron (charge, spin and orbital) can form new phases inside the solid, leading to very rich phase diagrams.

Some of these phases occur with similar energy scales and a small external perturbation can favour one phase over the other. For example, a magnetic field can be used to favour a metallic over the preferred insulating phase, as realized in $Pr_{0.6}Ca_{0.4}MnO_3$ shown in figure 3.1. Related to this, insulator-to-metal transition, is a change of resistance of more then nine orders of magnitude, the colossal magneto resistance effect [4]. These 'colossal' changes have generated interest from the data storage and computer

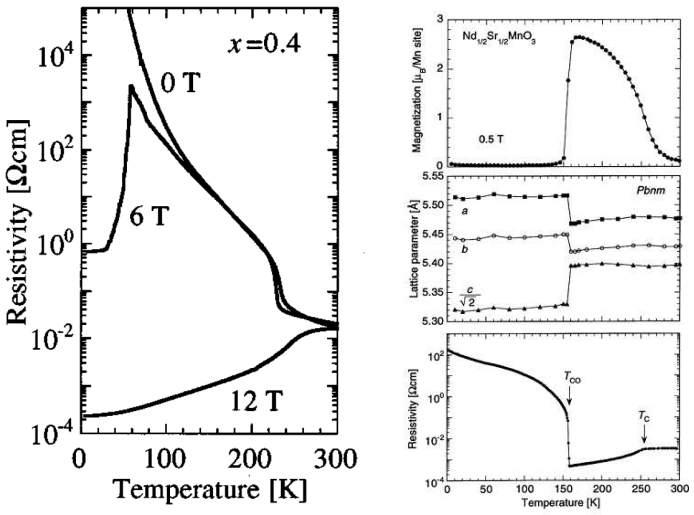

Figure 3.1: Left: Resistivity for the material $Pr_{0.6}Ca_{0.4}MnO_3$ [24]. **Right:** Resistivity, lattice parameter and magnetization for the medium bandwidth system $Nd_{0.5}Sr_{0.5}MnO_3$, from [25]

industry for their potential application as spintronic devices.

In the following sections the electronic and crystal structure of the manganites will be explained.

3.1 Crystallographic and electronic structure

The manganites are represented using the perovskite $AMnO_3$ structure. The perovskite A-site is occupied by a mixture of trivalent rare earth (RE) ions such as La, Pr, Nd and divalent alkaline earth (AE) ions such as Sr, Ca, Ba and can be written as $A=RE_{1-x}AE_x$. By controlling the parameter x it is possible to form a solid state solution composed of Mn^{3+} and Mn^{4+} over a wide doping range.

The geometrical structure can be described using a cube with the A-site ions occupying the corners while the manganese ions are located in the centre. The oxygen ions are situated in the face-centred positions, forming an octahedra around the manganese ions, see figure 3.2.

Alternatively, the perovskite structure can be described as a system of alternating

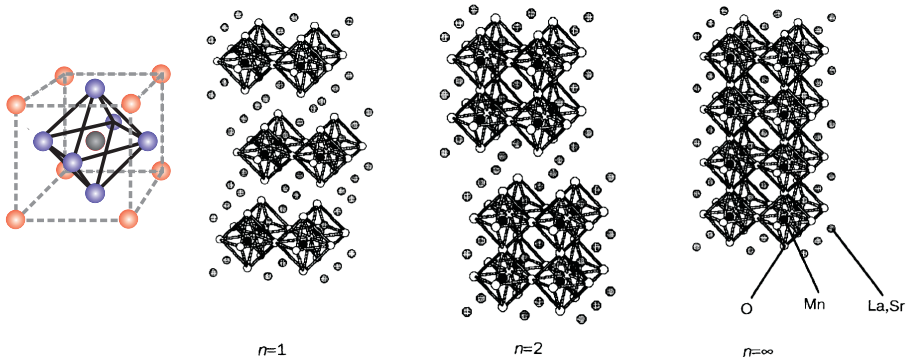

Figure 3.2: The figure shows the unit cell on the left side. Starting with n=1, the beginning of the Ruddlesden Popper series is shown, with the special case, n=∞ to the right.

MnO_2 and AO planes, where the AO planes are acting as charge reservoir layers for the Mn^{3+}/Mn^{4+} mixture. The parent cubic perovskite phase can be generalized through the Ruddlesden Popper series to include layered systems that have more then one charge buffer layer [26], see figure 3.2. These layered systems are characterized through a strong anisotropy perpendicular to the near two-dimensional MnO_2 planes [27].

When the manganese ion is placed in an octahedral environment the fivefold degeneracy of the *d*-orbitals is lifted. This crystal field splitting is due to an increased (decreased) electrostatic interaction when the Mn 3*d*-orbitals point towards (away from) a higher electron density. Orbitals with lobes pointing in between the oxygen ligands have a lower energy and form the t_{2g} (xy, yz, zx) subset; orbitals with lobes pointing towards the ligands form the higher energy e_g subset (x^2-y^2, $3z^2$-r^2). The energy separation between the two subsets is given by the crystal field energy, ΔCF, also called 10Dq and can be estimated to be around 1 eV [28, 29].

As mentioned above, the ratio of the dopant atoms RE/AE completely determines the manganese valency (Mn^{3+}/Mn^{4+}). The on-site spin orientation is determined from the first Hund's rule[1]; the first three electrons are placed with parallel spin into the t_{2g} orbitals and can be treated as localized. The fourth electron (from Mn^{3+}

[1]maximization of the total spin in the case of more energy levels than electrons

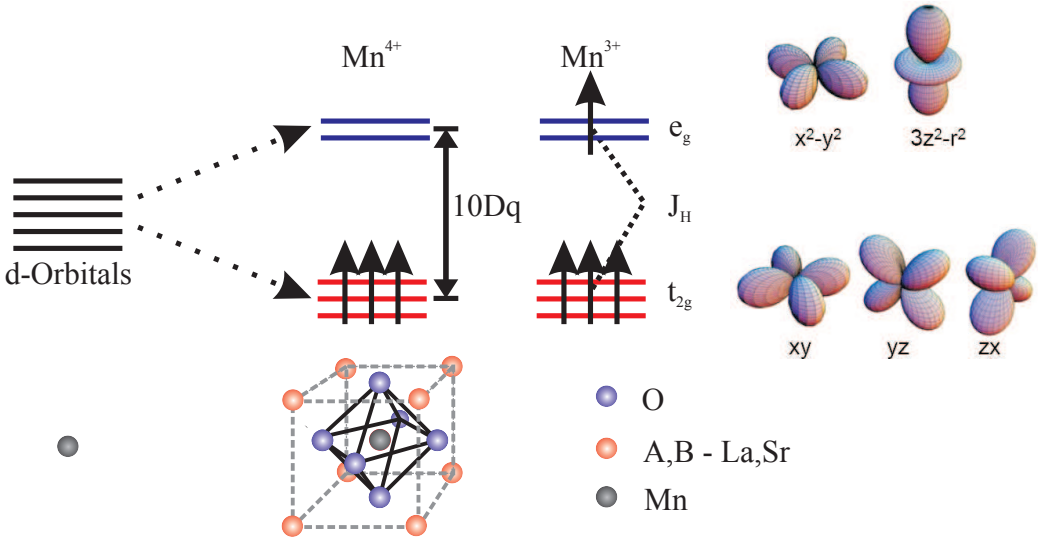

Figure 3.3: The figure is showing the influence of the crystal field onto the *d*-orbitals of the manganese ions.

sites) has to overcome the crystal field energy 10Dq to obey Hund's rule. In most cases the Hund's energy is bigger than the crystal field energy ($J_H \geq 10Dq$) and a high spin state is maintained, leaving a single electron in the e_g orbital, spin polarized parallel to the t_{2g}. Estimation of the strength of the Hund's coupling energy gives values between 1-2 eV, as shown by photoemission [30] and by optical conductivity measurements [31, 32, 33].

Further stabilization of the electronic configuration can be accomplished by a structural distortion of the lattice, known as Jahn-Teller distortion. Such a distortion is shown in figure 3.4 where the apical oxygen atoms undergo a displacement, in this way they reduce the energy of the e_g orbital further.

It is worth noting that the Jahn-Teller theorem predicts the existence of the distortion but not its strength. A tetragonal distortion of an octahedron can either increase the apical direction while simultaneously decrease the size of the basal plane, or the reverse can occur. To first approximation, the lattice distortion increases the energy, while the reduced electrostatic energy with the oxygen ions lowers the energy

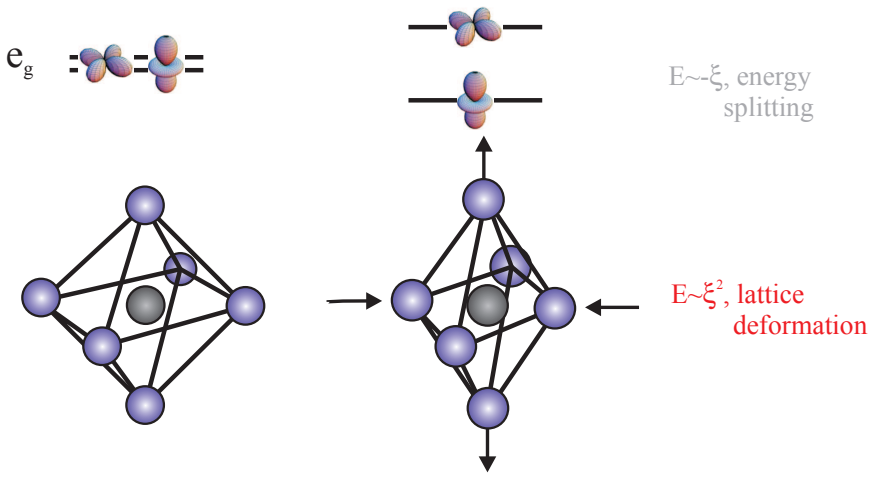

Figure 3.4: Illustration of the Jahn-Teller effect

of one of the orbitals, see equation 3.1.

$$E_{JT}(\xi) = -g\xi + B\xi^2 \tag{3.1}$$

Systems, in which the overall energy gain is positive, are Jahn-Teller active and a small distortion ξ is realized, shown in Figure 3.4.

3.2 Chemical doping and tolerance factor

The mixture of Mn^{3+}/Mn^{4+} can be controlled by changing the ratio x between the rare earth and the alkaline ions ($RE_{1-x}AE_x$) on the A site of the perovskite structure. By adjusting the charge carrier concentrations the magnetic and transport properties are altered, thus phase control is possible. Simultaneous to the filling the different radii of RE and AE ions leads to a modification in the Mn-O-Mn bond angle, as illustrated in figure 3.5. A deviation of the Mn-O-Mn bond angle from the ideal 180° decreases the overlap between manganese *d*- and oxygen *p*-orbitals. This is because the spatial shape of the oxygen *p*-orbital prevents it from pointing simultaneously to both manganese orbitals. As a result, the one-electron bandwidth (W) will decrease with increasing mismatch of the dopants on the A site. This change can be quantified with the tolerance factor f:

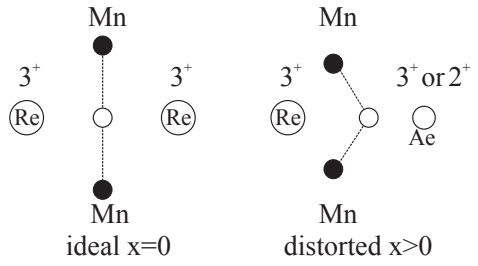

Figure 3.5: When the ratio x between the rare earth and the alkaline earth ions on the A side is changed the Mn-O-Mn will start to deviate from the ideal 180deg bond, due to the different size of the dopants.

$$f(x) = \frac{r_{Mn} + r_O}{\sqrt{2}(r_{\mathrm{A}}(x) + r_O)}. \tag{3.2}$$

where r_{Mn}-radius of manganese ion, r_O-radius of the oxygen and r_A is the average radius of the A-site ions. The resulting lattice structure change often has the form of a rotation, or buckling, of the MnO_6 octahedron.

Both effects are intertwined strongly. For small concentrations x of dopants the filling effect dominates: the insulating ground state is replaced by a ferromagnetic metallic (FM) phase. At some level of doping the different sizes of the ions alters the crystal structure fundamentally and modifies the overlap of the wavefunction.

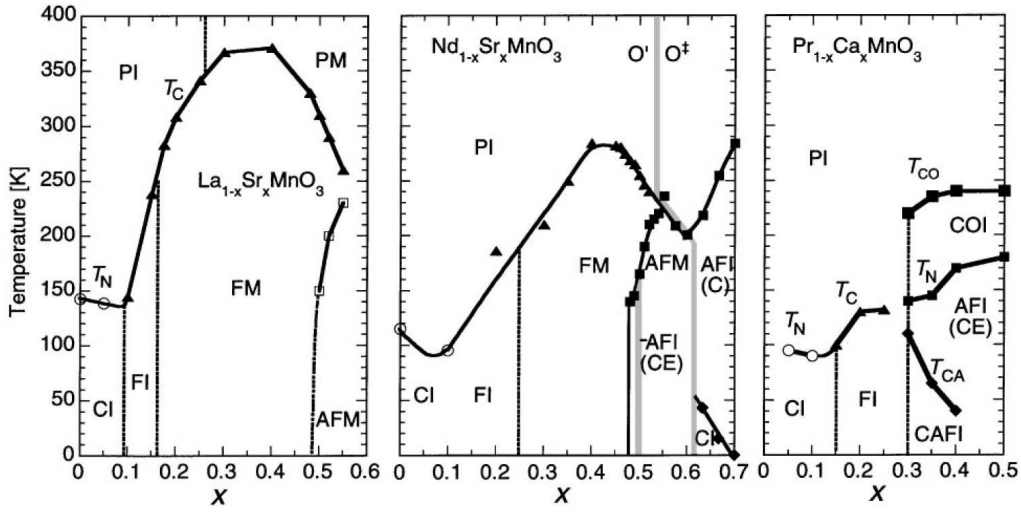

Figure 3.6: The Magnetic and electronic phase diagram for a high ($La_{1-x}Sr_xMnO_3$), medium ($Nd_{1-x}Sr_xMnO_3$) and low ($Pr_{1-x}Ca_xMnO_3$) bandwidth system is shown, [25]. The PI, PM and CI denote the paramagnetic insulating, paramagnetic metallic and spin-canted insulating states, respectively. The FI, FM, and AFM denote the ferromagnetic insulating and ferromagnetic metallic, and antiferromagnetic (A-type) metallic states, respectively. At x=0.5 in $Nd_{1-x}Sr_xMnO_3$, the charge-ordered insulating (COI) phase with CE-type spin ordering is present.

For certain doping levels the one-electron bandwidth is reduced to a point where the kinetic energy is weaker then the Coulomb interaction between the electrons. This can lead to an antiferromagnetic insulating phase (AFI) and in general to a complex phase diagram, see figure 3.6.

A particularly interesting region in the phase diagram is at half doping: when there are equal amounts of Mn^{3+} and Mn^{4+} ions. This can be seen for example in the manganite $Nd_{0.5}Sr_{0.5}MnO_3$ shown in Figure 3.6, where the antiferromagnetic charge ordered insulating phase (AFI) coexists with the ferromagnetic phase. This AFI state is characterized by an antiferromagnetic ordering of the orbitals and the spins in a so-called CE type pattern. Along one dimensional 'zig-zag' chains the spins are aligned ferromagnetically and coupled antiferromagnetically in the perpendicular direction. Experimental observation of this electronic ordering can be achieved with neutron or resonant x-ray scattering.

3.3 Magnetic interaction

A basic understanding of the different phases present in the manganites can be achieved by looking on the magnetic interaction. It is always between neighbouring manganese ions which are bridged by the non magnetic oxygen ligand, see figure 3.3. Thus the exchange interaction is strongly dependent on the hybridisation between oxygen *p*- and manganese *d*-orbitals. Additionally it also depends on the number of electrons (or the filling) in the manganese e_g orbital. The two dominant magnetic interactions are superexchange and the double exchange.

3.3.1 Superexchange

Superexchange is active in compounds where the spins of the magnetic ion are coupled through bridging anions such as oxygen. Consider two nearby Mn^{3+} ions separated by a O^{2-} ion. The strong Hund's rule forces the on-site e_g and the t_{2g} electrons into a high spin configuration. The three atom configuration Mn^{3+}-O-Mn^{3+} can reduce their energy by virtual hopping processes of the single highest lying electron. For the ferromagnetic ground state the virtual hopping processes involve the occupation of a higher energy orbital (on the O site) due to the Pauli exclusion principle. Therefore, the magnetic superexchange interaction favours an antiferromagnetic ground state when the nearest Mn sites are half filled. Alternatively, the superexchange can be understood as a covalent bond where only one spin direction takes part in the bonding. Goodenough used the term 'semi-covalent' to explain this effect [34].

3.3.2 Double exchange

The second important exchange interaction between two manganese ions is the double exchange, illustrated in figure 3.7. It occurs between Mn^{3+} and Mn^{4+} ions and favours a ferromagnetic ground state. The name double exchange derives from the idea that

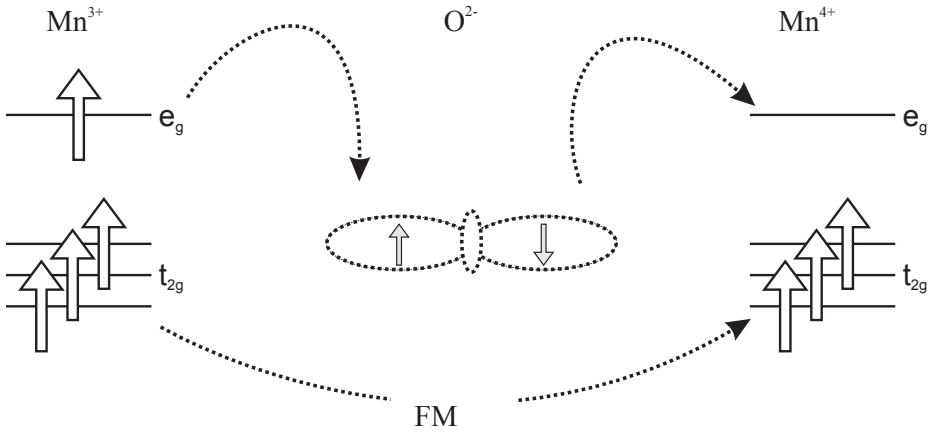

Figure 3.7: Double exchange mechanism leads to a delocalisation of the e_g electrons when the core t_{2g} electrons are ferromagnetically aligned.

the transfer from the first manganese ion to the oxygen happens at the same time as the transfer from the oxygen to the second manganese ion, thus involving two simultaneous hopping stages. It can be derived by using the single orbital model:

Single orbital model The single orbital model, also called the double exchange model, captures one of the most important interactions in the manganites. It rests on several approximations [35]:

(a) neglect the coupling with phonons:

(b) neglect the Coulomb interaction between e_g electrons:

(c) the Jahn-Teller distortion is assumed to be static:

(d) assume only one active orbital.

The model can be used to explain the competition between metallic ferromagnetism and insulating antiferromagnetic behaviour, the most important aspects in the CMR mechanism. It is used to describe the movement of the conduction electrons in a background of frozen t_{2g} spins [36]. The corresponding Hamiltonian can be written as:

$$H = -\sum_{<i,j>} t_{ij}(c^{\dagger}_{i\sigma}c_{j\sigma} + h.c.) - J_H \sum_i s_i S_i + J_{AF} \sum_{<i,j>} S_i S_j \qquad (3.3)$$

where $< i, j >$ indicates the summation over the nearest neighbours only, $c_{i\sigma}$ is the creation or annihilation operator and t_{ij} is the transfer integral of the conduction electrons. J_{AF} describes the interaction between the localized t_{2g} spins. J_H is the on-site Hund's coupling energy. A double occupancy of a single orbital requires an antiferromagnetic spin alignment, which is penalized by Hund's energy. Therefore, neglecting the electron-electron interaction is justified as J_H is strong enough to make the double occupancy of a single site unlikely. The spin state of the e_g orbital is given by $\underline{s}$ while $\underline{S}$ symbolizes the combined spin of the three electrons occupying the t_{2g} orbital. For simplicity, the model assumes that there are only two sites (labelled 1 and 2) and that the classical spin direction of site 1 defines the z-axes, while the spin of site 2 is arbitrarily aligned in the xz-plane, $\underline{S}_1 = S(0, 0, 1)$ and $\underline{S}_2 = S(\sin(t), 0, \cos(t))$. In the case of strong Hund's coupling only the projection of the conduction-electron's spin along the direction of the background t_{2g} spins is energetically favourable. Therefore, the system can be described using a basis set defined by the spin of site 1. Rotating the creation and destruction operators at site 2 gives

$$c_{\uparrow,2} = \cos\frac{\theta}{2}\tilde{c}_{\uparrow,2} - \sin\frac{\theta}{2}\tilde{c}_{\downarrow,2} \tag{3.4}$$

$$c_{\downarrow,2} = \cos\frac{\theta}{2}\tilde{c}_{\downarrow,2} - \sin\frac{\theta}{2}\tilde{c}_{\uparrow,2} \tag{3.5}$$

Inserting this into the kinetic energy term and dropping the energetically unfavourable states where the spin is anti-parallel to the combined t_{2g} spin, the kinetic energy or hopping term becomes

$$H_T = -t_{eff}(\tilde{c}^{\dagger}_{\uparrow,1}\tilde{c}_{\uparrow,2} + h.c.) \tag{3.6}$$

with $t_{eff} = t\ \cos(\frac{\theta}{2})$. From this effective Hamiltonian it can be seen that the ferromagnetic alignment of the neighbouring t_{2g} spins ($\theta = 0$) results in a positive hopping integral, whereas antiferromagnetic alignment ($\theta = 180$ deg) results in a

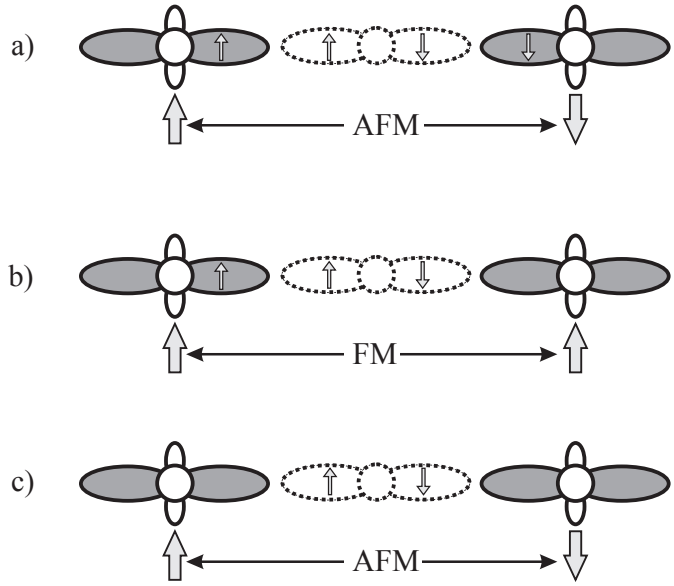

Figure 3.8: Goodenough Kanamori rules for a) two half-filled orbitals b) one filled, one half-filled c) both filled or empty

vanishing hopping amplitude and hence no energy gain.

3.4 Goodenough-Kanamori-Anderson rules (GKA)

Based on the consideration above, the GKA rules predict magnetic ordering phenomena in manganites. The GKA rules predict the sign of the exchange integral J, between two cations, bridged by a O^{2-} ion, depending on the filling of the cation. The bonding occurs between the full oxygen $2p$- and the unfilled manganese d-orbitals.

The Goodenough Kanamori rules can be summarized as follows (also figure 3.8):

1. the exchange is antiferromagnetic when both orbitals are either half-filled or when both are empty, see figure 3.8 a) and c)

2. the exchange is ferromagnetic when either (i) one orbital is full and the other half-filled or (ii) when one orbital is half-full and the other empty, see figure 3.8 b).

3.5 Orbital ordering and its origin

Orbital ordering is the tendency for the occupied e_g orbitals to form long-ranged ordered patterns. This order breaks the local symmetry and gives rise to the directionality of the electronic-transfer interaction. Depending on the directionality of orbitals on neighbouring sites, the GKA rules predict either a ferromagnetic or an antiferromagnetic ground state. This leads to complex coupling between the spin and the orbital degree of freedom. For example the A-Type order in the prototypical compound $LaMnO_3$ shown in figure 3.9. In the MnO_2 plane (*ab* plane) half-filled orbitals are pointing towards empty orbitals, this gives rise to ferromagnetic coupling according to the GKA rules. Along the c direction the superexchange between two unfilled e_g orbitals is of the antiferromagnetic type.

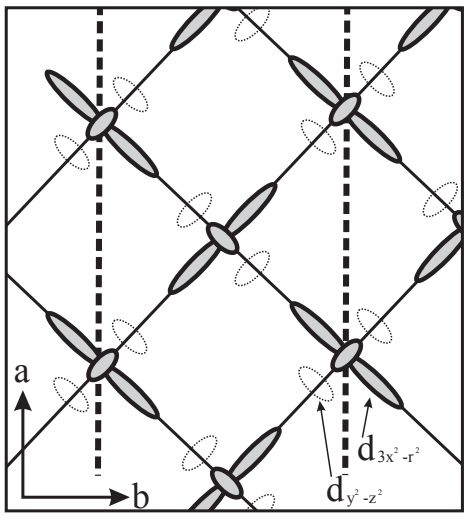

Figure 3.9: Depicted is the A type orbital order in the *ab* plane of $LaMnO_3$. In the *ab* plane the GKA rules predict ferromagnetic coupling, along the c direction the coupling is of the antiferromagnetic type, the spins are pointing along the c direction (out of the paper plane).

There are two possible origins of the orbital order: It either can be a consequence of the Jahn-Teller effect or it can arise from an exchange mechanism.

The Jahn-Teller distortion leads to a preferred occupancy and orientation of a specific orbital. This process is driven by a reduced electrostatic interaction when the orbital is aligned along the direction of the Jahn-Teller distortion.

Neighbouring manganese ions share their oxygen ligands and a deformation of one oxygen cage will couple to the neighbouring one, giving rise to a symmetry reduction of the whole crystal, see figure 3.10.

In doped manganites, where the valencies of the manganese ion alternates between Mn^{3+} and Mn^{4+}, the degree of Jahn-Teller distortion varies. As there are no electrons in the e_g orbital of Mn^{4+} ion, the octahedron is distorted less than the octahedron that surrounds the Mn^{3+} ion.

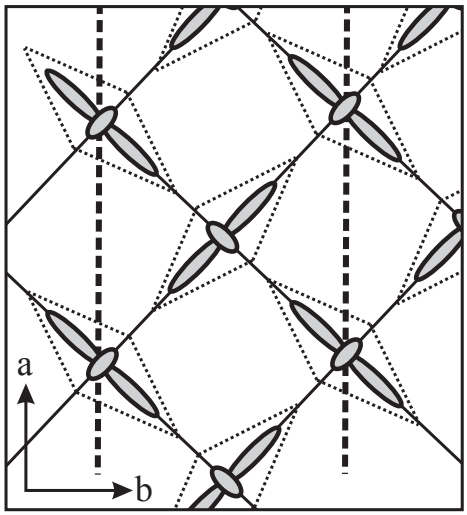

Figure 3.10: The Jahn-Teller distortion leads to the occupation of a specific orbital due to a reduced electrostatic interaction of the manganese wavefunction with the oxygen ligands.

Electronic exchange interaction Orbital ordering can also be explained purely by electronic exchange effects and therefore can occur without a change in the crystal symmetry [37, 38]. In figure 3.11 (b) different spin configurations for a double degenerate system are shown. When the spins are parallel (case (i)) the electrons cannot delocalize due to the Pauli exclusion principle. In case (ii) the electrons have antiparallel spin and can reduce their energy through virtual hopping processes (given by t) in both directions. The energy in case (iii) is further reduced because ferromagnetic alignment causes the electrons to occupy a higher lying orbital. They can delocalize over the bond and due to the alternating occupation of orbitals ('antiferro' orbital structure), the electron-electron repulsion U is reduced by the Hund's coupling energy J_H.

Both origins (electronic and lattice driven) can lead to macroscopic distortions, therefore it is difficult to asses what the microscopic cause is. Local density calcula-

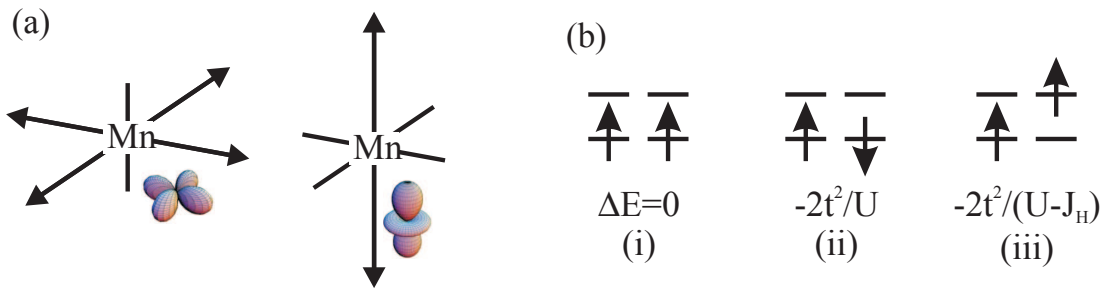

Figure 3.11: **(a)** The Jahn-Teller driven distortion of the oxygen Octahedron favours the occupancy of a specific orbital to minimize the electrostatic energy. **(b)** Energy diagram of electronic exchange effects that will lead to orbital ordering due to the Hund's energy.

tions (LDA+U) [39] predict the observation of orbital structure in a symmetric lattice (no Jahn-Teller distortion) [40, 41]. The simulations also predict that 60-70% of the energy gain in the orbital ordering can be explained only by the exchange mechanism.

Chapter 4

Experimental technique

Measuring the orbital and spin order in manganites is difficult but crucial. These ordering patterns, sometimes of less then one valence charge per atom, are a key factor in explaining the properties of most manganites [5]. A technique to investigate them has to be able to discriminate between effects originating from a single electron (or less) against the larger background composed of all the other electrons. In the static regime resonant x-ray diffraction (RXD) has proven to be a valuable tool [42, 43, 44]. This chapter will build the necessary theoretical fundament to understand this approach. It will show that RXD can be understood as a combination of real space sensitive absorption spectroscopy with k-space sensitive diffraction. As a first step the main ideas behind x-ray diffraction are introduced. This is then followed by discussing the effects near elemental absorption edges.

4.1 X-ray diffraction

When x-rays, with wavevector $\underline{k}_0$, are incident upon matter they are either absorbed or scattered. If $\underline{k}_0$ is chosen correctly then the scattered radiation from the individual atoms constructively interacts along certain directions. An intensity pattern is observable in the far field. The scattering process can be understood with the following

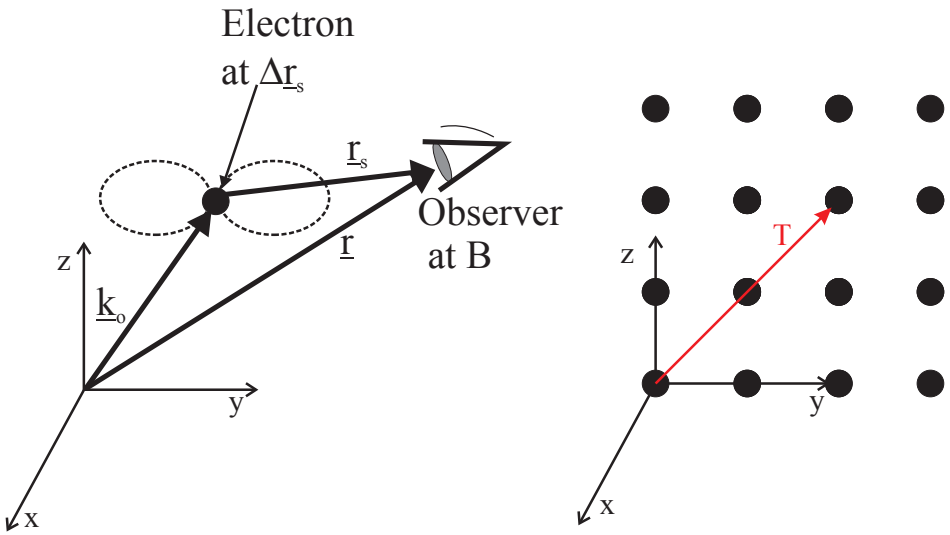

Figure 4.1: Left: Scattering from a single electron **Right:** Geometrical structure factor

assumptions: the x-rays are diffracted from individual particles (located at $\Delta\underline{r}_s$) and the incident x-rays are described by plane waves $E(\Delta\underline{r}_s) = A_e \cdot \exp[i(\underline{k}_0\Delta\underline{r}_s - \omega t)]$. The intensity observed at a position B($\underline{r}$) in the far-field ($r \gg \Delta r_s$, the point at which x-rays are scattered) is thus given as:

$$A_B = f \cdot \frac{E(\Delta r_s)}{r_s} \cdot \exp[i\underline{k}\underline{r}_s] \tag{4.1}$$

with $\underline{r}_s = \underline{r} - \Delta\underline{r}_s$, see also figure 4.1. The atomic form factor, f, is the fraction of the incoming amplitude A_e that is radiated from the scattering site. In the limit of scattering from a single electron, the far field pattern resembles the one generated by a dipole. This is due to the oscillation that the electron performs in the electric field of the incoming electromagnetic wave.

In the current discussion, it is assumed that the x-ray energy is far from any resonances of the scattering system. Later it will be shown that the atomic form factor is crucial in understanding the effects that occur near elemental absorption edges. Using the abbreviation $C = A_e/r_s \cdot \exp[i(\underline{k}_0\Delta\underline{r}_s - \omega t)]$ and the relationship

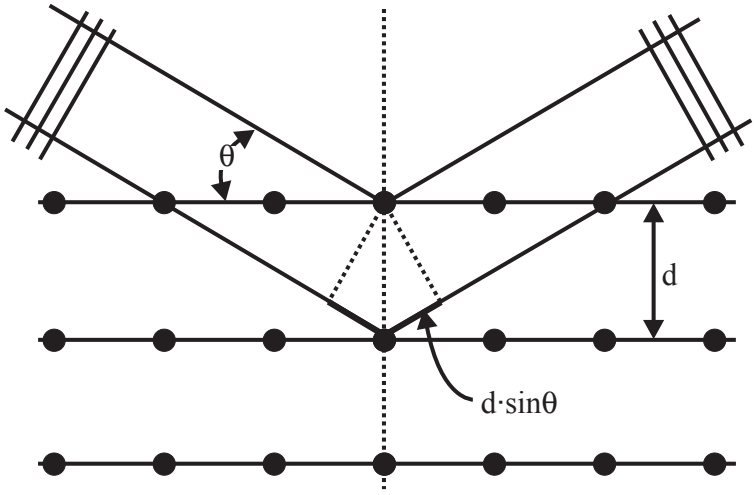

Figure 4.2: Schematic of the Bragg diffraction

$\Delta\underline{k} = \underline{k} - \underline{k}_0$ between incoming and outgoing wavevector, equation 4.1 becomes:

$$A_B = C \cdot f \cdot \exp[i\Delta\underline{k}\Delta\underline{r}_s] \tag{4.2}$$

This form can be used to discuss scattering from multiple particles arranged in a lattice (see figure 4.1). The position of the atoms within the lattice can be expressed as $\underline{T} = m_1\underline{a} + m_2\underline{b} + m_3\underline{c}$, where a,b and c are the unit vectors and m_1, m_2, and m_3 are integers. Thus $\Delta\underline{r}_s$ in equation 4.2 can be replaced with $\underline{T}$. At the observation point in the far field, the total scattering amplitude can be written as the sum of the individual scattering sites:

$$A_{\text{total}} = C \cdot f \cdot \sum_m e^{[i\Delta\underline{k}\cdot(m_1\underline{a}+m_2\underline{b}+m_3\underline{c})]}. \tag{4.3}$$

The exponent in the sum is a phase factor that describes the interference of the waves scattered from the individual atoms in the crystal. The phase factor and therefore the sum will give a maximum when the exponent in equation 4.3 is an integer multiple of 2π or:

$$\underline{T} \cdot \Delta\underline{k} = m \cdot 2\pi \tag{4.4}$$

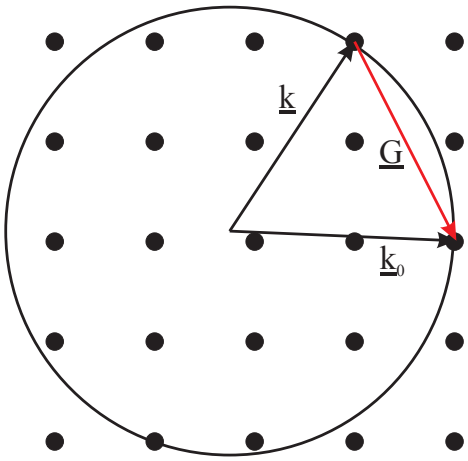

Figure 4.3: The Ewald sphere in the reciprocal space illustrates the Laue condition.

This is the condition for positive interference between waves that are reflected from planes separated by a lattice vector. This vector set of equations is called Laue equations [45]. It can be shown that this set of equations is identical to the Bragg equation [46].

$$\mathrm{d} \cdot \sin\theta = m\frac{\lambda}{2} \tag{4.5}$$

where the distance between the crystal planes, d, for crystals with orthogonal axes can be expressed as:

$$d = \left[\left(\frac{h}{a}\right)^2 + \left(\frac{k}{b}\right)^2 + \left(\frac{l}{c}\right)^2\right]^{-1/2} \tag{4.6}$$

m is the scattering order, λ is the wavelength of the x-rays.

When scattering is considered in the reciprocal space the Laue condition (equation 4.4) can be formulated to include the reciprocal lattice vector (G), which is defined as $\underline{G} \cdot \underline{T} = m \cdot 2\pi$:

$$\underline{G} = \Delta\underline{k} = \underline{k} - \underline{k}_0. \tag{4.7}$$

This fundamental equation can be visualized using the Ewald sphere (or Ewald circle in the two dimensional projection) shown in figure 4.3. The Ewald sphere is constructed by placing the toe of the incoming wavevector k_0 on a reciprocal lattice point. In the case of elastic scattering, the radius of the Ewald sphere is given by

the wavevector of the incoming x-rays. In this construction a diffraction spot occurs when the Ewald sphere intersects with two reciprocal lattice points. Changing the direction of the incident radiation moves the origin of the Ewald sphere and different diffraction spots will become visible.

Atomic form factor A simple introduction to scattering and the origin of the atomic form factor has been given by Attwood [47]. The cross section for scattering is defined as the total scattered power, P, normalized to the incoming power, S.

$$\sigma \equiv \frac{P_{\text{Scatt}}}{|\underline{S}|} \tag{4.8}$$

The incident average power is given through the amplitude of the electromagnetic field and Poynting's theorem

$$|\underline{S}| = \frac{1}{2}\sqrt{\frac{\epsilon_0}{\mu_0}}\,|\underline{E}|^2 \tag{4.9}$$

where ϵ_0 is the permittivity and μ_0 the permeability of free space, $\underline{E}$ is the amplitude of the electromagnetic field and the magnetic field component can be disregarded. The radiated power P_{Scatt} of a free electron can be found by integrating $\underline{S}$ over a distant sphere

$$P = \frac{1}{2}\frac{8\pi}{3}\left(\frac{e^2\,|\underline{a}|^2}{16\pi^2\epsilon_0 c^3}\right) \tag{4.10}$$

here $\underline{a}$ is the acceleration of an electron and c the speed of light. The interaction of the electric field with the electron leads to an accelaration according to Newton's law, $\underline{F} = m\underline{a}$, where F is the Lorentz force on the electron with mass m. When the magnetic field is neglected, the instantaneous acceleration of the oscillating electron is given by $\underline{a}(r,t) = -e/m\underline{E}(r,t)$. This allows to express the scattering cross section

(the Thomson scattering cross section) for the free electron as:

$$\sigma_e = \frac{8\pi}{3} r_e^2 \tag{4.11}$$

where $r_e \equiv e^2/(4\pi\epsilon_0 mc^2)$ is the classical radius of the electron.

When more then one electron is present and the charge is spread out over a volume as shown in figure 4.4 it can be shown that the scattering factor in the continuous limit can be written as:

$$\sigma_e = \frac{8\pi}{3} r_e^2 \underbrace{\int n(\underline{r'}) e^{i\Delta\underline{k}\cdot\underline{r'}} \cdot \mathrm{d}r'}_{f} \tag{4.12}$$

r' is the distance from the scattering centre and n is the charge density per volume. The factor $e^{i\Delta\underline{k}\cdot\underline{r'}}$ accounts for the phase shift of the scattered wave due to the varying position of the scattering sites. In the limit that all the charge (Z) is located in the centre of the scattering region, the atomic form factor reduces to $f = Z$. Therefore, it describes how the scattering cross section deviates from the point charge. It is worth noticing that the form factor has the form of a Fourier transformation. This leads to the interpretation that the diffraction pattern is the Fourier transformation of the real space charge distribution. The crystal periodicity is encoded into the arrangement of the spots while the intensity depends on the type of scatterer present. For diffraction to be possible the wavelength of the x-rays has to be of the order of the lattice periodicity, see equation 4.5.

4.2 Resonant x-ray diffraction

Resonance effects can have a dramatic effect on the x-ray scattering signal. This can be easily shown by considering a bound electron, interacting with the electromagnetic wave. The electron is bound by the restoring force of the nucleus ($\propto= -kx$) and

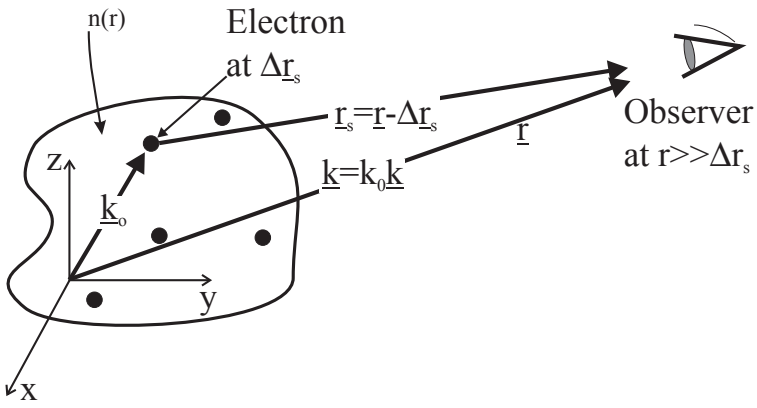

Figure 4.4: Semi classical model of multi electron scattering

dissipates energy to the rest of the system through a damping term γ. The bound electron is driven by the external electromagnetic field of the x-rays $\underline{E} = \underline{E}_0 e^{-i\omega t}$, leading to an equation of motion similar to the driven harmonic oscillator:

$$m\frac{\mathrm{d}^2\underline{x}}{\mathrm{d}t^2} + m\gamma\frac{\mathrm{d}\underline{x}}{\mathrm{d}t} + m\omega_0^2\underline{x} = -e\underline{E} \tag{4.13}$$

ω is the frequency of the incoming x-ray radiation and $\omega_0 = \sqrt{k/m}$ is the resonance frequency. Following the same approach as for the unbound case (see equation 4.12), the scattering cross section can be written as:

$$\sigma_e = \frac{8\pi}{3}r_e^2 \underbrace{\frac{\omega^4}{(\omega^2-\omega_0^2)^2 + (\gamma\omega)^2}}_{f} \tag{4.14}$$

and the cross section is a function of the incident x-ray energy, which is peaked at $\omega = \omega_0$.

Scattering from multiple electrons at a distance Δr_s away from the nucleus, can be included by assuming that the charge distribution of equation 4.12 can be written as $n(\underline{r}, t) = \sum_{s=1}^{Z} \delta[\underline{r} - \Delta\underline{r}_s(t)]$. The different positions of the scattering sites within the atom gives an additional phase factor $(\underline{k}_i \cdot \Delta\underline{r}_s)$, which enters into the equation of motion, resulting in an acceleration of the form:

$$\underline{a}_s(t) = \frac{-\omega^2}{\omega^2 - \omega_s^2 + i\gamma\omega}\frac{e}{m}\underline{E}_i e^{-i(\omega t - \underline{k}_i \cdot \Delta\underline{r}_s)} \tag{4.15}$$

Summing up over all the electrons within the atom the scattering field in the far field becomes

$$E(\underline{r}, t) = -\frac{r_e}{r_s}\sum_{s=1}^{Z}\frac{\omega^2 E_i \sin\theta}{\omega^2 - \omega_s^2 + i\gamma\omega} e^{-i[\omega(t - r_s/c) - \underline{k}_i \cdot \Delta\underline{r}_s]} \tag{4.16}$$

with $\underline{r}_s \equiv \underline{r} - \Delta\underline{r}_s$ and $r_s = |\underline{r}_s|$, θ is the angle between the acceleration and the observation direction $\underline{k}_0$. For $\underline{r} \gg \Delta\underline{r}_s$, r_s can be approximated to $r_s \approx r - \underline{k}_0 \cdot \Delta\underline{r}_s$. This simplifies equation 4.16 to $E(\underline{r}, t) = \frac{-r_e}{r} f(\Delta\underline{k}, \omega) E_0 \sin\theta e^{-i\omega(t - r_s/c)}$ where the factor $f(\Delta\underline{k} = \underline{k} - \underline{k}_i, \omega)$ is defined as:

$$f(\Delta\underline{k}, \omega) = \sum_{s=1}^{Z}\frac{\omega^2 e^{-i\underline{k}_i \cdot \Delta\underline{r}_s}}{\omega^2 - \omega_s^2 + i\gamma\omega} \tag{4.17}$$

Pure quantum field treatment yields a similar form for the scattering factor, for example shown by Blume and Blume and Gibbs [48, 49]:

$$f_j(\omega) = \frac{m_e}{\hbar^2}\frac{1}{\hbar\omega}\sum_n \frac{(E_n - E_g)^3 \langle \Psi_n | O | \Psi_g \rangle \langle \Psi_g | O^* | \Psi_n \rangle}{\hbar\omega - (E_n - E_g) - i\frac{\Gamma_n}{2}} \tag{4.18}$$

where $\hbar\omega$ is the photon energy, m_e is the electron mass and Ψ_g,E_g and Ψ_n,E_n indicate the wavefunction and energy of the ground and the intermediate state, respectively. Γ denotes the inverse lifetime of the excited state and O is the operator of the light field. The dependency on the resonant term leads to an enhancement of the scattering cross section that is unique for elemental transition edges.

Resonant x-ray diffraction requires two conditions. Firstly, the incoming photon energy has to be resonant to an absorption edge and secondly the corresponding Ewald sphere has to intersect with a reciprocal lattice point, see figure 4.3. Fulfilling both conditions simultaneously can be difficult, like at the L-edge of the manganites.

The resonance condition limits the size of the Ewald sphere, this allows an intersection with a reciprocal lattice point only in special cases. One of the materials with a unit cell large enough in the charge and orbital ordered phase is $La_{0.5}Sr_{1.5}MnO_4$.

Chapter 5

The compound $La_{0.5}Sr_{1.5}MnO_4$

The material $La_{0.5}Sr_{1.5}MnO_4$ has become a benchmark material to study charge, orbital and spin ordering in the manganites. The electronic order has been extensively studied using x-ray [42, 50] and neutron scattering [51, 52].

The size of the electronic ordered unit cell makes it possible to perform resonant x-ray scattering in the soft x-ray range as is shown in [43, 53]. This enables the direct measurement of ordering patterns in the $3d$ orbitals of the manganese ions. Due to the layered structure the orbital order is confined in the ab-plane. Macroscopic probes, such as optical birefringence, can thus be used to meausure orbital order. This allows their study on the ultrafast timescale, see chapter 7 and [54].

Furthermore, theoretical simulations exist that allow interpretation of the energy-resolved soft x-ray diffraction spectra. Based on this firm foundation the compound emerges as a prime candidate to study the interplay of photo excitation with electronic order.

5.1 Properties

Through the Ruddlesden Popper series the three dimensional perovskite system $La_{1-x}Sr_xMnO_3$ ($n = \infty$) can be related to the quasi-two-dimensional compound

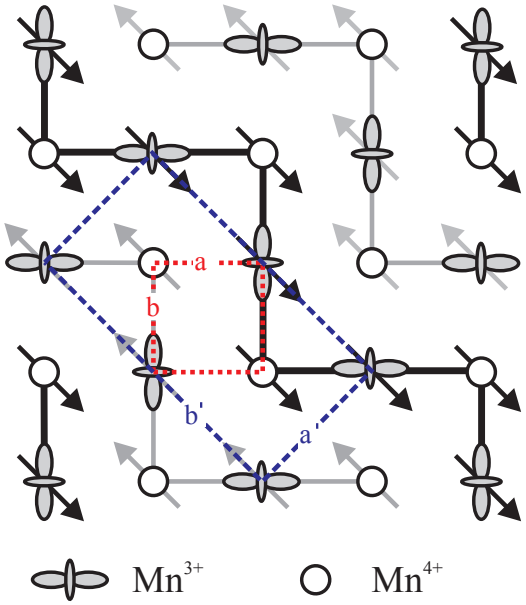

Figure 5.1: Charge and orbital ordering pattern in the ab plane of $La_{0.5}Sr_{1.5}MnO_4$, along the direction of the orbitals the GKA rules predict ferromagnetic coupling while it is antiferromagnetic in the perpendicular direction.

$La_{1-x}Sr_{1+x}MnO_4$ ($n = 1$). The reduced dimensionality leads to a smaller electron bandwidth and hence the electron tendency towards delocalisation is reduced[1]. This is for example reflected in the larger resistivity [55]. Unlike the three dimensional parent compound, $La_{1-x}Sr_{1+x}MnO_4$ does not have a ferromagnetic metallic phase, for any doping value.

Particularly interesting is the behaviour at half doping, $La_{0.5}Sr_{1.5}MnO_4$. Below $T \leq T_{CO/OO} = 220$ K a special charge/orbital order has been observed in neutron [56, 57] and resonant hard x-ray diffraction [42]. Originally this pattern has been described as alternating Mn^{3+}/Mn^{4+} ions with a wavecetor of ($1/2$ $1/2$ 0) as shown in figure 5.1 [34, 56]. This full charge separation picture of one charge per site requires a strong lattice distortion which was not observed [58, 59]. Therefore, it seems more appropriate to describe the order as $Mn^{+3.5+\delta}$/ $Mn^{+3.5-\delta}$. Some experiments allowed an interpretation based on a charge separation of $0.01e$ [60]. From theoretical first

[1]The single electron bandwidth is given by the relationship $W = 2nt$, where n is the number of nearest neighbours and t is the hopping amplitude (equation 2.2). In a three dimensional cubic lattice the bandwidth is $W = 12t$ which reduces to $W = 8t$ in a two dimensional square lattice.

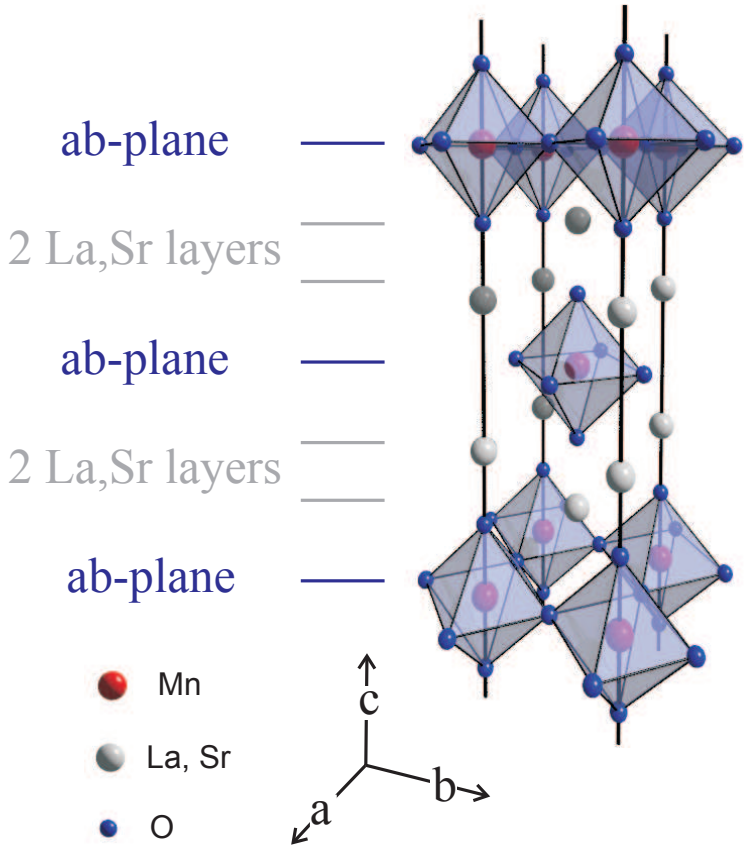

Figure 5.2: Three dimensional crystal structure. The *ab* plane with the MnO_2 ions is separated by a $(La,Sr)_2O_2$ charge buffer layer.

principle calculations a charge separation of $0.09e$ was predicted [61].

The orbital and spin coupling occurs along ferromagnetic 'zigzag' chains that show antiferromagnetic coupling to the neighbouring chains. This CE-type pattern is described by a new unit cell (a',b') that is rotated by 45° relative to the original one (a,b), as shown in figure 5.1. The dimensions of the new, orbital ordered, unit cell is given by $2\sqrt{2}$a×$\sqrt{2}$b×c (a'×b'×c).

A prediction of the sign of the exchange constants can be achieved using the GKA rules. Along the chain direction a full Mn^{3+} orbital faces an empty Mn^{4+} one, this gives a ferromagnetic coupling. The inter-chain coupling is between empty orbitals and therefore of the antiferromagnetic type. An alternative explanation of this CE type pattern was given by Daoud-Aladine et. al. [62, 63]. They used a Zener-

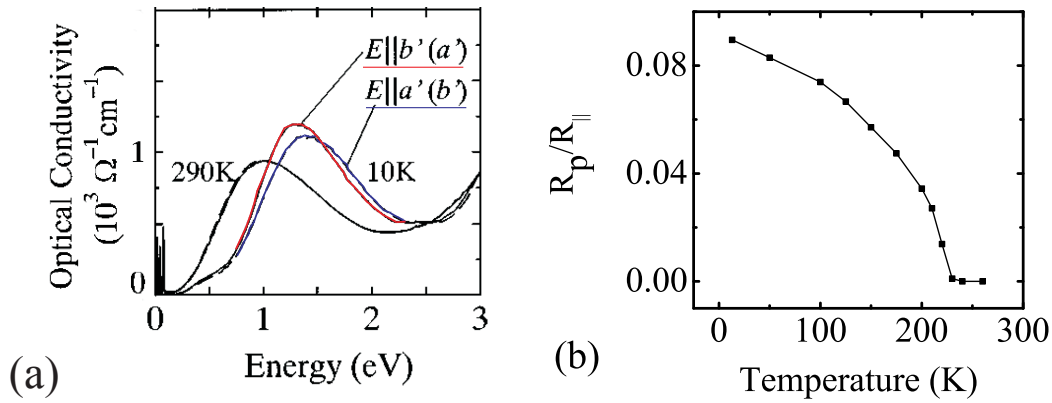

Figure 5.3: (a) Optical conductivity for the different principal axes, from [65]. (b) Optical anisotropy at 1.96 eV over temperature.

Polaron motif were the charge is mainly localised on the Mn-O-Mn bond instead of on the manganese ion. It is currently debated how well this picture, derived from $Pr_{0.6}Ca_{0.4}MnO_3$, can be generalized for all the manganites [64]. However, in the presented work the description will be based on the site centered description.

When the system is cooled below $T_N = 110$ K the magnetic moments associated with the manganese ions couple antiferromagnetically along the c direction to form a unit cell of the size $2\sqrt{2}$a×$2\sqrt{2}$b×2c [51, 57].

5.2 Optical properties

At elevated temperature (such as room temperature) $La_{0.5}Sr_{1.5}MnO_4$ has a perfect tetragonal structure in contrast to the three dimensional manganites. Upon cooling below the ordering temperature ($T<T_{OO/CO}$) this tetragonal symmetry is broken. As previously discussed, the layered structure confines the ordering pattern into the MnO_2 plane. The ordering pattern involves the orientation of the Mn^{3+} e_g electrons along chains in the [110] direction. Along those chains the electrons are more strongly delocalised then perpendicular to them. Thus cooling leads to the evolution of an anisotropic electronic structure in the material. Ishikawa showed that this can be

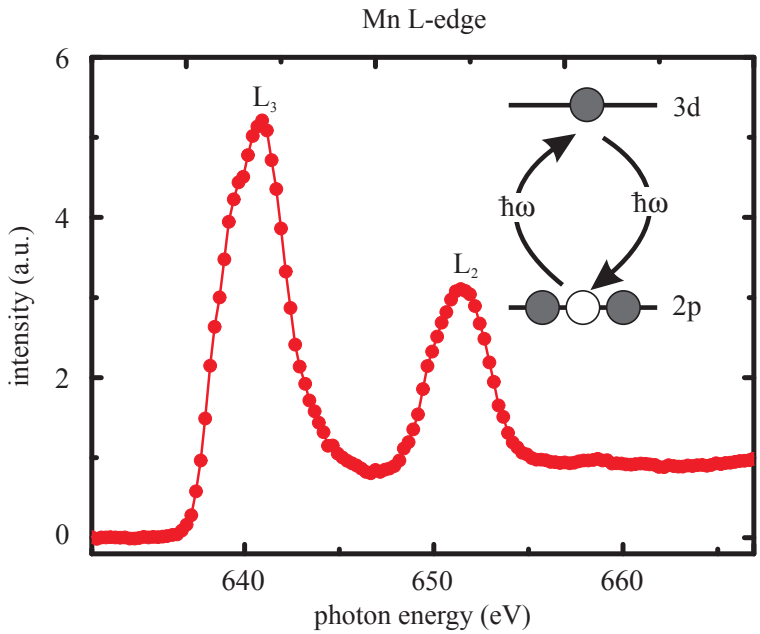

Figure 5.4: X-ray absorption spectrum at the manganese $L_{2,3}$-edge

probed optically [65]. In figure 5.3 (a) the optical conductivity spectra is shown. At room temperature a broad peak at 1 eV is visible, which is due to the hole doping, it is absent in the undoped case $LaSrMnO_4$ [66]. Upon cooling this peak shifts to higher energies, which is consistent with the more insulating nature of the material at lower temperature. The shift is anticipated to arise from changes in the *d*-*p* hybridisation. Additionally, the peak also splits, an optical anisotropy develops, as expected from the ordering pattern. Figure 5.3 (b) shows the optical anistropy over temperature. It shows the same temperature behaviour as resonant x-ray diffraction measurements [42] and therefore was attributed to orbital ordering.

5.3 Resonant scattering in $La_{0.5}Sr_{1.5}MnO_4$

5.3.1 Sample preparation

The single crystals were grown at the Department of Physics at the University of Oxford and at the Laboratoire de Physico-Chimie de l'Etat Solide, Universit*é* de

Paris-Sud (LPCES).

The crystal growth was carried out using the floating zone technique in a quadruple ellipsoid infrared image furnace equipped with four halogen lamps as heat sources, for samples grown at the LPCES a double ellipsoid infrared image furnace and only two halogen lamps where used. Feed rods were prepared by solid state reaction: stoichiometric mixtures of La_2O_3 (dried at 900°C for 24 h), $SrCO_3$; and MnO_2 (purity $\geq$99.99% for all compounds) were calcined at 900°C for 30 h. With intermediate grinding, heat treatments were performed at 1100°C (30 h), 1300°C (30 h), and 1410°C or 1500°C (50 h) before isostatically cold pressing the obtained powder under 2.5 kbar, and sintering it at 1410°C or 1500°C (50 h). The resulting compact material was again thoroughly reground and then cold-pressed (2.5 kbar) into rods of ≈6mm diameter and 7-10 cm length before repeating the sintering procedure [67, 68].

After the crystal growth the rods were aligned using Laue diffraction with either [110] or [112] direction surface normal. Then slabs with a thickness of 1-2 mm were prepared using a diamond saw. The surface was polished to a mirror-like finish with a succession of diamond polishing wheels. First, a rough polishing wheel with a grain size of 8μm was used. Then, the grain size was reduced in steps down to 100nm, the best results were achieved using the following sequence of diamond wheels: 8, 2, 0.6 0.3 and finally 0.1 μm.

The base temperature of $La_{0.5}Sr_{1.5}MnO_4$ was held at 25 K unless otherwise stated.

5.3.2 Resonant scattering

Equation 4.18 shows that the scattering factor depends on the final states available to the atom or ion. This provides a contrast mechanism which can be exploited to measure the ordering of the charges and the orbitals. Besides the sensitivity to the final state, the denominator in equation 4.18 also has a resonant term. Therefore, when the photon energy is tuned to an absorption edge resonant enhancement occurs.

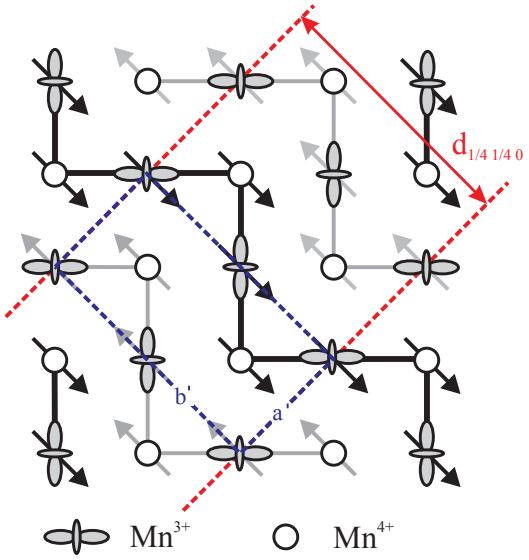

Figure 5.5: Charge and orbital ordering pattern in the compound $La_{1.5}Sr_{1.5}MnO_4$. The Bragg planes of the ordering structure are indicated by the dashed red lines.

At the *L*-edge electrons from the $2p$ level are directly promoted into empty orbitals in the orbital ordered $3d$ shell, $2p \rightarrow 3d$ see figure 5.5[2].

At the manganese *L*-edge the limited size of the Ewald sphere only allows the detection of ordering with periodicities that are long enough. One of the few compounds where the detection of charge, orbital and spin order is partially possible is $La_{0.5}Sr_{1.5}MnO_4$. The orbital order can be described through a wavevector of ($1/4$ $1/4$ 0), the corresponding Bragg planes are shown in figure 5.5 with dashed red lines. The constraints due to the limited size of the Ewald sphere can be visualized at the orbital order peak when the full angle range is scanned, shown in figure 5.6. For angles below 30 degree the sample reflection dominats the detected intensity. At higher angles the sample fluorescence is stronger; with the exception of when the diffraction condition is fullfiled, then the ($1/4$ $1/4$ 0)-peak becomes visible[3]. Comparing the incoming number of photons with the photons detected in the scattering peak reveals that the efficiency is of the order of 10^{-6}.

[2]The splitting into L_3 and L_2 is due transitions from the spin-orbit split $p_{1/2}$ and $p_{3/2}$ core levels.
[3]In order to detect the ($1/4$ $1/4$ $1/2$)-peak the sample has to be cut differently.

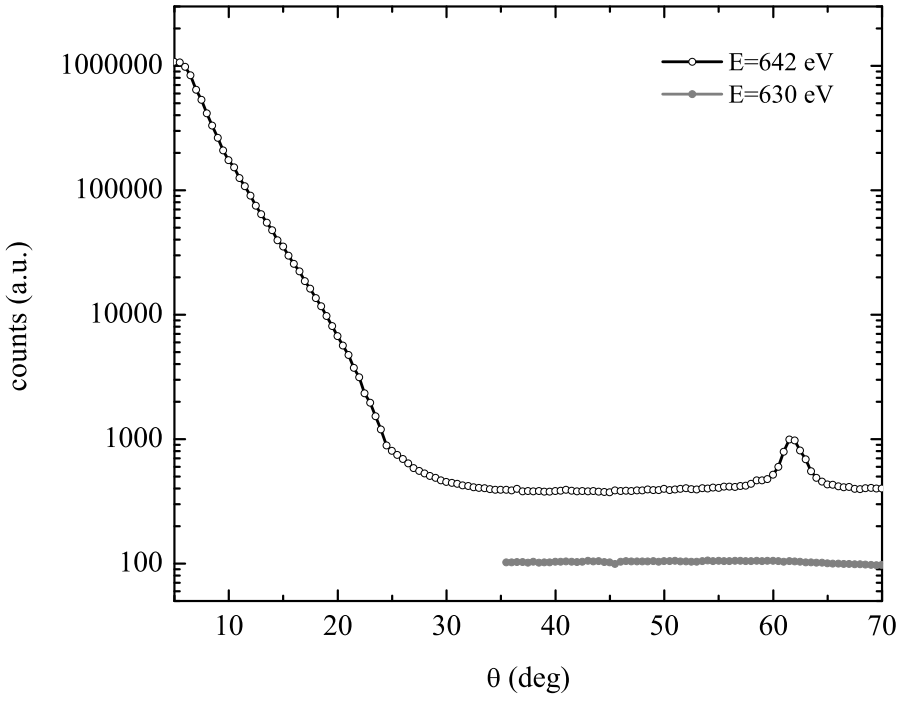

Figure 5.6: Scan over the full angle range. Up till 30 degree the sample reflection dominates the measured x-ray intensity. Above 30 degree only fluorescence of the sample is measured. When the radiation is on resoncance (E=642 eV) the orbital scattering peak is visible.

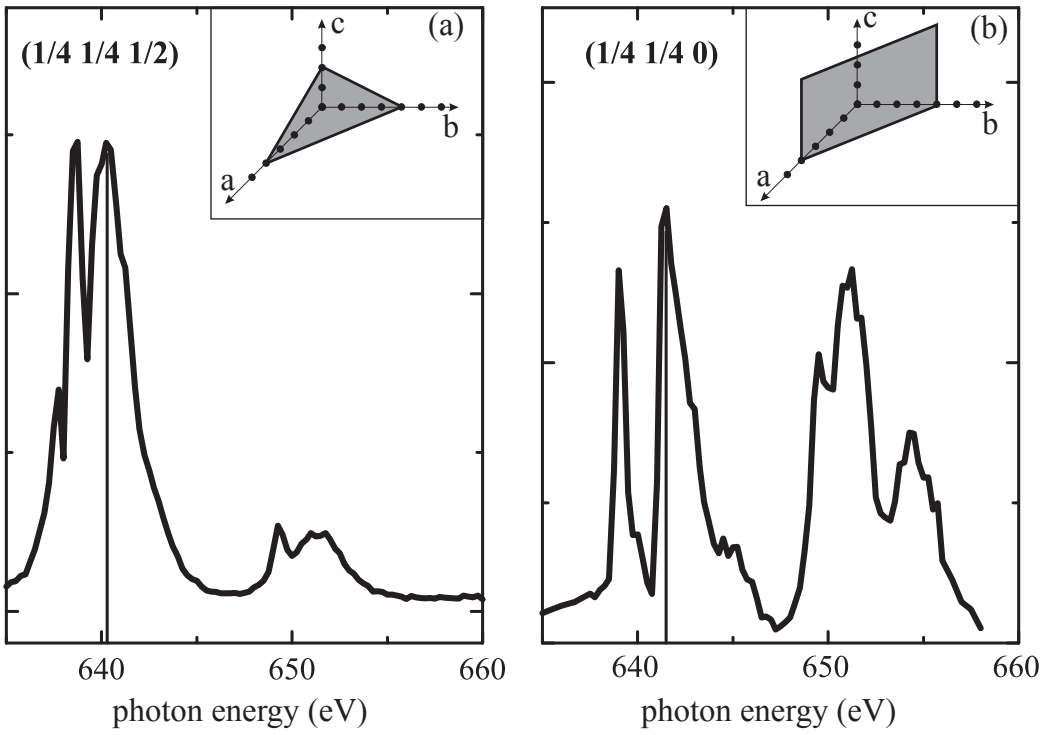

Figure 5.7: Static energy dependent diffraction peak, when the sample is cut along the (a)[112] or (b)[110] direction.

The azimuthal dependency[4] of the scattering intensity is regarded as the proof that the scattering arises from the orbital order [42, 69, 53]. Qualitatively this can be seen by looking at the occupied orbitals. The e_g state on the Mn^{3+} side is composed of a filled $3d_{z2-r2\uparrow}$ orbital and an empty $3d_{x2-y2\uparrow}$ orbital. On the Mn^{4+} the e_g orbital is empty. In the case of a filled $3d_{z2-r2\uparrow}$ orbital the transition can be expressed as $2p \rightarrow 3d_{x2-y2\uparrow}$. From this it can be seen that depending on whether the polarization of the x-rays is parallel or perpendicular to the local z axes a different scattering rate will be observed.

It is worthwhile looking at the intensity changes of the diffraction peak with the photon energy. Figure 5.7 shows the superlattice reflections at T = 25 K. By tuning the x-ray photon energy over the L-edge strong changes in scattering intensity are observed, the experimental procedure is explained in appendix A. Statically

[4]Rotation of the sample around the scattering vector.

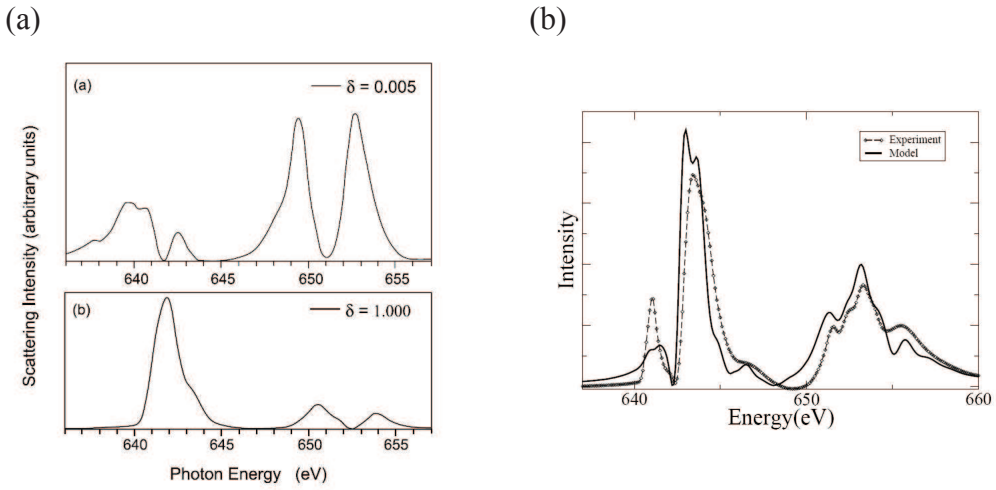

Figure 5.8: Theoretical spectra for the diffraction signal are shown. Figure a) presents spectra based on atomic multiplett calculation, for different strength of the Jahn-Teller distortion (top: no Jahn-Teller)[71, 43]. Figure (b) compares experimental and theoretical spectra. The simulation is based one a cluster calculation and reproduces the different peaks as well as their relative strength [72, 44].

this material has been extensively studied in the soft x-ray range [43, 44, 70]. The spectral features arise from the splitting of the d-levels, caused by a combination of Coulomb and Jahn-Teller interaction. In the former case the Coulomb repulsion between orbitals with the same spatial distribution splits the unoccupied $3d_{z2-r2\downarrow}$ and $3d_{z2-r2\uparrow}$ level. The Jahn-Teller effect, on the other hand, would lead to a splitting of the t_{2g} orbitals. This is due to their single occupancy according to Hund's rule [71].

This qualitative discussion implies that the Jahn-Teller and the Coulomb effect influences the energy spectra in a different manner. Attempts have been made to compare theoretical spectra with experimental ones and to attribute the features to their microscopic origin [71, 43] and [72, 44, 53]. In figure 5.8 they are reproduced from their respective publication. Static experiments and simulations suggests that the features at L_3 are strongly influenced by the Jahn-Teller distortion. This can be seen in figure 5.8 a) where the energy spectra is calculated for different strength of the Jahn-Teller distortion, measured by the parameter δ.

Time-resolved experiments could help to clarify the situation more; when a specific

degree of freedom is selectively excited the corresponding changes of the spectral features could be monitored on the ultrafast timescale. It would be expected that spectral features depending on the Jahn-Teller distortion have a response time limited by the phonon frequency, while features caused by the electronic degree of freedom react promptly.

Chapter 6

Time-resolved technique

6.1 Introduction

The study of dynamics is an important direction in science. Initially, time-resolved experiments where performed mainly on macroscopic objects. The first reported experiments of a 'fast' dynamical process was performed in the 1870's by E. Muybridge [73]. It aimed at solving the question of whether a horse had all four hooves above the ground at any time during the gallop. Muybridge used an array of cameras along the path of the horse. The horse triggered mechanical shutters on the cameras while passing by. In this way Muybridge achieved, at the time, an unprecedented time resolution. Later, the technique was advanced using flashes of light synchronized to the investigated dynamic. This stroboscopic recording technique was developed by Edgerton in the 1920's at the Massachusetts Institute of Technology [74] to study synchronous motors, it allows to 'freeze' dynamical events in time. Edgerton later became famous for his studies on more lively objects, such as the dynamics during a golf swing shown in figure 6.1.

Almost hundred years after Muybridge, in 1967 the Nobel Prize was awarded to Eigen, Norrish and Porter [75] for a new type of spectroscopy, that studied the

dynamics of a chemical reaction. Dynamics where initiated by depositing energy into a chemical compound at equilibrium with a strong 'pump' light pulse. The dynamics triggered in this way were subsequently measured with multiple, delayed, probe pulses. The great innovation was to start at equilibrium and to initiate the dynamics at a well defined point in time. The temporal resolution of such an approach is then only limited by the duration of the pulses (pump and probe).

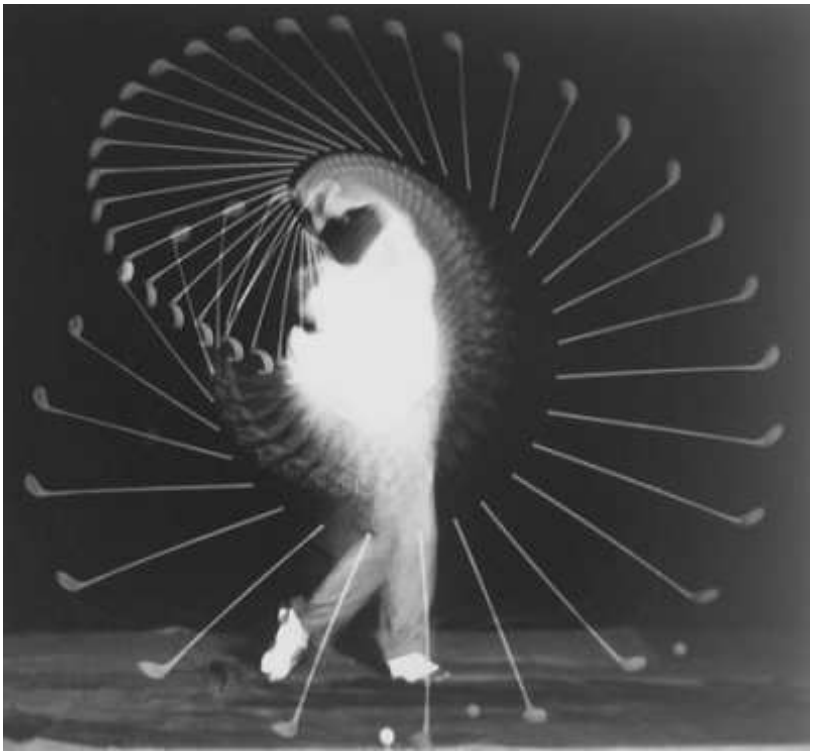

Figure 6.1: Example of a time-resolved experiment using the stroboscopic technique. In contrast to the pump-probe technique the dynamic here is only initiated once and then mapped using many synchronized light flashes, taken from [74].

In contrast to the stroboscopic approach, where many synchronized light flashes interrogate with the ensuing dynamics, most pump-probe experiments to date only use one pair of pump and probe pulse, see figure 6.2. When a single pair of pulses is used the evolution of the dynamics is recorded many times, while only the relative delay between the two pulses is adjusted.

Using a strong pump pulse allows to drive systems out of their equilibrium condi-

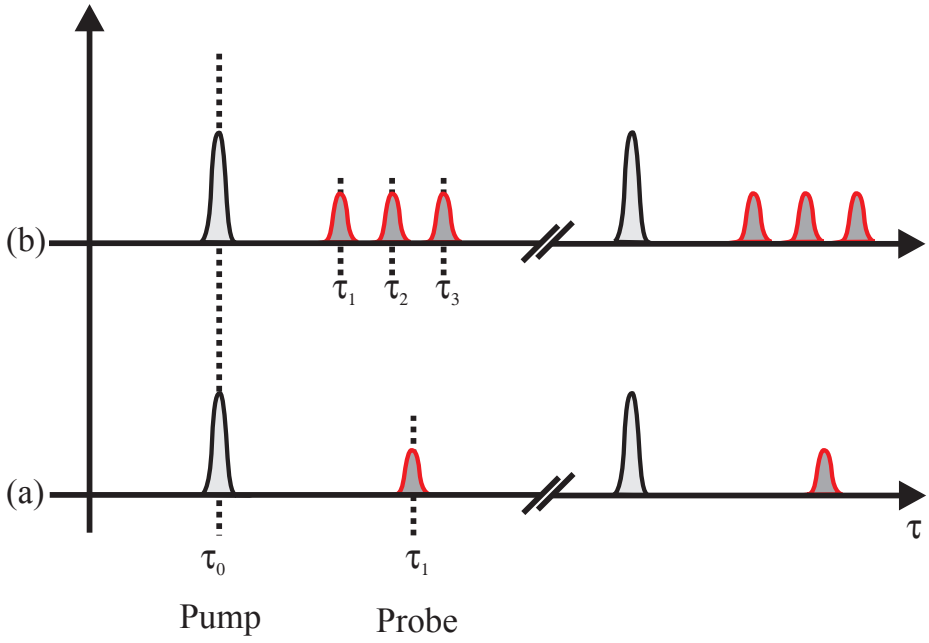

Figure 6.2: Pump and probe pulse are shown on the time axes. In (a) one probe pulse is used, different temporal delays are recorded consecutively, (b) shows the stroboscopic approach where many probe pulses are used to sample the dynamic at once.

tion instead of only measuring how a system reaches a new equilibrium state. In this way the scope of this pump-probe technique could be expanded greatly, for example into the area of solid state physics. Furthermore, it lifts the restriction of measuring as fast as the process occurs. This made the measurement independent of the reaction speed and in principle it enables the ultraslow measurement of ultrafast processes. Weak signals can be measured by integrating at a give delay for many hours (given the stability of the setup). In order for a pump probe experiment, utilizing a single probe pulse, to deliver reliable information, different pump pulses have to find the sample in the same ground state. Due to great technical improvements Shank extended the pump-probe technique into the femtosecond range [76]. Using these technical advances Zewail was able to measure reaction times with a resolution in the range of the fundamental timescale of the atomic motion (femtosecond) [77]. The race for shorter pulses is still ongoing and the limit is now in the attosecond range [12]. This allows experiments that measure the motion of electrons during a chemical

reaction. For example, an electron wavepacket completes a single revolution around the hydrogen core within 152 attosecond [78].

In addition to the search for ever shorter pulses, another area of research is to tailor the pump and probe pulse to specific properties of the material. The aim here is to selectively deposit energy into specific degrees of freedom and then probe how other degrees of freedom are affected. An ideal experiment for example would be to selectively excite a specific type of lattice vibration in the system [13] and then use femtosecond x-ray diffraction [15] to probe the response of the lattice or resonant soft x-ray radiation to measure the evolution of the ordering phenomena of the electronic degrees of freedom.

6.2 Photo-stimulated dynamics in manganites

Some of the properties of manganites can be changed through chemical doping. A more versatile approach to phase control is the application of external stimuli, such as magnetic fields [79], pressure [80], electric currents [81] and x-ray [82] radiation. In this way the properties can be controlled reversibly. Especially interesting for the high-speed data processing and storage industry is to probe dynamics following the excitation with visible light pulses. The demonstration of phase control was successfully achieved with pulses spanning over a wide wavelength range, from the terahertz [83] to the x-ray range [82]. The following paragraph gives a brief selection of significant and intriguing experiments to this field.

Measuring the photocurrent between two electrodes offers an opportunity to probe an insulator to metal transition. In this way the macroscopic parameter that classifies such a transition is directly sensed. This approach was pioneered by Miyano et. al.; They showed that light excitation leads to the formation of a permanent metallic state [84]. Figure 6.3 presents the voltage drop between the two electrodes as reproduced from the original literature. In a similar way the conducting pathways formed between the electrodes during this Insulator-Metal transition can be imaged. This experiment revealed that the transient conducting path was filamentary and lasted as long as a current flows between the electrodes [9, 10]. Still, due to limits in the detection process, the photocurrent cannot be detected with a time resolution better than a few nanoseconds.

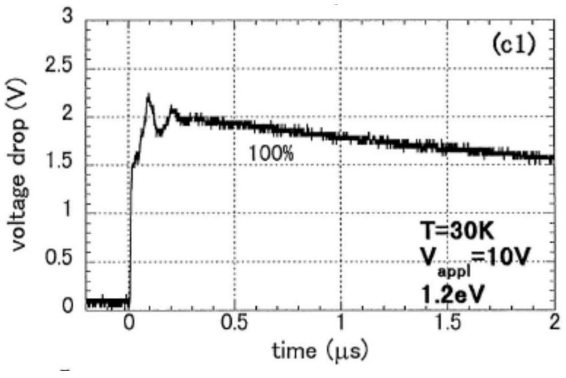

Figure 6.3: Photocurrent after laser excitation taken from [84].

In comparison, the use of light pulses allows to measure changes on the ultra-

fast timescale. When the reflectivity is probed on the ten femtosecond timescale, oscillations from the excitation of phonons and other quasiparticles emerge. A direct connection between the detected changes and their microscopic origin is not possible. Moreover, changes in reflectivity arise from the interaction of many degrees of freedom. A careful analysis of the response in the time domain enables a temporal filtering of changes caused by different degrees of freedom. For example, the analysation of reflectivity oscillations showed that light excitation can couple to the magnetic state [85], see figure 6.4. Wall et.al. irradiated the charge and orbital ordered phase (COO) of $LaMnO_3$ with ten femtosecond light pulses, resonant to the charge transfer excitation between Mn^{3+} and Mn^{4+}. This modified the magnetic exchange constant J, leading to perturbation of the equilibrium bond length. This demonstrated a complex coupling between light excitation and the magnetic state of the material.

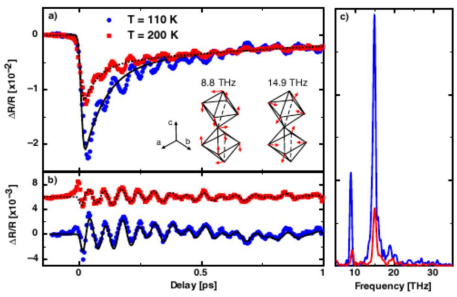

Figure 6.4: Reflectivity oscillation after ultrafast laser excitation taken from [85].

Connecting changes of macroscopic sample properties to their microscopic origin is also possible, to some extent, by analysing the polarization of the reflected light. Isihkawa et.al. [65] showed that the rotation of reflected, linear polarized, light is different for the COO phase compared to the unordered one. This change in optical anisotropy (or birefringence) was used by Ogasawara et. al. to detect changes in the COO order [54]. Intense 200 fs light pulses were found to melt the electronic order in $La_{0.5}Sr_{1.5}MnO_4$. The extension of this technique into the ten femtosecond range will be presented in chapter 7.

The polarization of the electromagnetic wave can also be used to study the mag-

netic state of a material. In the cubic system $La_{0.6}Sr_{0.4}MnO_3$ the spin dynamics was measured with time-resolved magneto-optical Kerr spectroscopy (TRMOKE). Here, changes in the polarization of circular light are detected, which is influenced by the sample magnetization. This allows to separate them from reflectivity changes. Thus it is possible to disentangle low-energy excitation from the delayed photo-induced demagnetization [86].

Also using TRMOKE Koopman et. al. [87] disentangled the magnetical and optical contribution on the few hundred femtosecond timescale. They investigated the relationship between optical excitation and magnetization. In the first few hundred femtoseconds after photo excitation they found a drop in magnetization and explained this on the ground of dichroic bleaching, providing evidence for a strong non-magneticc contribution to the magneto optical response on the femtosecond time scale.

Especially relevant for investigating magnetic structures is second harmonic generation (SHG). Generally forbidden in systems with space inversion symmetry, it occurs when this symmetry is broken by the distribution of charges or spins [88, 89, 90]. For example, it is found that below the Neel temperature of $HoMnO_3$ a second harmonic signal appears, and due to the characteristic tensor component χ_{ijk} the magnetic space symmetry can be distinguished.

As common theme of the above, it follows that the polarisation of reflected light can help to disentangle the different degrees of freedom, especially on the ultrafast timescale where other suitable probes are not available yet. Still, this is not an ideal approach as the microscopic changes are buried under the macroscopic sample response. It is possible that different degrees of freedom influence the polarization simultaneously, especially in a non-equilibrium condition.

A more selective way that directly accesses only the lattice degree of freedom, is to use hard x-ray diffraction. Beaud et. al. [91] used femtosecond x-ray radi-

ation generated by a storage ring, with a time resolution of 195 fs. The material $La_{0.42}Ca_{0.58}MnO_3$ was excited with 1.55 eV light pulses, resonant to the intra atomic $t_{2g}^3e_g^1(Mn^{3+}) \rightarrow t_{2g}^2e_g^2(Mn^{3+})$ transition [92]. Depending on the excitation fluence it was possible to separate two distinctive regimes: for low fluence a displacive excitation of A_g-phonons was observed. Above a threshold fluence the Jahn-Teller distortion is released, evidenced by the disappearance of the superlattice peak. Thus a complete phase transition occurs within the first picosecond.

A direct comparison between photoinduced and static phases can be achieved through XANES[1]. It is a very powerful tool to measure changes in the hybridization between for example the manganese ions and the oxygen ligands. The hybridisation between the manganese $3d$- and the oxygen $2p$-states directly influences the properties of the valence and the conduction band. Rini et. al. found that transient photoinduced XANES spectra resemble the ferromagnetic static spectra which can be reached when cooling the sample [83].

The following chapters present new contributions in this field. First, measurements on the ultrafast timescale of the optical anisotropy are presented. A discussion of the time-resolved diffraction chamber follows. Finally, measurements on the orbital and spin order in the photoexcited phase of the manganites $La_{0.5}Sr_{1.5}MnO_4$ are reported.

These examples illustrated that light excitation allows to switch an insulating to a metallic phase. Two avenues where presented: Firstly, exciting and probing the changes on ultrafast timescales. Secondly, the use of selective probes was demonstrated. In the following contributions in both directions are presented.

[1] X-ray Absorption Near Edge Structure

Chapter 7

Ultrafast photoinduced melting of the orbital order in $La_{0.5}Sr_{1.5}MnO_4$

7.1 Introduction

As previously discussed, there are several competing explanations for the onset of orbital order. It can arise from a Jahn-Teller driven lattice distortion or, alternatively, it can be attributed to an electronic exchange mechanism as explained by van den Brink [38]. However, a concensus on the matter has yet to be reached and it remains a hotly debated topic [44, 41, 71, 70, 93], see also chapter 3.5.

For a time-resolved experiment to be able to distinguish between the two competing scenarios it is necessary to have a time resolution that is better than the speed at which the lattice can react to an external perturbation. It was shown [94] that this is related to the frequency of the phonons. Depending on the type of phonon present, it can be related to the inverse of half the phonon frequency. The highest phonon modes reported in this material are in-plane Mn-O stretching modes at 693 cm^{-1} [95], corresponding to a half period of 24 fs. Therefore, a time resolution better than 24 fs would be required to separate electronic from lattice driven effects, following

the argument in [15]. On this short timescale the electron and lattice system have not thermalized [85]. Therefore, the coherent response of the system dominates the sample response.

In the prototypical compound $La_{0.5}Sr_{1.5}MnO_4$ the charge and orbital order can be probed using visible light [65, 42]. In this 'all-optical' approach the rotation of polarised reflected light pulses is analysed. This measurement can be performed on the ultrafast timescale, with suitable short pulses of light. Previous studies used 200 fs long pulses [54], too long to measure the dynamics on their natural timescale. Here, ultrafast measurements of the optical anisotropy after photo excitation are reported. To this end the system is disturbed with 16 fs pulses from its electronically ordered state. Changes in the orbital order are then probed by measuring the optical anisotropy. It is found that the sample response is limited by the integral of the cross correlation between pump and probe pulse. Also observed is the near-complete melting of the orbital order within the first tens of femtoseconds after photo-excitation.

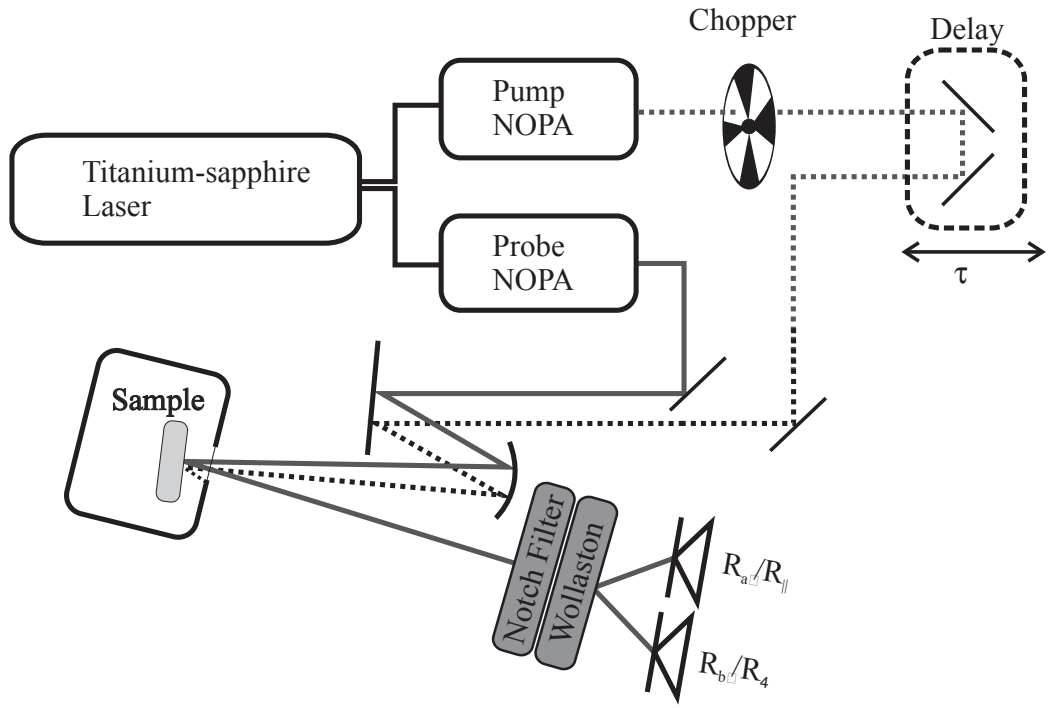

Figure 7.1: Experimental setup to measure the ultrafast optical anisotropy.

7.2 Experimental setup

Figure 7.1 shows the layout of the pump-probe experiment. A Titanium sapphire laser with a repetition frequency of 1kHz (KMLabs Dragon Series) feeds two identical non-collinear optical parametric amplifiers (NOPA). In the NOPA 800 nm 30 fs long input pulses are converted into shorter pulses with a tunable central wavelength. This work used 16 fs (FWHM) long pulses with a center wavelength that could be adjusted between 550 to 700 nm. The design of the NOPAs is taken from a paper by Cerullo et. al.[96]. The 800 nm input pulses are split into two arms: The first one is upconverted to 400 nm and acts later as an amplifing pulse. The second one is used to generate a broad and stable white light continuum and acts as a seed pulse. With a delay stage between the two arms it is possible to select a wavelength from the seed pulse that is amplified through mixing with the 400 nm pump light in a nonlinear crystal (BBO 1 mm thick and cut at 32°). The amplified bandwidth depends on the angle between the two beams inside the crystal and is adjusted to be as large as possible.

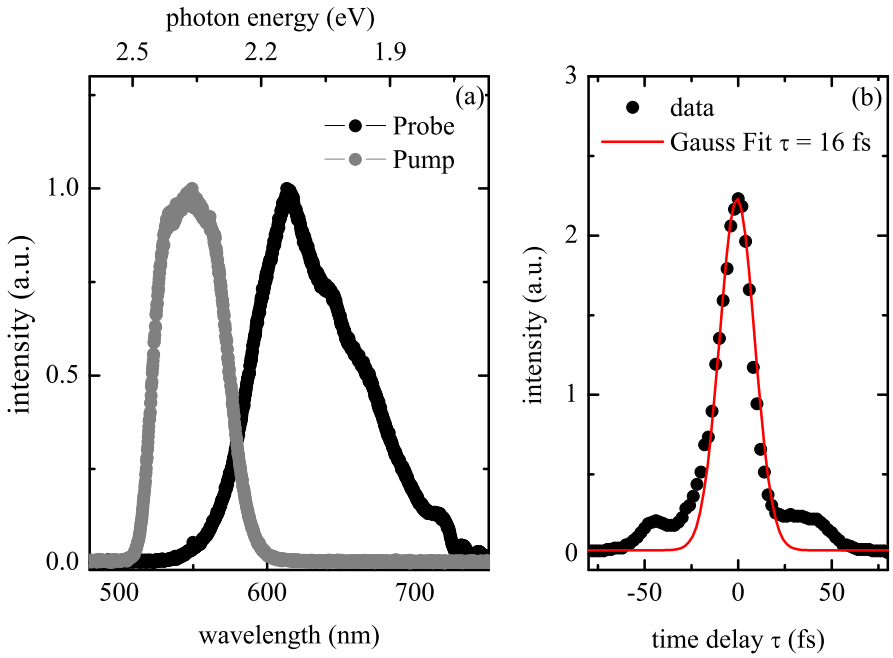

Figure 7.2: (a) Spectra of pump (560 nm) and probe pulse (630 nm) (b) Cross correlation between pump and probe pulse.

These amplified pulses are later compressed using several bounces on chirped mirrors to remove the temporal chirp and to deliver short pulses at the sample position. This pulse is used to excite the sample.

This process is repeated to generate a second, independent pulse. The pump pulse, with a central wavelength of 560 nm, was sent over a delay stage and modulated by a chopper. The wavelength of the probe pulse was tuned to 630 nm to maximize the anisotropic signal in the orbital ordered phase, according to [65]. Figure 7.2 a) shows the spectra and b) the cross correlation between pump and probe pulse.

A schematic of the experimental setup used to measure the polarization rotation of the reflected light is shown in figure 7.3. Before the light pulse hits the sample a polarizor fixes the polarisation state, so that it is aligned 45 degrees with respect to the principal axes (a', b'). After the reflection, a notch filter selects a narrow region (10 nm) around the center wavelength. The Wollaston prism is used to analyse the

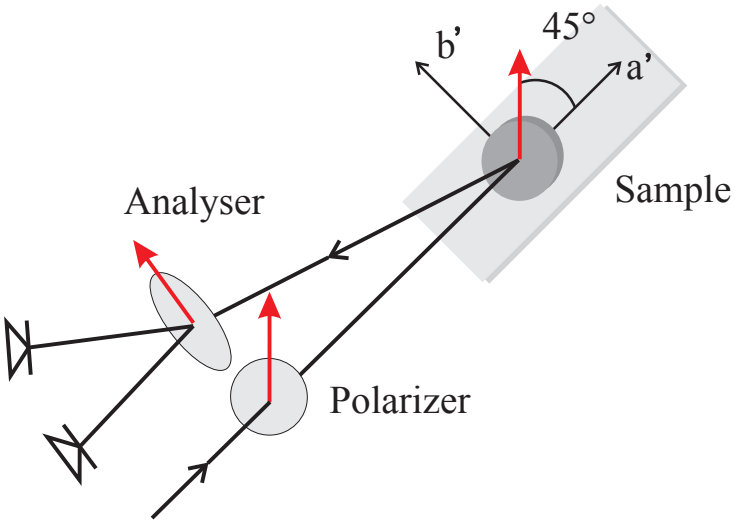

Figure 7.3: Experimental setup to measure the optical anisotropy.

polarisation state of the light. It separates the light into a parallel ($R_{\perp}$) and perpendicular ($R_{||}$) component relative to the incoming light vector. The light was detected with standard silicon diodes measured in a Lock-In difference detection scheme.

The beams are focused using a mirror with a focal length of $f = 200$ mm. This resulted in a spot size for the pump pulse of 90 μm and for the probe pulse of 50 μm. The maximum pumping power was measured to be P=640 nJ, which translates into a maximum excitation density at the sample position of 9.5 mJ/cm^2. The probe arm was attenuated by replacing a mirror with a neutral density filter so that no additional dispersion was inserted into the pulse, the power was measured to be 74 nJ. In order to measure the pulse duration and to determine time zero, the beams were sent into the BBO crystal by placing a mirror just before the sample.

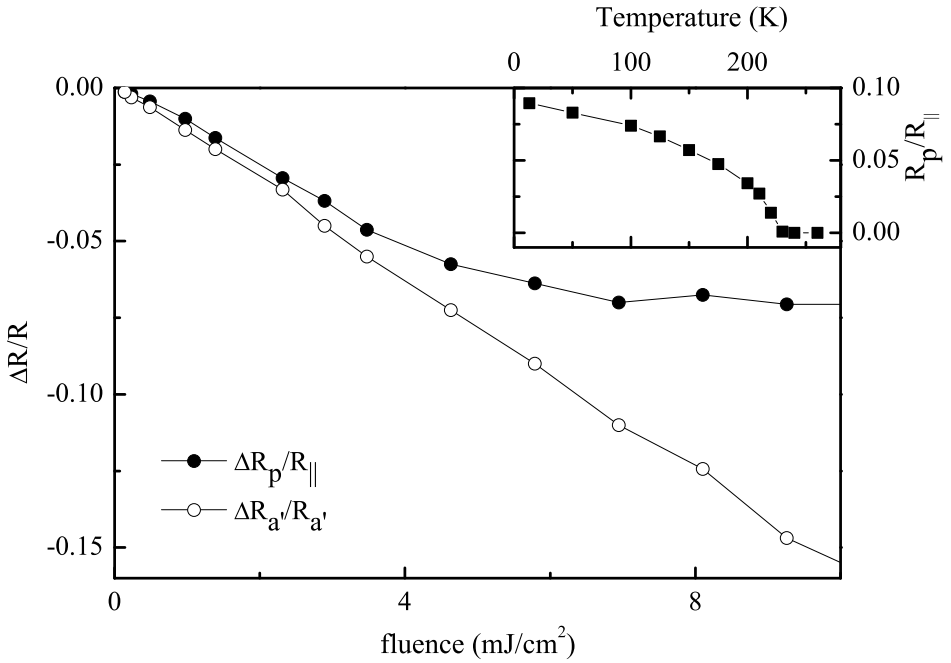

Figure 7.4: The relative change of the optical anisotropy with pump fluence (full dots) and of the reflectivity along the a' axes (open dots), with R_p-reflectivity perpendicular to the incoming direction and $R_{||}$-reflectivity parallel to the incoming direction. The inset shows the static optical anisotropy.

7.3 Experimental results

Figure 7.4 shows the change in the reflectivity (open dots) and the change of the optical anisotropy (filled dots) with fluence (sample temperature of 20 K). Remarkably, there is a difference between the reflectivity along the a-axis (R'_a) and the optical anisotropy signal ($\frac{R_\perp}{R_{||}} = \frac{R_{a'}-R_{b'}}{R_{a'}+R_{b'}}$)). If the light is polarized along a principal axis, the system does not show any saturation and the reflectivity decreases linearly with increasing fluence (measured at a pump probe delay of 200 fs after time zero). However, the change in the optical anisotropy signal settles to a constant value of 0.07 above 6 mJ/cm^2. This fluence corresponds to an excitation of 1 out of 10 manganese ions, or a density of 10 %. If the fluence is decreased towards zero, the change in the optical anisotropy follows with a near-linear behaviour. Also very small fluences are already inducing a measurable dynamic in the system, so that no threshold could be

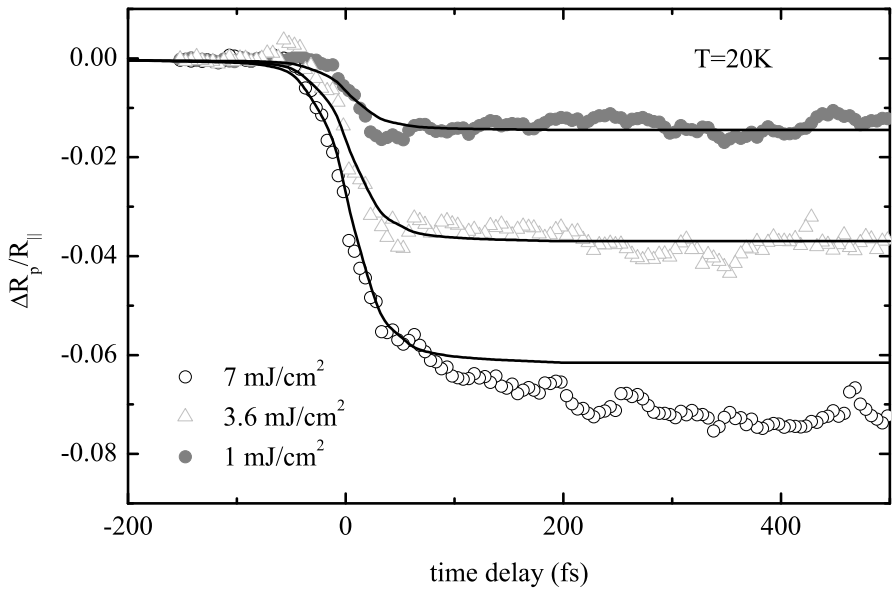

Figure 7.5: The birefringence signal for various excitation fluences as a function of pump-probe delay, the solid lines are the integral of the cross correlation signal between pump and probe pulse.

observed. This observation shows that the melting of the orbital order can already be initiated with very little activation energy. This contrasts with what has been reported in VO_2 [15, 97], in which photo excitation melts a Peierls distorted phase and the pump induced change was found to be slower than the pulse duration. This was interpreted to arise from the lattice relaxation as the limiting factor [94].

In Figure 7.5 the birefringence signal is plotted as a function of the time delay between pump and probe for three different fluences. The high fluence curve was measured in saturation as determined from Figure 7.4. The loss of birefringence ($\frac{R_\perp}{R_{||}}$) in saturation is strong, it drops to 30 % of the static value within the first 50 fs. The changes due to photo-doping are shown together with the integral of the cross correlation signal (scaled to the signal at 50 fs for each trace). This clearly shows that the timescale for the drop in birefringence is limited by the pulse integral, which it follows almost identically. This finding together with the threshold-less fluence

dependence points towards an electronic effect that stabilizes the orbital ordered phase.

These measurements show that, after photo excitation, the orbital order signal collapses at a resolution limited rate given by the integral of the cross correlation of the 16 fs pump and probe pulse. This is achieved for a photo-doping density of 10 %. This fast relaxation of the order points towards an electronic mechanism leading to the phase transition. Lattice effects such as the relaxing of Jahn-Teller phonons could still be involed but are limited to an overdamped contribution of the highest frequency phonons. Alternatively, the fast decline could also be explained by a mechanism similar to photo-bleaching where the occupancy of the ordered *d*-orbital system is promptly changed by the laser excitation making the system more isotropic. Even though this could explain the fast decline of the optical anisotropy it would not be expected that a reduction in signal amplitude of 70 % could be achieved with a photo-doping density of 10 %.

These measurements reveal that ultrafast changes can be induced on the few femtosecond timescale. In order to learn more about the underlying interactions a more specific probe is needed. To address this, a time-resolved resonant x-ray diffractometer was developed. The setup and some experiments are presented in the next chapters.

Chapter 8

Time-resolved resonant x-ray diffractometer

8.1 Introduction

The theoretical background of resonant x-ray diffraction (RXD) has been introduced in chapter 4. The current one aims to describe the experimental extension of RXD into the time-domain. It starts with a brief introduction to the genarating principles and to the characteristics of x-ray radiation. There follows a description of the time-resolved x-ray diffractometer that was designed and build during this thesis.

8.2 Generation of x-rays

The primary source for x-rays was the Diamond Light Source in the United Kingdom [98]. Operational since early 2007 it delivers high brilliant electromagnetic radiation [99] extending from the infrared (2.4 meV) to the ultra hard x-ray range (150 keV). The stored electrons have an energy of 3 GeV at a current of 300 mA. It operates in the so called 'top-up' mode [100], where the lost charge is added regularly during the operation. This leads to an intensity variation of the x-rays on the sample of less

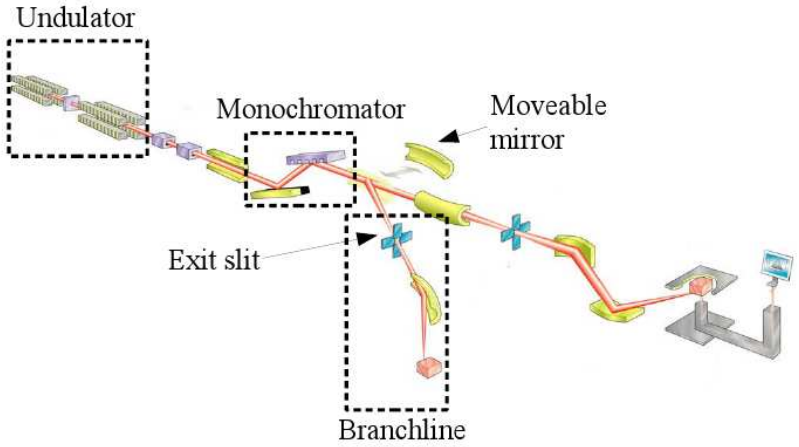

Figure 8.1: The figure shows the schematic of the beam line I06 at Diamond Light Source in the UK.

then one percent.

8.2.1 Beamline I06

The x-ray experiments presented in this thesis were performed on the branch line of beamline I06 (dotted boxes in figure 8.1) at the Diamond Light Source. X-rays are generated from the electron bunch in an APPLE 2 undulator, which provide complete polarisation control by changing the relative alignment of the magnetic poles. For linear vertical light the energy can be varied between 130 - 1500 eV and 80 - 2100 eV for linear horizontal light. After the undulator a plain grating monochromator spectrally filters the light, with a minimal energy resolution of 40 meV.

The spot sizes were measured using the knife edge technique. In figure 8.2 the x-ray beam profile is shown. X-ray radiation is converted into the visible using a phosphor screen on the sample holder and then captured with a CCD camera.

8.2.2 Camshaft mode

The Diamond Light Source storage ring allows the storage of 936 electron bunches which are 2 ns apart. When the ring is completly filled the repetition frequency of

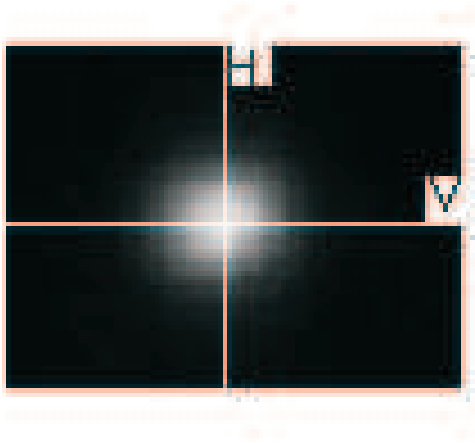

Figure 8.2: The beam profile at the sample position is shown.

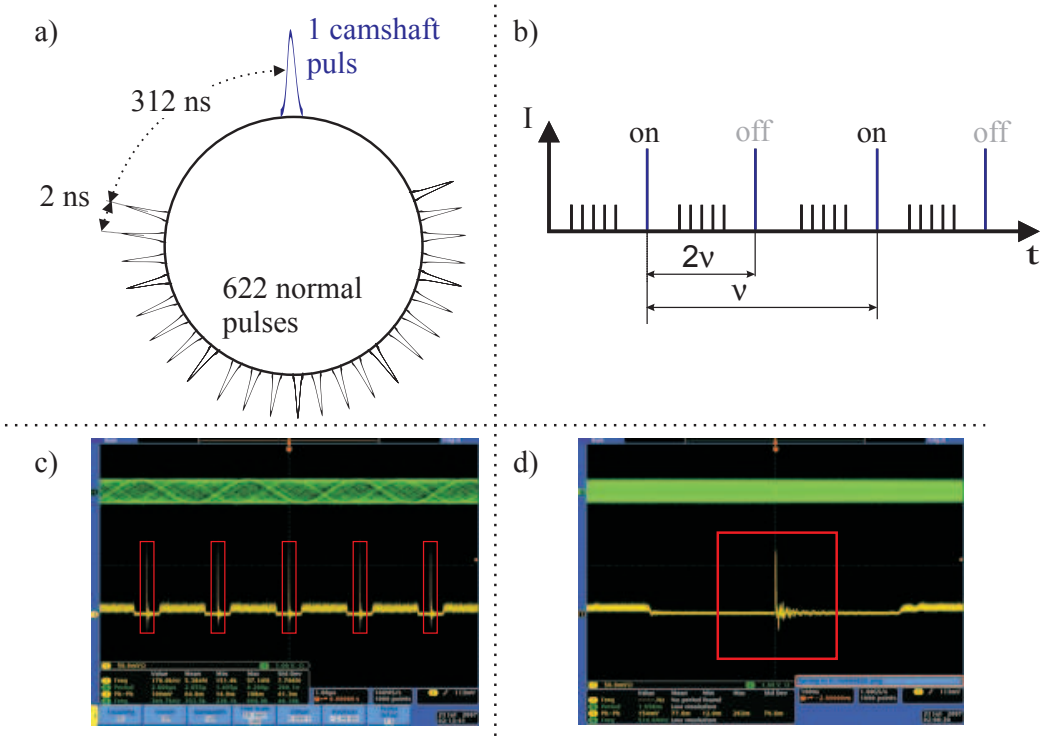

Figure 8.3: Shows the bunch structure in the camshaft mode of Diamond Light Source from different perspectives as explained in the text.

Single bucket revolution frequency	533.82 kHz
X-ray repetition frequency (master frequency)	499.65 Mhz
Pulse duration in normal operation	80 ps
MIRA repetition rate	83.275 MHz
MIRA oscillator master clock	83.275/2 MHz
REGA repetition frequency	11 KHz - 266.91 KHz

Table 8.1: Important frequencies of the storage ring and laser.

the x-rays is 499.654 MHz. Every single electron bunch has a revolution frequency of 533.82 kHz.

In addition to the standard filling pattern, where two-thirds of the ring is filled with equally spaced electron bunches, there are several special filling patterns. The filling pattern used for time-resolved experiments is the 'camshaft' or 'hybrid' mode. This special filling pattern is shown in figure 8.3:

a) schematic filling pattern of the ring in real space

b) schematic of the intensity over time

c) trace of several revolutions recorded on an oscilloscope using an avalanche photo diode

d) a closer examination of a single revolution.

Similar to the standard fill, two-thirds of the ring is filled with electrons (the multi-bunch) while the other third stores only one electron bunch. This individual bunch is separated by several hundred nanoseconds on either side and is refered to as 'camshaft' or timing pulse. The gap is required to allow enough time for the electronics to gate the signal generated from the 'camshaft' pulse. Since there is a wide gap on either side it is possible to store ten times more charge in the 'camshaft' pulse (5.6 nC) compared to the multibunch pulses (0.4 nC).

8.2.3 Low-alpha mode

The longitudinal spatial extent of the electron bunch defines the duration of the generated x-rays. However, due to the Coulomb repulsion, electron bunches with a high charge cannot be compressed in modern day storage rings, as the Coulomb repulsion between the electrons limits the region in space to which they can be compressed. Different techniques have been employed to create short x-ray pulses in storage rings. Among them is the slicing method [101] or the 'low-alpha' mode [102]. Both methods reduce the pulse width at the expense of x-ray flux. With femtosecond slicing, it is possible to generate x-ray pulses as short as 50 fs [103, 104] but the intensity is too weak to generate an x-ray flux that allows soft x-ray diffraction, except for materials with exceptional high diffraction efficiency [105].

A technique that provides more flux, albeit at the expense of longer pulses, is the 'low-alpha' mode. It refers to a mode where modifications to the electron filling pattern of the storage ring are used to reduce the longitudinal width of the electron buckets. Namely, the momentum compression factor alpha is changed, leading to steeper electron buckets [106, 107]. The shortest pulses reported are 1.6 ps FWHM with a charge of 4 pC from Bessy 2 [102]. Chapter 9 reports on measurements in the 'low alpha' mode at Diamond Light Source, where a charge of 64 pC was used to generate 10 ps (FWHM) pulses. This was the shortest pulse duration that allowed the detection of a sizeable number of scattered photons. For comparison, the bunch length in normal operation is measured to be 80 ps when 6 nC of charge is stored. In figure 8.4 the filling patterns for normal mode operation, and for 'low-alpha' operation, are shown.

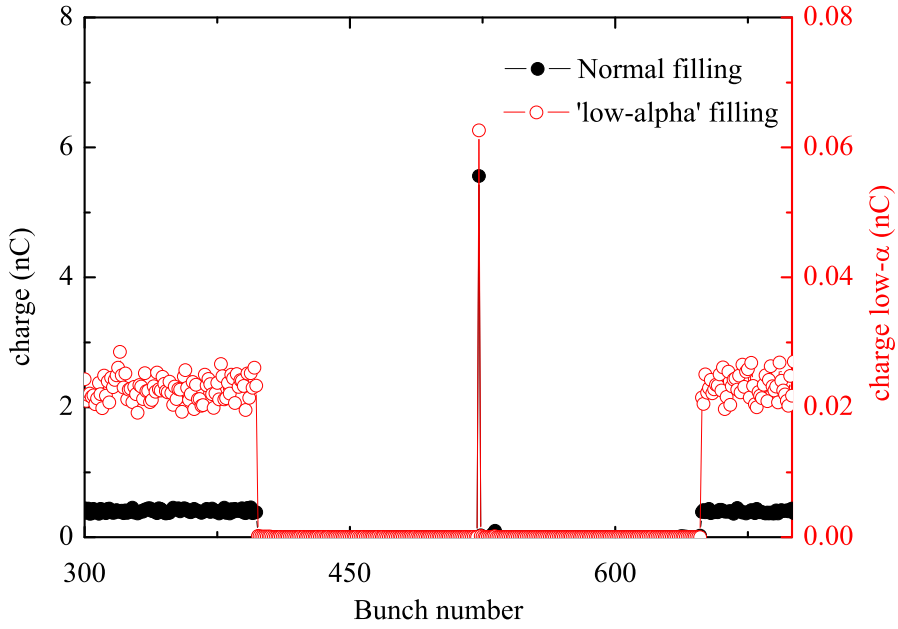

Figure 8.4: Comparison of the charge in the 'low-alpha' mode (red) with the normal mode filling pattern (black). In the 'low-alpha' mode the charge in the timing pulse is roughly a factor of 100 less.

8.3 Time-resolved diffractometer

8.3.1 Chamber layout

A schematical layout of the excitation and scattering geometry and the experimental chamber are shown in figure 8.5 and figure 8.6, respectively. The chamber is equipped with a Turbo and an Ion pump, allowing a base pressure better then 10^{-9} mbar. X-rays enter the chamber through a 2 mm diameter hole in a silver mirror. This 'holey mirror' geometry is used to couple x-ray and visible pump light collinearly into the chamber, reducing non-collinear temporal smear and aiding in the spatial overlap, see inset in figure 8.5. The x-rays hit the sample at an angle θ and are diffracted according to the Bragg equation

$$d \sin \theta = \frac{\lambda}{2} \, . \tag{8.1}$$

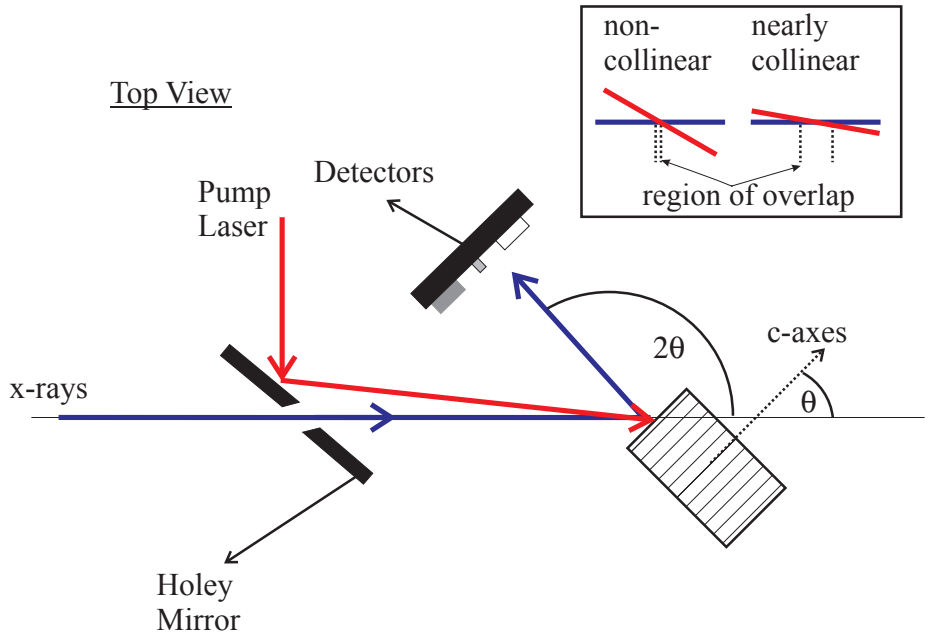

Figure 8.5: The diffraction geometry is shown. The inset illustrates the advantage of the 'holey-mirror' configuration that allows a near collinear propagation between the two beams leading to an increased overlap depth in the propagation direction.

The diffracted photons are captured with a detector at an angle of 2θ located 200 mm away. The diffractometer is based on a $\theta - 2\theta$ design and has independent manipulators for the sample (θ) and the detector rotation (2θ). The sample is fixed to a liquid helium flow cryostat from Oxford Instruments, allowing control of the sample temperature between 5 and 400 K. A commercial UHV manipulator holds the cryostat and is mounted from the top, providing 4 degrees of motion, see figure 8.6 (a). The degrees of motion are:

1. rotation (θ);
2. translation of the sample parallel to the beam (x);
3. translation perpendicular to the beam (y);
4. vertical motion (z).

The detector assembly is mounted from below and fitted with a differentially-pumped rotation and a linear translation stage (z motion) to move the detectors up

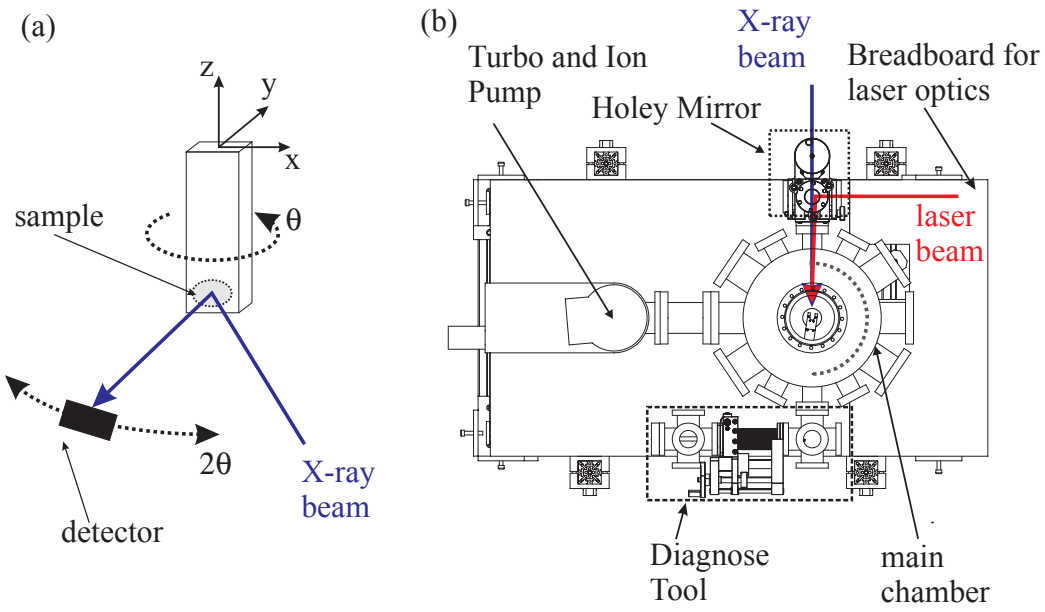

Figure 8.6: (a) Schematic to illustrate the degrees of motion of the diffractometer. (b) Drawing of the diffraction chamber viewed from the top.

and down. The detector arm has a length of 200 mm and holds an array of detectors for different purposes which will be described more thoroughly in the next section.

Downstream of the main chamber a second side chamber houses a fixed detector array with an avalanche photodiode (C30902SH from Perkin Elmer) and a static photodiode (AXUV100 from International Radiation Detectors). The avalanche photo diode is used to measure the temporal delay between x-ray and optical pulses. The static diode can record the intensity of the direct x-ray and laser beam, and is used in the alignment procedure for finding the spatial overlap between pump and probe. It is also for aligning the sample to the centre of rotation.

All rotation stages have a reproducibility of better then ± 0.01 deg and the linear motions are better then ± 10 μm. Motors are controlled via the computer system EPICS and the data acquisition is done in GDA, both developed at the Darsebury Synchrotron and at the Diamond Light Source. Alternatively the complete system can be controlled by a personal computer and Labview.

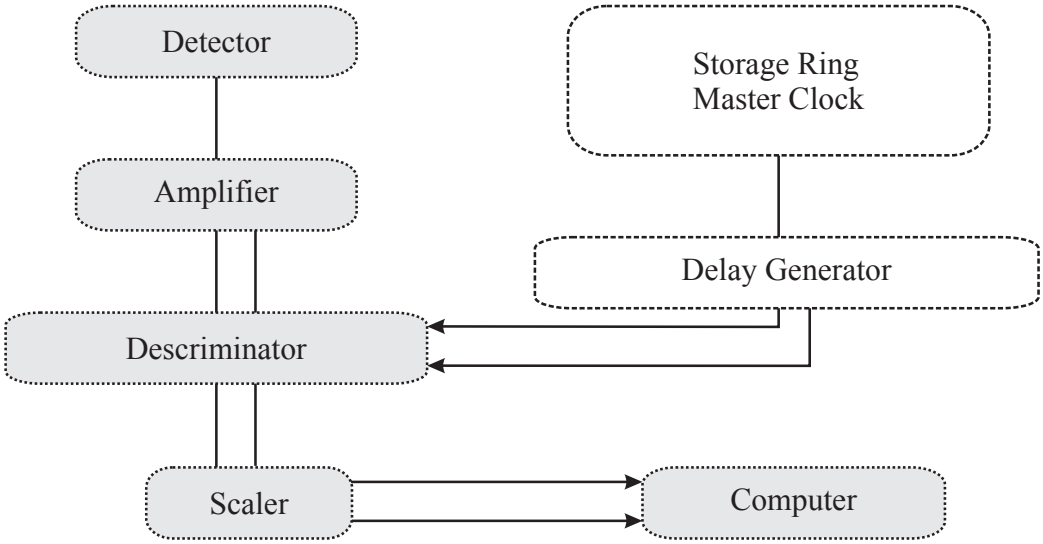

Figure 8.7: Shows the detection scheme that was used for the time-resolved diffraction measurements. In the top left corner the signal is detected in the detector and represented in the bottom right corner as counts in the computer. See text for further explanation.

8.3.2 Detection system

In figure 8.7 the flow diagram of the detection scheme is shown. It starts at the top left corner with the detector and finishes in the bottom right corner with a signal in the computer.

The detector has to fulfil several conditions:

- fast to resolve the bunch structure from figure 8.3;
- able to detect single photons;
- completely solar blind to the 1.6 eV pump photons.

A multichannel plate (MCP) naturally combines all these aspects (Photonis APD MINITOF 8). The MCP converts the incoming x-rays into electrons with an efficiency of 10 % and a gain of 2000. It has an active area of 8 mm. The signal from the detector is coupled out of the chamber using a 50 Ω SMA feed-through and is subsequently amplified. The amplifier (Ortec Instruments 9306) has a gain of 36 dB with a broad bandwidth of 1 Ghz, this preserves the bunch structure during the amplification. The

amplifier has two identical output ports. The amplified signal is then fed into two identical gated discriminators, together with a gate signal that is generated from a delay generator (DS 535 Stanford Research) synchronized to the master clock of the storage ring. The gate signal triggers the discriminators. One discriminator measures the laser 'on' signal and the other measures the laser 'off' channel. The signal from the discriminator is read out with a scaler card delivering the detected x-rays per second. The use of two discriminators allows the measurement of the signal in the photoexcited phase and, with every other pulse, a reference signal when the sample is in its ground state. In figure 8.3 b) this differential detection mechanism is shown. To make this measurement possible the repetition rate of the laser has to be smaller then half the revolution frequency of the camshaft repetition rate ($\nu_{laser} < \frac{533.82}{2}\ kHz$).

8.3.3 Laser system

The laser system is a commercial system from Coherent. Ultrafast laser pulses are generated in the oscillator (MIRA), which is used to seed a regenerative amplifier (REGA). Both the oscillator and the amplifier are pumped by the same Verdi V18 pump source making this system very stable and easy to use. In order to synchronize the laser and the storage ring the cavity of the MIRA is matched to exactly one sixth (83.275 MHz) of the storage ring master clock frequency. The stabilization is achieved via an electronic feedback loop, controlled by a commercial device (Syncrolock, Coherent). Figure 8.8 shows a flow diagram of the feedback loop.

The Synchrolock receives the frequency from the storage ring master clock (1) and the oscillator frequency (2) from an external photodiode. The jitter between the two pulses is minimized by adjusting the length of the oscillator cavity (3), using a piezo element on the end mirror. The manufacturer specifications are a jitter of less than 500 fs. Whilst the repetition frequency of the MIRA is locked the frequency of the REGA system can be adjusted from 266.91 kHz (exactly half the revolution

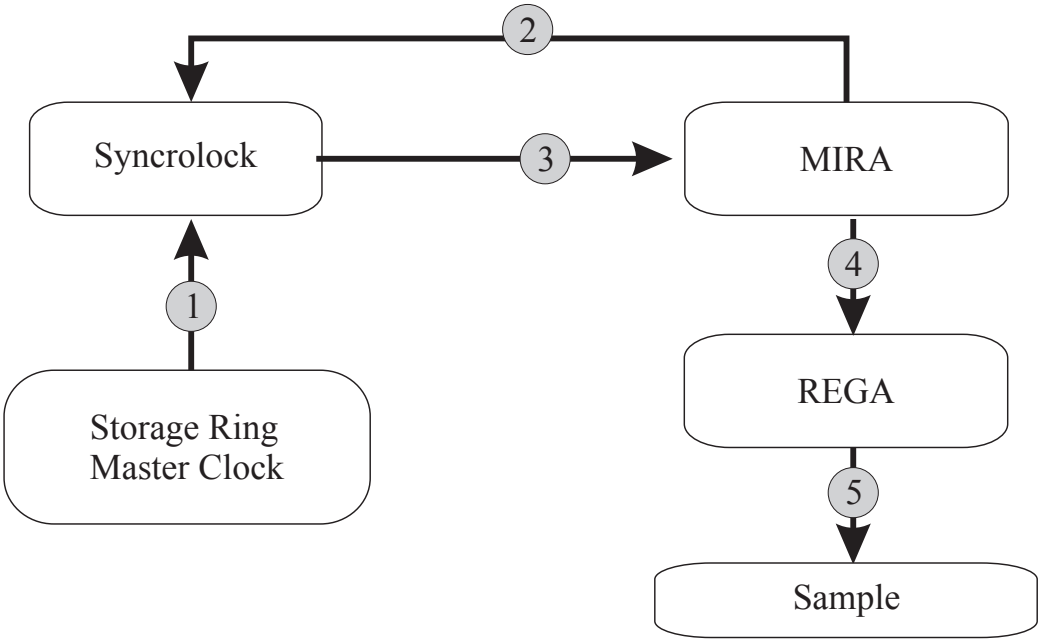

Figure 8.8: Shows a schematic of the synchronization of the Laser oscillator (Mira) with the storage ring. The phase looking between the pulses is achieved via an active feedback loop controlled from the Syncrolock.

frequency of the storage ring) down to 11 kHz. Depending on the repetition frequency the maximum pulse energy of the REGA is 4-6 μJ at the sample, with a pulse width of 200 fs.

8.3.4 Controlling the delay between pump and probe

Temporal synchronization of the optical pump and x-ray probe pulse is accomplished by a combination of electronic and mechanical delay. Gross temporal alignment is achieved by selecting which oscillator pulse is used for amplification. The delay achieved in this way is an integer multiple (n) of the oscillator clock (half the repetition frequency) $t_c = n \cdot 2/83.275$ Mhz $\approx n \cdot 24$ ns.

A finer delay can be generated by changing the phase delay in the synchrolock. This allows a continous adjustment between 0 - 12 ns or between 12 - 24 ns depending on an internal setting in the controller of the amplifier system.

The finest temporal adjustment is accomplished by using the mechanical delay. A

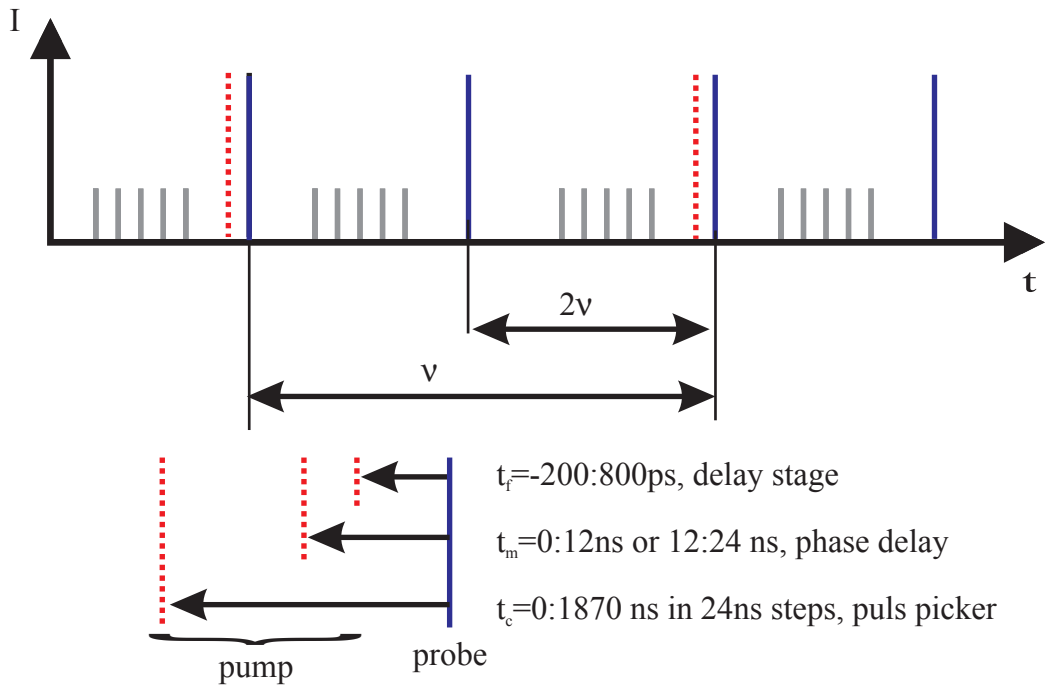

Figure 8.9: Illustrates the different delays that can be used to generate a temporal separation between the laser pump source and the x-ray probe source.

standard Newport motor is used giving a full range of 1 ns and a temporal resolution of 1 fs, in figure 8.9 the delays are illustrated graphically.

Chapter 9

Metastable electronic order in a photo excited manganite

9.1 Introduction

This chapter reports on measurements using the technique of time-resolved resonant soft x-ray diffraction (SXRD), the dynamics of charge and orbital order in the single-layer, half-doped Manganite $La_{0.5}Sr_{1.5}MnO_4$ are studied. Light excitation is found to melt CE antiferromagnetic order non-thermally, melting spin correlations between planes and altering the balance between super-exchange and Jahn-Teller-mediated orbital ordering within each plane.

9.2 Experimental setup

A femtosecond laser was synchronized to trains of soft x-ray pulses from the I06 beamline at the Diamond Light Source, making it possible to perform optical-pump resonant soft x-ray diffraction probe experiments, with a time resolution limited by the duration of the x-ray pulses, approximately 50 ps in normal operation and 10 ps in 'low-alpha' operation, as explained in chapter 8. Superstructures were clearly

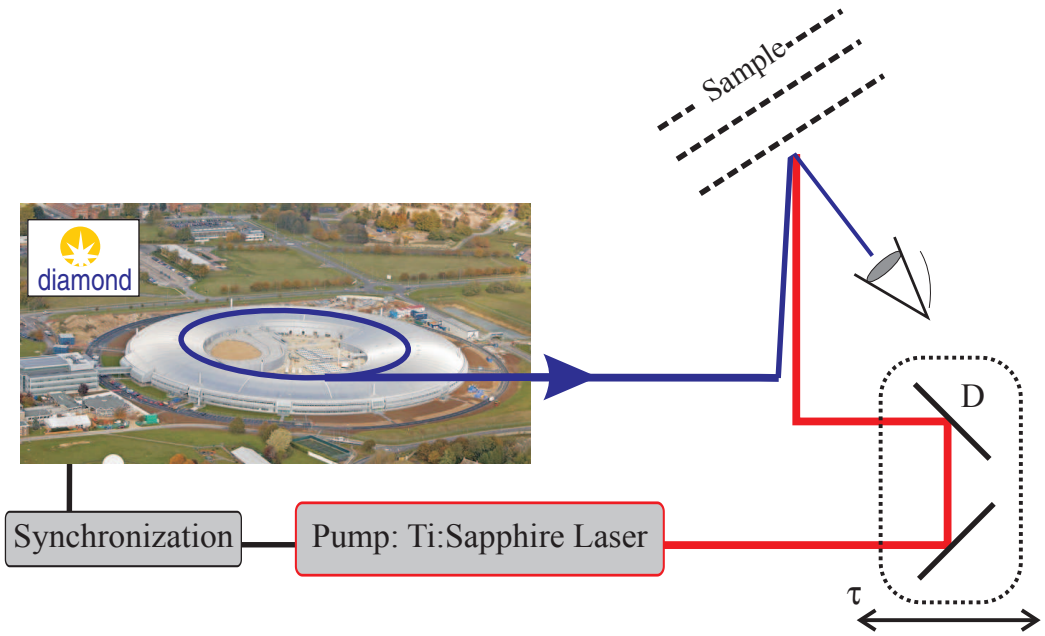

Figure 9.1: Schematic of the technical layout of time-resolved soft x-ray resonant diffraction.

resolved statically as well as dynamically, despite the significant reduction in x-ray flux caused by gating only less than one pulse per 20000. $La_{0.5}Sr_{1.5}MnO_4$ was photo excited with 200 fs laser pulses at a wavelength of 800 nm (1.6 eV), with the light polarized in the ab plane. The x-ray radiation was set to vertical polarization and to an energy resolution of 0.14 eV. For the measurements the x-ray spot size was measured to be 100 μm while the laser spot size was 150 μm.

9.3 Time- and energy-resolved dynamics

Figure 9.2 a) and 9.2 c), report the time-resolved photo-induced changes in diffraction for the (1/4 1/4 1/2) magnetic and for the (1/4 1/4 0) orbital peak. The plotted data are relative changes between laser 'on' and laser 'off' output of the discriminators. Measurements were performed at 641.5 eV and 640.25 eV near the Mn L-edge. Figure 9.2 a) shows the decrease in antiferromagnetic order along the c-axis, proportional to the (1/4 1/4 1/2) scattering signal, which was completely melted for all excitation

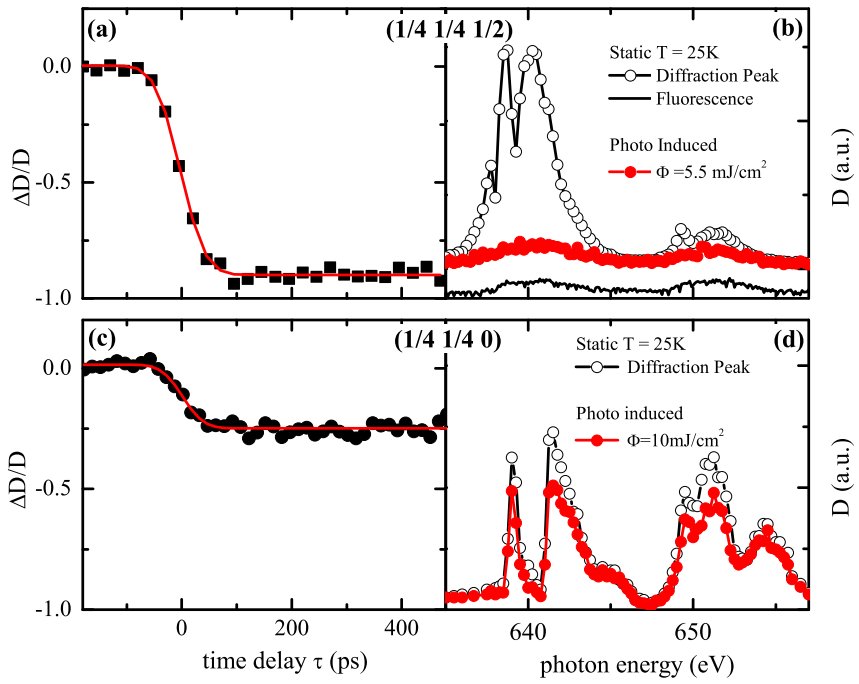

Figure 9.2: Photo-induced normalized change of the diffraction signal ($\Delta D/D$) for the (1/4 1/4 1/2) (a) and the (1/4 1/4 0) (c) peak. The panels (b) and (d) are showing the amplitude of the diffraction signal at a pump-probe delay time τ=200 ps (full red dots) in comparison to the one the static trace (black open dots).

fluences above 5 mJ/cm^2. The energy-resolved curves show a complete suppression at all wavelengths (see figure 9.2 b), leaving a weak, structureless signal with the same wavelength dependence as off-axis fluorescence. The off axis fluorescence signal was collected at fixed scattering angles of $\theta = 45$ deg, $2\theta = 90$ deg while the incoming photon energy is tuned over the absorption edge. The recorded fluorescence is directly related to the absorption of the crystal and agrees well with total electron yield measurements [108].

Figure 9.2 d) shows the energy dependence of this (1/4 1/4 0) orbital order peak at a time delay of $\tau = 200$ ps after photo excitation, along with the static diffraction spectrum taken before photo excitation. In contrast to the magnetic ordering, the photo-induced reduction of two-dimensional orbital order was measured to plateau of at 25%, even when the excitation was increased to 10 mJ/cm^2. These results show

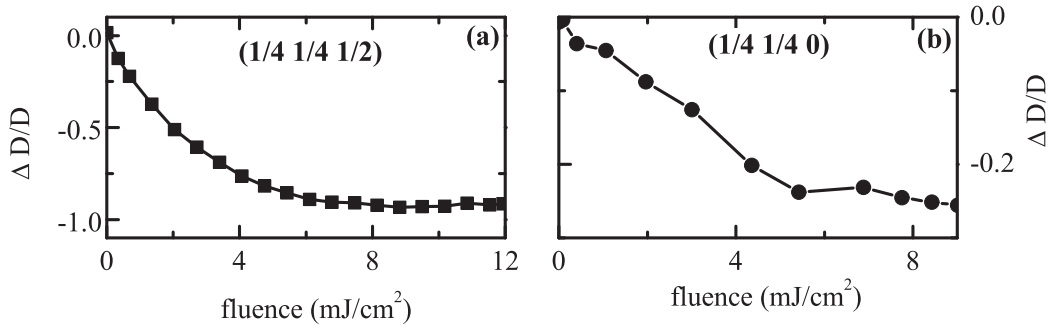

Figure 9.3: Fluence dependent scans of the change in diffraction intensity ($\Delta D/D$) for the (1/4 1/4 1/2) and (1/4 1/4 0) peak at a sample temperature of 25 K measured at a pump-probe delay $\tau = 200$ ps.

that photo excitation with 1.6 eV light pulses can cause a complete reduction of the signal that arises from the antiferromagnetic inter-layer coupling in the c direction. On the other hand, the diffraction signal due to the in-plane orbital order is only partially reduced by the photo excitation. As the antiferromagnetic and orbital ordering occurs at different temperatures, a possible explanation of this data would be that the ordering phenomena have a different dependence on the fluence. Thus a complete extinction for the orbital ordering signal may also be possible at higher pumping power. Therefore, as a next step the change of the diffraction signal at different fluencies was measured.

9.3.1 Dependence on the excitation fluence

In figure 9.3 the fluence dependent signal at a particular energy ($E_{\frac{1}{4}\frac{1}{4}\frac{1}{2}} = 641.5$ eV, $E_{\frac{1}{4}\frac{1}{4}0} = 640.25$ eV) and a fixed delay of $\tau = 200$ ps is shown. In order to reduce the pumping power of the laser a $\lambda/2$- plate and a polarizer was placed before the focusing mirror. This allowed the laser power to be continuously adjusted without changing the direction of the beam.

Both peaks show a qualitative similar fluence behaviour. The (1/4 1/4 0) graph is considerably more noisy, due to a weaker diffraction efficiency. For the (1/4 1/4 1/2) as well as for the (1/4 1/4 0) peak a small excitation fluence is sufficient to induce changes

in the system. The induced dynamics level off of at a fluence of 5-6 mJ/cm^2. The similar saturation energy indicates a common origin for changes in the two peaks.

9.3.2 Low-alpha data

In figure 9.4 time-resolved dynamics are shown when the Diamond Light Source operates in the 'low-alpha' mode. This is a mode of operation in which the generated x-rays have a shorter temporal duration at the expense of a reduced x-ray intensity, as explained in 8.2.3.

Here, measurements with a bunch length of 10 ps for the (1/4 1/4 1/2) peak are reported. Due to the combination of the reduced x-ray intensity in the 'low-alpha' mode and a weaker diffraction efficiency, measurements on the (1/4 1/4 0) peak where not possible. The measurements shown in 9.4 a) are averaged over several traces accumulated over the course of 6 hours. The data points are the measured data while the red curve is a fit using an error function with a full width at half maximum (FWHM) determined to be 10 ps. This measurement compares well to the FWHM of the electron bunch as measured with a streak camera inside the storage ring, by the Diamond light source. Energy-resolved scans where taken at a delay of 15 ps, similar to the one shown in figure 9.2. It is clearly visible that on this timescale the photo-induced melting of the diffraction peak has already completely occurred and the remaining signal is only due to fluorescence. An attempt to measure the time-resolved dynamics with 3 ps pulses was also made. For this measurements the flux was reduced by a factor of 50 compared to the 10 ps measurement. The count rate for the diffracted x-rays then had a similar magnitude to the detector noise, making a measurement infeasible.

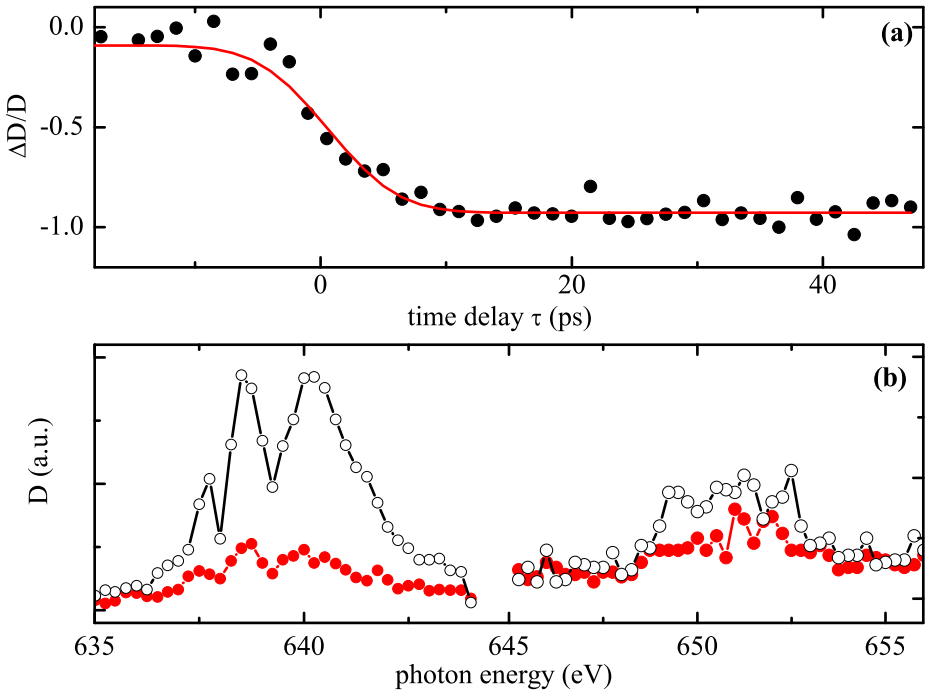

Figure 9.4: Time- and energy-resolved scans performed in the 'low-alpha' mode.

9.4 Nanosecond dynamics

At longer times we observe the relaxation back to the magnetically ordered ground state with at least three timescales, in figure 9.5 the data for pump fluences of 2 mJ/cm^2 and 5.5 mJ/cm^2 are shown for the (1/4 1/4 1/2) peak. A delay of between -300 and 400 ps was introduced by the mechanical delay stage whilst longer delays were introduced electronically, for more details see 8.3.4. In the case of a high fluence two of these timescales could be fitted to exponential decays of $\tau_1 = 10$ and $\tau_2 = 110$ ns, while a much longer timescale, visible as a plateau at about 7 % of the signal loss (in the high fluence data), extends well beyond the window of our measurements. In the low fluence data the decay times are $\tau_1 = 5$ and $\tau_2 = 82$ ns and the plateau is 4 % of the signal at $\tau = 0$ ps. The faster decay time τ_1 is close to the thermal diffusion time in the material $\tau_D = 5$ ns. This time is calculated by using the coefficient of a related compound (La_{1-x} Sr_xMnO_3) [109], D = 0.5 mm^2/s ($\tau_{\text{diff}} \approx L^2/D$, where L = 60 nm is

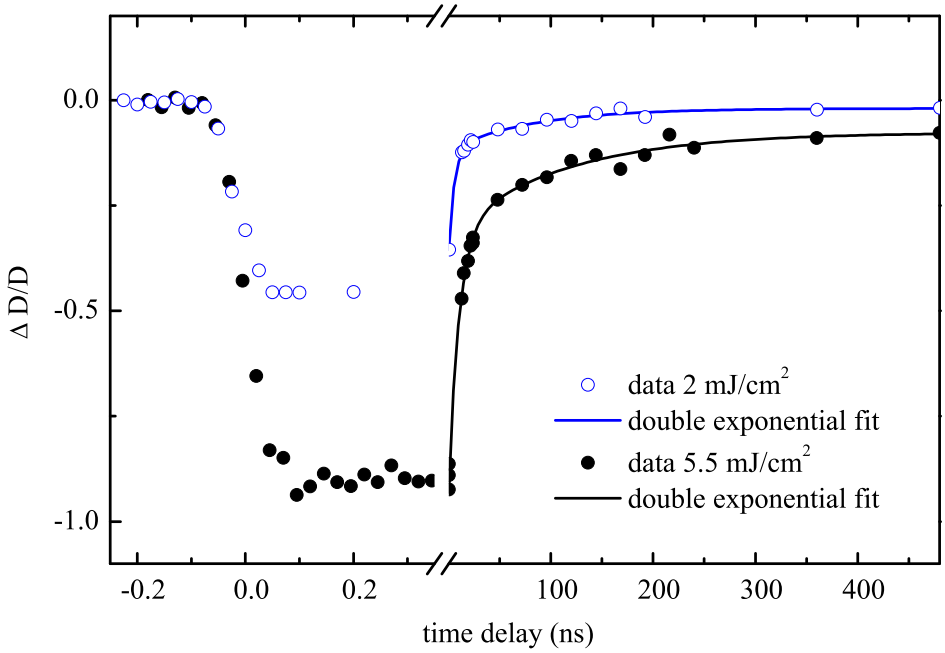

Figure 9.5: The nanosecond dynamics of the magnetic (1/4 1/4 1/2) peak is depicted.

the absorption depth). Differences might arise from the non-equilibrium conditions after photo excitation.

The present data set does not allow a clear interpretation of the fluence dependence of the relaxation dynamics. These are likely driven by a combination of heat diffusion and nucleation of CE antiferromagnetic order. Other experiments are needed to clarify the processes that occur during the relaxation of the transient dynamics. For example, a measurement of the diffraction peak width could reveal how the relaxation takes place, see appendix B. One possibility could be that the photo excitation reduces the scattering strength and leaves the spatial correlation unaffected. It could therefore be expected that the peak intensity decreases, leaving the width constant. If on the other hand the spatial correlation is destroyed then the peak could be expected to narrow during the relaxation process.

Another possible experiment is the measurement of x-ray magnetic circular dichroism (XMCD) or x-ray magnetic linear dichroism (XMLD) signals which could reveal

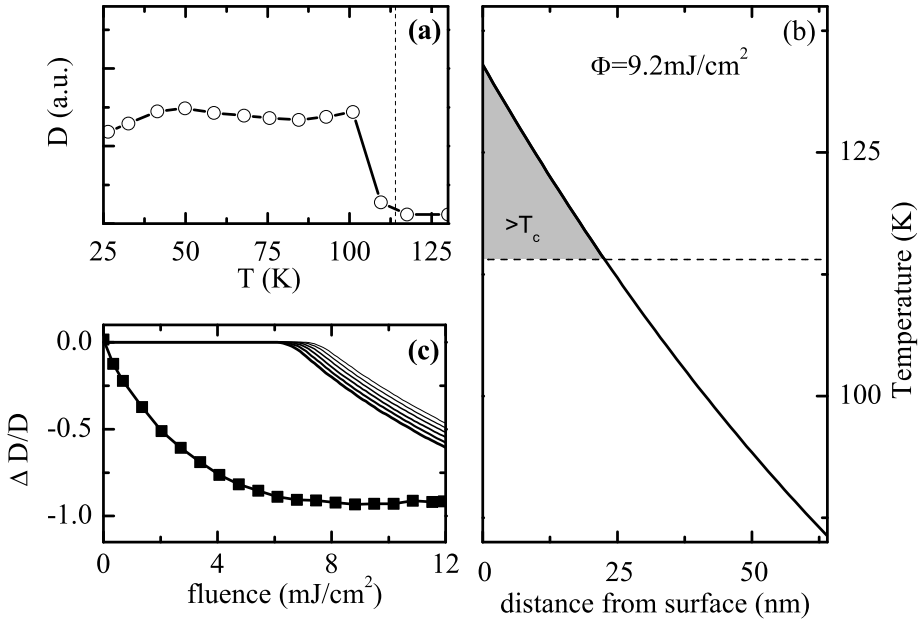

Figure 9.6: (a) Temperature dependent scattering intensity at the (1/4 1/4 1/2) peak recorded at 641.5 eV. (b) Calculated temperature profile for a fluence of Φ= 9.2 mJ/cm^2 over the distance from the surface. (c) The fluence dependent scattering intensity of the (1/4 1/4 1/2) peak (squares), the thin lines are the calculated fraction of the probed volume above T_c for different absorption depth of the pumped light.

the magnetic state during the relaxation process. These measurements would provide further insight into the different relaxation times and their origins.

9.5 Laser heating effects

Before proposing an interpretation to the observations, it is important to consider the effect of heating due to the laser power. If the temperature was raised above T_N = 110 K but remained below $T_{OO/CO}$ = 220 K, magnetic ordering would melt, whilst in-plane orbital order would only be reduced. Analysis of the data excludes this explanation.

First, we can calculate an upper limit for the laser induced heating. As a simple first step we start by assuming that the photo-excited volume (defined by the laser

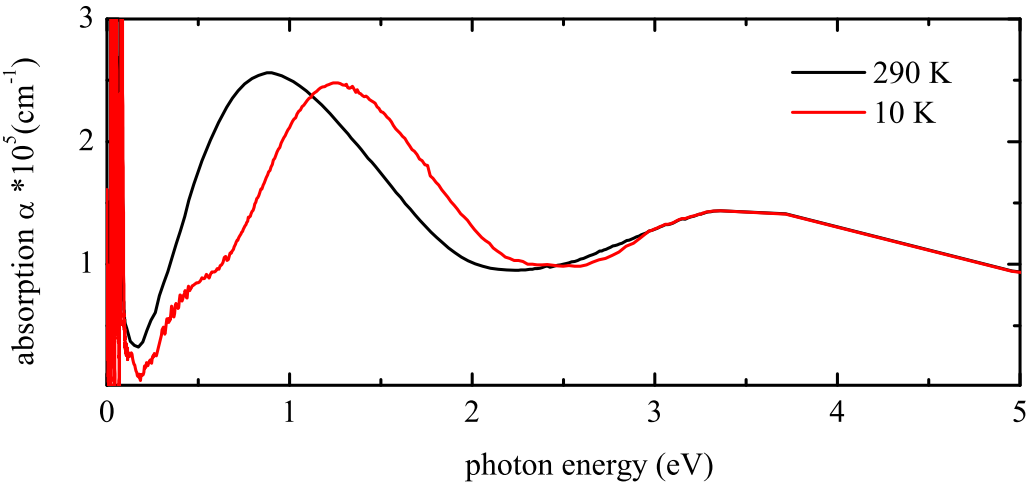

Figure 9.7: Optical absorption spectra in $La_{0.5}Sr_{1.5}MnO_4$ after Kramers-Kronig of reflectivity data from [65]

spot size and the linear absorption depth) is heated once equilibrium between electrons and lattice is reached. For now we assume that laser power is absorbed homogenously, this will be refined later to incorporate the exponentially decaying amplitude into the material. From literature data we extract the optical constants $n = 1.29$, $k = 0.966$ at 1.6 eV using Kramers-Kronig analysis, and find the absorption depth to be d = $\lambda/4\pi$k = 60 nm and 25 % reflectivity at 10 K. At room temperature these values change to d=65 nm, R=16 %. In the absence of diffusion, we calculate that 138 J/cm^3 thermalizes into the solid for each mJ/cm^2 of absorbed laser fluence.

From the temperature dependent specific heat C(T), the increase in temperature (averaged over the absorption depth) is computed for all excitation fluences. A maximum of 50 K for excitation with a pump fluence of 5 mJ/cm^2 is calculated. This temperature increase is most likely overestimated, since carrier and heat diffusion will transport a fraction of the energy into the bulk before thermalisation. In figure 9.6 a) we report on the static changes in diffraction intensity for the (1/4 1/4 1/2) peak at an energy of 641.5 eV. According to this, a temperature jump of 50 K could not explain the strong reduction in diffracted intensity.

This calculation can be extended to include the absorbed intensity profile inside

the material. The exponential absorption means that areas close to the surface are hotter than the average temperature of the probed region. In order to see if this could explain the observed shape for the fluence dependance, the temperature profile over the absorption depth was calculated, shown in figure 9.6 b) for a fluence of 9.2 mJ/cm^2. The dashed line shows the transition temperature, the grey area is indicating the part of the probed volume that is above T_N. In figure 9.6 c) we reproduce the fluence dependent change of the photo-induced signal for the (1/4 1/4 1/2) peak at T = 25 K alongside a plot that shows the fraction of the pumped volume over T_N. Both curves remain significantly different. Already for weak excitation we measure a sizeable photo-induced drop in diffraction intensity, saturating near 5 mJ/cm^2. This is in contrast to the temperature dependance of the peak (when the laser pulses are blocked), which is essentially constant up to T_N = 110 K. This experimental observation is strengthened by the calculation of the volume fraction over T_N for different fluencies. In a pure thermal scenario the deposited energy has to be high enough to heat the system by more then 85 K. It is worth noting that in order to reproduce the shape that we observed experimentally (no threshold) we need to change the critical temperature in the calculation towards a much lower value ($\approx$ 40 K).

Additionally, the presented calculation can be regarded as an upper limit for the heating scenario. As mentioned earlier the electrons will propagate out of the volume due to charge scattering and diffusion processes. This increases the effective volume over which the hot electrons thermalize with the lattice. In figure 9.6 c) this scenario is indicated. The lines that gradually thin out correspond to situations where the electrons diffuse deeper into the bulk. This carrier diffusion moves the observed fluence threshold to higher values.

Figure 9.8 shows the pump induced change of the (1/4 1/4 0) scattering intensity 43 μs after the excitation has taken place at different base temperature. This delay

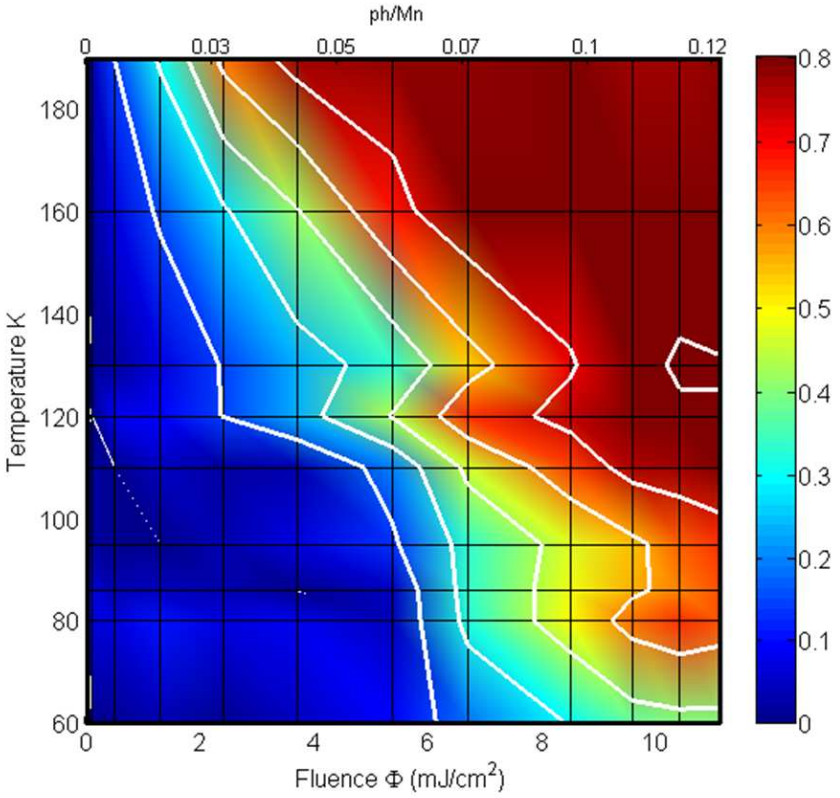

Figure 9.8: The figure shows the relative changes of the (1/4 1/4 0) peak 43 μs after time zero for different fluences and different sample temperatures. In the bottom left blue area the sample has relaxed back to the ground state.

is chosen deliberately, it is directly before the next excitation pulse arrives. For low fluences (the bottom left corner) the pump induced changes have relaxed back to the ground state (blue areas). This contrasts with the situation observed for higher fluences or higher base temperatures, here an average decrease in diffraction intensity is observable and the system does not recover before the next pump pulse arrives.

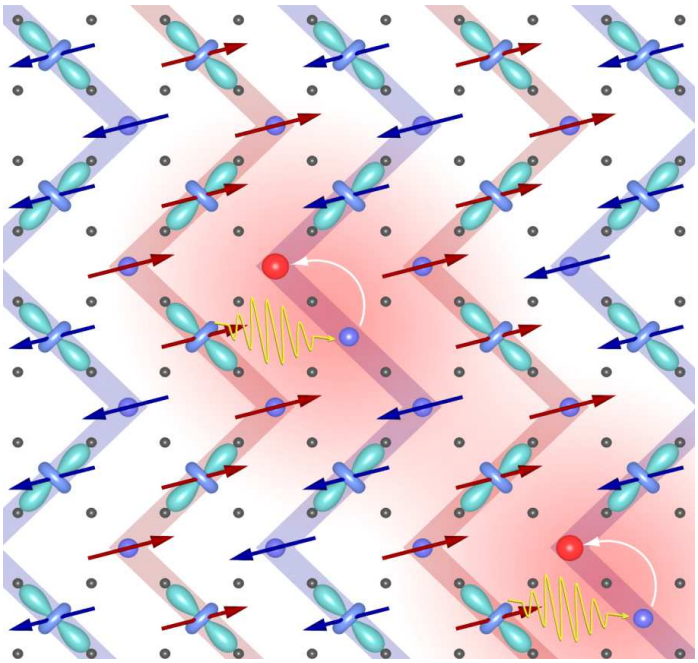

Figure 9.9: Schematic view of the photo-excitation that transfers charge predominantly along the ferromagnetic aligned chains. Thus transforming a $Mn^{4+}/(Mn^{3+}/Mn^{4+})/Mn^{3+}$ chain into a $Mn^{4+}/(Mn^{4+}/Mn^{3+})/Mn^{3+}$

9.6 Interpretation

Charge order in $La_{0.5}Sr_{1.5}MnO_4$ is often described as a checkerboard charge pattern of alternating Mn^{3+} and Mn^{4+} - cations. Complete charge separation is unlikely to have fully occured and this pattern is best understood as a charge density wave of $Mn^{3.5+\delta}$ and $Mn^{3.5-\delta}$ [62]. However, for the purposes of the following discussion the charge separation picture will be used. Due to the strong on-site Hund's coupling, excitation with linearly polarized light at 1.6 eV cannot transfer charge between antiferromagnetically coupled sites, and corresponds only to charge transfer along the $\underline{Mn^{4+}/Mn^{3+}}/Mn^{4+}/Mn^{3+}$ 'zigzag' chains[110], transforming them into - $\underline{Mn^{4+}/Mn^{4+}}/Mn^{3+}/Mn^{3+}$ ones. Photo-excitation can be thought of as injecting sparse charge defects into ferromagnetically coupled chains, perturbing the occupancy of various orbitals (see figure 9.9). Excitation between 0.5 and 10 mJ/cm^2, corresponds to photo doping densities (excitations per manganese site) of less than

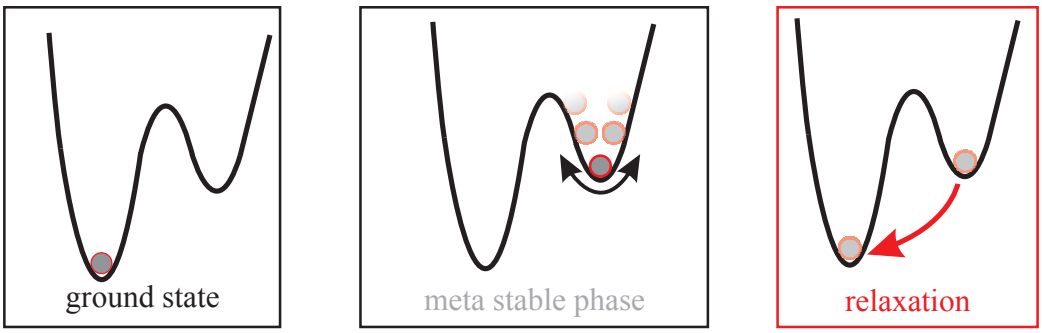

Figure 9.10: The schematic is showing the free energy landscape of the metastable photo excited state for the system in the ground state, its excited state and during the relaxation process.

1 % and 10 %. Charge defects are likely to couple effectively to magnetic order, which is stabilized by a short-range exchange interaction. A qualitative argument can be provided along the following lines. If one applies the Goodenough-Kanamori rules [34] to the new chain $\underline{Mn^{4+}/Mn^{4+}}/Mn^{3+}/Mn^{3+}$ of the photo-excited state [85], one notices that the exchange pattern is drastically altered. Whilst in the ground state all 3+/4+ bonds were ferromagnetic, the newly formed Mn^{4+}-Mn^{4+} bonds, as well as Mn^{3+}-Mn^{3+} should, according to GKA rules, promptly give rise to an AF/FM/AF coupling pattern, $Mn^{4+} \overset{AF}{\leftrightarrow} Mn^{4+} \overset{FM}{\leftrightarrow} Mn^{3+} \overset{AF}{\leftrightarrow} Mn^{3+}$. The coupling along the c axis, previously entirely antiferromagnetic, would also switch sign and become positive if the photo-dopants were sparse. Whilst this picture is clearly oversimplified, it provides a working hypothesis of how photo-excitation can couple directly to the magnetism. The cooperative Jahn-Teller order is more robust. Its dominant interactions are, in fact, long range and may not be affected by sparse photo-dopants. For the low fluences, the mechanism observed here is nonthermal, and the sample temperature never exceeds T_N. Not even in areas close to the surface where the excitation fluence is highest.

Figure 9.10 proposes a schematic view of the physics in play. Photo-excitation melts CE antiferromagnetism, creating an alternative phase that may or may not have residual spin order. This phase is, as observed by comparing different diffraction

peaks, a two-dimensional electronic phase. This state persists for tens of nanoseconds, relaxing back to the ground state with a complex set of processes that combine cooling by diffusion and nucleation of the CE state. This data goes well beyond what was known previously of this photo-induced transition, which could only detect drop in optical birefringence. Resonant soft x-ray diffraction is especially effective in measuring antiferromagnetic and orbital couplings. However, based on the data presented an assessment of whether the product state of the solid is paramagnetic or even ferromagnetic, an interesting possibility that has been raised by recent measurements using ultrafast Magneto-optical Kerr effect in related compounds [111], cannot be made. It is also quite possible that different forms of magnetic order characterize the product state, which may well result in scattering peaks at wavevectors that are not accessible at soft x-ray wavelengths. The question of whether the product phase is magnetically ordered is crucial, and time-resolved x-ray magnetic circular dichroism [112] may provide an answer, detecting any net magnetization that develops. Experiments with femtosecond temporal resolution, now possible at Free Electron Lasers (FEL), can also clarify the non-equilibrium path that underpins this photo-induced dynamics.

9.7 Summary

In summary we report on time-resolved soft x-ray diffraction probe measurements of microscopic spin and orbital ordering dynamics in the photo-induced phase of $La_{0.5}Sr_{1.5}MnO_4$. The picture that emerges shows that optical excitation destroys the three-dimensional magnetic ordering while the in-plane orbital ordering is much less affected. This work breaks new ground in that it allows us to see the dynamics of complex anti-ferromagnetic order in the time domain, and while it clearly leaves questions unanswered, it also points us in a new direction to map all degrees of

freedom of complex solids in the time domain, a new class of experiments that is only starting to become possible with new pulsed laser and x-ray techniques.

Chapter 10

Summary and Outlook

This thesis has investigated the photo-induced dynamics of electronic order (orbital and spin) in the prototypical compound $La_{0.5}Sr_{1.5}MnO_4$. To this end, two different approaches where used:

i) The orbital order was probed on the few femtosecond timescale using optical anisotropy measurements.

ii) The evolution of orbital and spin order after photoexcitation was directly probed with time-resolved resonant soft x-ray diffraction.

Chapter 7 presented the ultrafast optical experiment. Photoinduced changes in the orbital order are probed through the optical anisotropy in the polarization of reflected light at 1.96 eV. Previous measurements had a resolution of 200 fs, in the presented work this was improved to 16 fs, faster then the period of the highest frequency phonon. This measurement revealed a prompt drop in the orbital order that occurs after photoexcitation, only limited by the integral of the cross correlation between pump and probe pulses. This gives rise to the interpretation that depletion of the *d*-orbital is sufficient to melt the orbital order. A lattice contribution cannot be excluded, but it would require that an overdamped vibration drives the system in the unordered phase in less than half a period. One caveat of this interpretation

is that the optical anisotropy measures a macroscopic sample response and hence a direct association with microscopic degrees of freedom is not possible, as it also can be influenced by strain.

Therefore, a dedicated resonant soft x-ray diffractometer was designed and commissioned at the Diamond Light Source, as described in chapter 8. In chapter 9 the first time-resolved resonant soft x-ray diffraction experiment on the model compound $La_{0.5}Sr_{1.5}MnO_4$ was presented. The highest temporal resolution achieved was 10 ps, when the storage ring was operated in the 'low-alpha' mode. This approach is an unambigous measurement of changes in the three-dimensional spin and two-dimensional orbital order, through a measurement of the associated $(1/4\ 1/4\ 1/2)$ or $(1/4\ 1/4\ 0)$ superlattice diffraction peaks. It was found that intense femtosecond light pulses melt the three-dimensional magnetic spin order completely, while the orbital order is affected much less [72, 113].

It was also demonstrated that the relaxation dynamics of the melted diffraction peak back to the ground state can be measured. The timescale of the recovery from the $(1/4\ 1/4\ 1/2)$ peak was found to slow down with increasing excitation fluence; this suggests that spin frustration impedes the relaxation. Further insight could be gained by mapping changes in peak height and width during the recovery as discussed in the appendix B. The next step forward would be to perform x-ray diffraction experiments on the same timescale as the optical anisotropy measurements. It seems possible to address photo-induced changes to their microscopic origin. Also, it could be possible to directly measure orbitons [5, 114] through oscillations of the associated orbital diffraction peak. The generation of soft x-ray radiation with duration in the femtosecond range is already possible. In storage rings the slicing technique is used to generate x-ray pulses in the hundred femtosecond range [103]. The available photon flux in combination with the weak efficiency of the diffraction signal allows only measurements in special cases [105]. A more promising approach is to use x-

rays generated from free electron lasers like the LCLS at SLAC (USA) or FLASH at Desy (Germany)[115]. To date their most severe problem is the jitter between pump and probe pulse. Different techniques can be used to measure the jitter down to the hundred femtosecond range [116] and might reach the few femtosecond range soon [117].

Recently it has been shown that a phase transition can be induced by using mid-infrared or Terahertz radiation that directly couples to the lattice degree of freedom. It was shown that radiation resonant to a phonon can drive a phase transition [13, 14]. This leads directly to the ideal pump-probe experiment: excitation of a lattice vibration using mid-infrared radiation and probing the response of the spin and the orbital order in the material $La_{0.5}Sr_{1.5}MnO_4$ with soft x-ray diffraction.

A vast field of very interesting experiments seems possible in the near future. The rising number of suitable pump and probe sources promise and will enable many exciting experiments. Thus allowing resarchers to answer long-standing questions as well as generating many new ones.

Appendices

Appendix A

Energy-resolved scan of the diffraction peak

When the incoming photon energy is tuned over the absorption edge the wavelength changes. This changes the size of the Ewald sphere, when the variations are not to strong this can be compensated by rotating the sphere. Experimentally this means that each photon energy has its unique scattering angle (θ(E)) according to the Bragg equation. Using the unit cell dimension $a = b$ =3.876 Å, $c = 12.44$ Å [53] the d-spacing can be calculated according to equation 4.6. Together with the Bragg equation 4.5 this gives:

$$\theta_{\frac{1}{4}\ \frac{1}{4}\ 0} = \text{asin}\left(\frac{565.96}{E(\text{eV})}\right) \tag{A.1}$$

$$\theta_{\frac{1}{4}\ \frac{1}{4}\ \frac{1}{2}} = \text{asin}\left(\frac{618.31}{E(\text{eV})}\right) \tag{A.2}$$

Figure A.1 shows the diffraction angle over the photon energy for the (1/4 1/4 0) and the (1/4 1/4 1/2) peak.

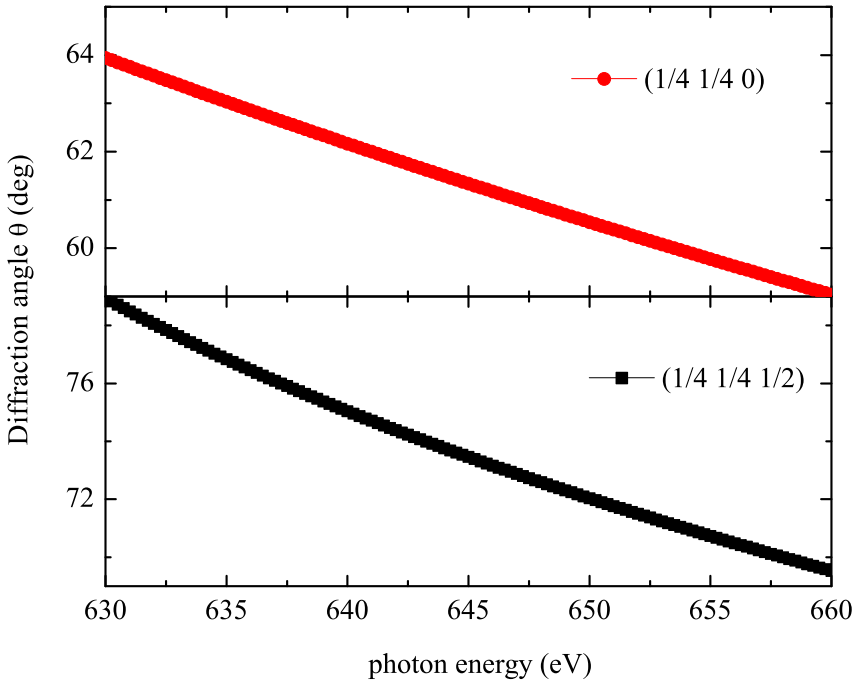

Figure A.1: Diffraction angle over the photon energy.

Appendix B

Angle resolution

A paper by Thomas and co-workers [118] illustrates nicely what can be learned by analysing the width of the diffraction peak. It was shown that the correlation length of the magnetic peak is twice as large as the orbital correlation length, for all temperatures. This implies that the original theory from Goodenough that requires a direct connection between magnetic and orbital degree of freedom is more complicated. For the experiments presented here a measurement of the correlation length could lead to an understanding how the melted order is re-established after laser excitation. The k-space resolution of the diffractometer is limited by the angle resolution. As stated above, the width of the peak in k-space is directly related to the correlation length of the corresponding ordering ($\xi_l = \frac{1}{\Delta k}$). A narrow diffraction peak therefore implies a long correlation length. Hence the coherently interacting scattering sites cover a wider area compared to a broad peak. Even in a single crystal the correlation length does not extend over the whole crystal but is normally much less.

The resolution in k-space, or the angular resolution, is limited by the size of the detector and its distance from the centre of rotation. In figure B.1 the scattering geometry is shown. In PCMO the correlation length for the orbital degree of freedom is 37 nm (0.03nm^{-1})[118]. To sample this peak with a twentieth of its width it is

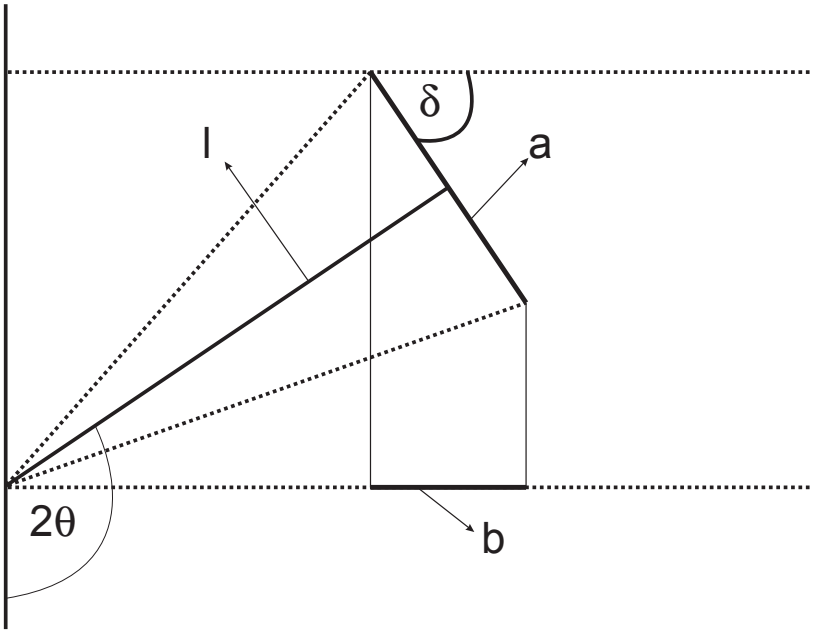

Figure B.1: Shows a schematic to calculate the angle resolution of the chamber, the size of the detector is given by a, the distance between the detector and the interaction region is given by l, and the diffraction angle by 2θ.

necessary to have an angle resolution of 0.05 deg. This follows from Bragg's equation

$$\mathrm{d} \cdot \sin\theta = \frac{\lambda}{2} = \frac{\pi}{k} \tag{B.1}$$

expressing the width of the diffraction peak using the Bragg equation yields

$$\xi_l = \frac{1}{\Delta k} = \frac{d}{\pi}\left[\frac{1}{\sin\theta_1} - \frac{1}{\sin\theta_2}\right]^{-1}$$
$$\text{with } \theta_{1/2} = \theta_B \mp \Delta\theta$$

here θ_B is the position of the Bragg peak and $\Delta\theta$ its width. The angular resolution in our experiment is limited by the size of the detector (a) and its distance away from the interaction region (l), see figure B.1. A straight forward geometric consideration is revealing that the active area from our detector has to be smaller than 200μm. In the presented experiment the MCP detector has an area of 8 mm. When a slit is inserted in front of the detector the amount of scattered photons will get smaller thus

increasing the integration time.

$$a = \frac{b}{cos\delta}$$
$$\delta = 180 - 2\theta$$
$$b = l \cdot [\cos(2\theta - \pi/2 - \Delta\alpha) - \cos(2\theta - \pi/2 + \Delta\alpha)]$$

The angle $\Delta\alpha$ is the resolution which is used to sample the peak. For the experiments presented here the width of the diffraction peak was limited by the resolution of the instrument. Future amendments can easily be made to make these types of measurements possible.

Bibliography

[1] A. Sommerfeld and H.Bethe, *Elektronentheorie der Metalle*. Springer Verlag, Heidelberg, 1933.

[2] R. J. Birgeneau and M. A. Kastner, "Frontier Physics with Correlated Electrons," *Science*, vol. 288, no. 5465, p. 437, 2000.

[3] J. G. Bednorz and K. A. Mller, "Possible high T_c superconductivity in the Ba-La-Cu-O system," *Z. Phys. B*, vol. 64, no. 2, pp. 189–193, 1986.

[4] S. Jin, T. H. Tiefel, M. McCormack, R. A. Fastnacht, R. Ramesh, and L. H. Chen, "Thousandfold Change in Resistivity in Magnetoresistive La-Ca-Mn-O Films," *Science*, vol. 264, no. 5157, pp. 413–415, 1994.

[5] Y. Tokura and N. Nagaosa, "Orbital physics in transition-metal oxides," *Science*, vol. 288, no. 5465, pp. 462–468, 2000.

[6] R. von Helmolt, J. Wecker, B. Holzapfel, L. Schultz, and K. Samwer, "Giant negative magnetoresistance in perovskitelike $La_{2/3}Ba_{1/3}MnO_x$ ferromagnetic films," *Phys. Rev. Lett.*, vol. 71, pp. 2331–2333, Oct 1993.

[7] H. Takagi and H. Y. Hwang, "An Emergent Change of Phase for Electronics," *Science*, vol. 327, no. 5973, pp. 1601–1602, 2010.

[8] S. Koshihara, Y. Tokura, T. Mitani, G. Saito, and T. Koda, "Photoinduced valence instability in the organic molecular compound tetrathiafulvalene-p-chloranil (ttf-ca)," *Phys. Rev. B*, vol. 42, pp. 6853–6856, Oct 1990.

[9] M. Fiebig, K. Miyano, Y. Tomioka, and Y. Tokura, "Visualization of the Local Insulator-Metal Transition in $Pr_{0.7}Ca_{0.3}MnO_3$," *Science*, vol. 280, no. 5371, pp. 1925–1928, 1998.

[10] M. Fiebig, K. Miyano, T. Satoh, Y. Tomioka, and Y. Tokura, "Action spectra of the two-stage photoinduced insulator-metal transition in $Pr_{0.7}Ca_{0.3}MnO_3$," *Phys. Rev. B*, vol. 60, pp. 7944–7949, Sep 1999.

[11] D. S. Chemla and J. Shah, "Many-body and correlation effects in semiconductors," *Nature*, vol. 411, pp. 549–557, May 2001.

[12] F. Krausz and M. Ivanov, "Attosecond physics," *Rev. Mod. Phys.*, vol. 81, pp. 163–234, Feb 2009.

[13] M. Rini, R. Tobey, N. Dean, J. Itatani, Y. Tomioka, Y. Tokura, R. W. Schoenlein, and A. Cavalleri, "Control of the electronic phase of a manganite by mode-selective vibrational excitation," *Nature*, vol. 449, pp. 72–74, Sept. 2007.

[14] R. I. Tobey, D. Prabhakaran, A. T. Boothroyd, and A. Cavalleri, "Ultrafast electronic phase transition in $La_{0.5}Sr_{1.5}MnO_4$ by coherent vibrational excitation: Evidence for nonthermal melting of orbital order," *Phys. Rev. Lett.*, vol. 101, p. 197404, Nov 2008.

[15] A. Cavalleri, C. Tóth, C. W. Siders, J. A. Squier, F. Ráksi, P. Forget, and J. C. Kieffer, "Femtosecond structural dynamics in VO_2 during an ultrafast solid-solid phase transition," *Phys. Rev. Lett.*, vol. 87, p. 237401, Nov 2001.

[16] E. Collet, M.-H. Lemee-Cailleau, M. Buron-Le Cointe, H. Cailleau, M. Wulff, T. Luty, S.-Y. Koshihara, M. Meyer, L. Toupet, P. Rabiller, and S. Techert, "Laser-Induced Ferroelectric Structural Order in an Organic Charge-Transfer Crystal," *Science*, vol. 300, no. 5619, pp. 612–615, 2003.

[17] L. Perfetti, P. A. Loukakos, M. Lisowski, U. Bovensiepen, H. Berger, S. Biermann, P. S. Cornaglia, A. Georges, and M. Wolf, "Time evolution of the electronic structure of $1T - TaS_2$ through the insulator-metal transition," *Phys. Rev. Lett.*, vol. 97, p. 067402, Aug 2006.

[18] J. H. de Boer and E. J. W. Verwey, "Semi-conductors with partially and with completely filled 3 d -lattice bands," *Proceedings of the Physical Society*, vol. 49, no. 4S, p. 59, 1937.

[19] E. Wigner, "On the interaction of electrons in metals," *Phys. Rev.*, vol. 46, pp. 1002–1011, Dec 1934.

[20] N. F. Mott, "The basis of the electron theory of metals, with special reference to the transition metals," *Proceedings of the Physical Society. Section A*, vol. 62, no. 7, p. 416, 1949.

[21] J. Hubbard, "The Description of Collective Motions in Terms of Many-Body Perturbation Theory," *Proceedings of the Royal Society of London. Series A. Mathematical and Physical Sciences*, vol. 240, no. 1223, pp. 539–560, 1957.

[22] M. Imada, A. Fujimori, and Y. Tokura, "Metal-insulator transitions," *Rev. Mod. Phys.*, vol. 70, pp. 1039–1263, Oct 1998.

[23] E. Dagotto, "Complexity in Strongly Correlated Electronic Systems," *Science*, vol. 309, no. 5732, pp. 257–262, 2005.

[24] Y. Tomioka, A. Asamitsu, H. Kuwahara, Y. Moritomo, and Y. Tokura, "Magnetic-field-induced metal-insulator phenomena in $Pr_{1-x}Ca_xMnO_3$ with controlled charge-ordering instability," *Phys. Rev. B*, vol. 53, pp. R1689–R1692, Jan 1996.

[25] Y. Tokura and Y. Tomioka, "Colossal magnetoresistive manganites," *Journal of Magnetism and Magnetic Materials*, vol. 200, no. 1-3, pp. 1 – 23, 1999.

[26] S. N. Ruddlesden and P. Popper, "New compounds of the K_2NiF_4 type," *Acta Crystallographic*, vol. 10, p. 538, 1957.

[27] Y. Moritomo, A. Asamitsu, H. Kuwahara, and Y. Tokura, "Giant magnetoresistance of manganese oxides with a layered perovskite structure," *Nature*, vol. 380, pp. 141–144, Mar. 1996.

[28] Y. Tokura, *Fundamental Features of Colossal Magnetoresisitive Manganese Oxides, in Colossal Magnetoresistance Oxides*. Gordon & Breach Monographs in Condensed Matter Science, London, 1999.

[29] K. Yoshida, *Theory of Magnetism*. Springer, Berlin, Heidelberg, NewYork, 1998.

[30] D. Dessau and Z. Shen, *Collosal Magnetoresistance Oxides*. Gordon & Breach Monographs in Condensed Matter Science, London, 2000.

[31] A. J. Millis, B. I. Shraiman, and R. Mueller, "Dynamic jahn-teller effect and colossal magnetoresistance in $La_{1-x}Sr_{1+x}MnO_3$," *Phys. Rev. Lett.*, vol. 77, pp. 175–178, Jul 1996.

[32] Y. Okimoto, T. Katsufuji, T. Ishikawa, A. Urushibara, T. Arima, and Y. Tokura, "Anomalous variation of optical spectra with spin polarization in double-exchange ferromagnet: $La_{1-x}Sr_xMnO_3$," *Phys. Rev. Lett.*, vol. 75, pp. 109–112, Jul 1995.

[33] M. Quijada, J. Černe, J. R. Simpson, H. D. Drew, K. H. Ahn, A. J. Millis, R. Shreekala, R. Ramesh, M. Rajeswari, and T. Venkatesan, "Optical conductivity of manganites: Crossover from jahn-teller small polaron to coherent transport in the ferromagnetic state," *Phys. Rev. B*, vol. 58, pp. 16093–16102, Dec 1998.

[34] J. B. Goodenough, "Theory of the role of covalence in the perovskite-type manganites [La, M(II)]MnO_3," *Phys. Rev.*, vol. 100, pp. 564–573, Oct 1955.

[35] E. Dagotto, *Nanoscale Phase Separation and Colosssal Magnetoresistance*. Springer, 2003.

[36] P. W. Anderson and H. Hasegawa, "Considerations on double exchange," *Phys. Rev.*, vol. 100, pp. 675–681, Oct 1955.

[37] D. I. Khomskii and G. A. Sawatzky, "Interplay between spin, charge and orbital degrees of freedom in magnetic oxides," *Solid State Communications*, vol. 102, no. 2-3, pp. 87 – 99, 1997. Highlights in Condensed Matter Physics and Materials Science.

[38] J. van den Brink, G. Khaliullin, and D. Khomskii, "Charge and orbital order in half-doped manganites," *Phys. Rev. Lett.*, vol. 83, pp. 5118–5121, Dec 1999.

[39] V. I. Anisimov, F. Aryasetiawan, and A. I. Lichtenstein, "First-principles calculations of the electronic structure and spectra of strongly correlated systems: the LDA + U method," *Journal of Physics: Condensed Matter*, vol. 9, no. 4, p. 767, 1997.

[40] A. I. Liechtenstein, V. I. Anisimov, and J. Zaanen, "Density-functional theory and strong interactions: Orbital ordering in mott-hubbard insulators," *Phys. Rev. B*, vol. 52, pp. R5467–R5470, Aug 1995.

[41] L. F. Feiner and A. M. Oleś, "Electronic origin of magnetic and orbital ordering in insulating $LaSrMnO_3$," *Phys. Rev. B*, vol. 59, pp. 3295–3298, Feb 1999.

[42] Y. Murakami, H. Kawada, H. Kawata, M. Tanaka, T. Arima, Y. Moritomo, and Y. Tokura, "Direct observation of charge and orbital ordering in $La_{0.5}Sr_{1.5}MnO_4$," *Phys. Rev. Lett.*, vol. 80, pp. 1932–1935, Mar 1998.

[43] S. B. Wilkins, P. D. Spencer, P. D. Hatton, S. P. Collins, M. D. Roper, D. Prabhakaran, and A. T. Boothroyd, "Direct observation of orbital ordering in $La_{0.5}Sr_{1.5}MnO_4$ using soft x-ray diffraction," *Phys. Rev. Lett.*, vol. 91, p. 167205, Oct 2003.

[44] S. S. Dhesi, A. Mirone, C. De Nadaï, P. Ohresser, P. Bencok, N. B. Brookes, P. Reutler, A. Revcolevschi, A. Tagliaferri, O. Toulemonde, and G. van der Laan, "Unraveling orbital ordering in $La_{0.5}Sr_{1.5}MnO_4$," *Phys. Rev. Lett.*, vol. 92, p. 056403, Feb 2004.

[45] M. von Laue, "Nobelprize.org.," July 1914.

[46] W. Demtröder, *Experimentalphysik 3: Atome, Moleküle und Festkörper (Springer-Lehrbuch) (German Edition)*. Springer, 2010.

[47] D. Attwood, *Soft X-Rays and Extreme Ultraviolet Radiation: Principles and Applications*. Cambridge University Press, 2007.

[48] M. Blume, "Magnetic scattering of x rays (invited)," *J. of Appl. Phys.*, vol. 57, no. 8, pp. 3615–3618, 1985.

[49] M. Blume and D. Gibbs, "Polarization dependence of magnetic x-ray scattering," *Phys. Rev. B*, vol. 37, pp. 1779–1789, Feb 1988.

[50] S. Larochelle, A. Mehta, L. Lu, P. K. Mang, O. P. Vajk, N. Kaneko, J. W. Lynn, L. Zhou, and M. Greven, "Structural and magnetic properties of the single-layer manganese oxide $La_{0.5}Sr_{1.5}MnO_4$," *Phys. Rev. B*, vol. 71, p. 024435, Jan 2005.

[51] B. J. Sternlieb, J. P. Hill, U. C. Wildgruber, G. M. Luke, B. Nachumi, Y. Moritomo, and Y. Tokura, "Charge and magnetic order in $La_{0.5}Sr_{1.5}MnO_4$," *Phys. Rev. Lett.*, vol. 76, pp. 2169–2172, Mar 1996.

[52] D. Senff, F. Krüger, S. Scheidl, M. Benomar, Y. Sidis, F. Demmel, and M. Braden, "Spin-wave dispersion in orbitally ordered $La_{0.5}Sr_{1.5}MnO_4$," *Phys. Rev. Lett.*, vol. 96, p. 257201, Jun 2006.

[53] U. Staub, V. Scagnoli, A. M. Mulders, K. Katsumata, Z. Honda, H. Grimmer, M. Horisberger, and J. M. Tonnerre, "Orbital and magnetic ordering in $La_{0.5}Sr_{1.5}MnO_4$ studied by soft x-ray resonant scattering," *Phys. Rev. B*, vol. 71, p. 214421, Jun 2005.

[54] T. Ogasawara, T. Kimura, T. Ishikawa, M. Kuwata-Gonokami, and Y. Tokura, "Dynamics of photoinduced melting of charge/orbital order in a layered manganite $La_{0.5}Sr_{1.5}MnO_4$," *Phys. Rev. B*, vol. 63, p. 113105, Mar 2001.

[55] A. Urushibara, Y. Moritomo, T. Arima, A. Asamitsu, G. Kido, and Y. Tokura, "Insulator-metal transition and giant magnetoresistance in $La_{1-x}Sr_{1+x}MnO_3$," *Phys. Rev. B*, vol. 51, pp. 14103–14109, May 1995.

[56] E. O. Wollan and W. C. Koehler, "Neutron diffraction study of the magnetic properties of the series of perovskite-type compounds $[(1-x)\mathrm{La}, x\mathrm{Ca}]MnO_3$," *Phys. Rev.*, vol. 100, pp. 545–563, Oct 1955.

[57] D. Senff, O. Schumann, M. Benomar, M. Kriener, T. Lorenz, Y. Sidis, K. Habicht, P. Link, and M. Braden, "Melting of magnetic correlations in

charge-orbital ordered $La_{0.5}Sr_{1.5}MnO_4$: Competition of ferromagnetic and antiferromagnetic states," *Phys. Rev. B*, vol. 77, p. 184413, May 2008.

[58] Z. Jirák, S. Krupicka, Z. Simsa, M. Dlouh, and S. Vratislav, "Neutron diffraction study of $Pr_{1-x}Ca_xMnO_3$ perovskites," *Journal of Magnetism and Magnetic Materials*, vol. 53, no. 1-2, pp. 153–166, 1985.

[59] P. G. Radaelli, D. E. Cox, M. Marezio, and S.-W. Cheong, "Charge, orbital, and magnetic ordering in $La_{0.5}Ca_{0.5}MnO_3$," *Phys. Rev. B*, vol. 55, pp. 3015–3023, Feb 1997.

[60] J. Rodrguez-Carvajal, A. Daoud-Aladine, L. Pinsard-Gaudart, M. T. Fernndez-Daz, and A. Revcolevschi, "A new interpretation of the co state in half-doped manganites: new results from neutron diffraction and synchrotron radiation experiments," *Physica B: Condensed Matter*, vol. 320, no. 1-4, pp. 1 – 6, 2002.

[61] C. Ma, H. X. Yang, L. J. Zeng, Z. A. Li, Y. Zhang, Y. B. Qin, and J. Q. Li, "Effects of layered structural features on charge/orbital ordering in $(La, Sr)_{n+1}Mn_nO_{3n+1}$ (n = 1 and 2)," *Journal of Physics: Condensed Matter*, vol. 21, no. 4, p. 045601, 2009.

[62] A. Daoud-Aladine, J. Rodríguez-Carvajal, L. Pinsard-Gaudart, M. T. Fernández-Díaz, and A. Revcolevschi, "Zener polaron ordering in half-doped manganites," *Phys. Rev. Lett.*, vol. 89, p. 097205, Aug 2002.

[63] D. V. Efremov, J. van den Brink, and D. I. Khomskii, "Bond- versus site-centred ordering and possible ferroelectricity in manganites," *Nature Mater.*, vol. 3, pp. 853–856, Dec. 2004.

[64] S. Grenier, J. P. Hill, D. Gibbs, K. J. Thomas, M. v. Zimmermann, C. S. Nelson, V. Kiryukhin, Y. Tokura, Y. Tomioka, D. Casa, T. Gog, and

C. Venkataraman, "Resonant x-ray diffraction of the magnetoresistant perovskite $Pr_{0.6}Ca_{0.4}MnO_3$," *Phys. Rev. B*, vol. 69, p. 134419, Apr 2004.

[65] T. Ishikawa, K. Ookura, and Y. Tokura, "Optical response to orbital and charge ordering in a layered manganite: $La_{0.5}Sr_{1.5}MnO_4$," *Phys. Rev. B*, vol. 59, pp. 8367–8370, Apr 1999.

[66] T. A. Y. Moritomo and Y. Tokura, "Electronic structure of layered perovskite $LaSrMO_4$ (M=Cr, Mn, Fe and Co)," *Journal of the Physical Society of Japan*, vol. 64, no. 11, pp. 4117–4120, 1995.

[67] P. Reutler, O. Friedt, B. Bchner, M. Braden, and A. Revcolevschi, "Growth of $La_{1-x}Sr_{1+x}MnO_4$ single crystals and characterization by scattering techniques," *Journal of Crystal Growth*, vol. 249, no. 1-2, pp. 222 – 229, 2003.

[68] D. Prabhakaran and A. Boothroyd, "Single-crystal growth of $la_{2-2x}sr_{1+2x}mn_2o_7$," *Journal of Materials Science: Materials in electronics*, vol. 14, pp. 587–589, 2003.

[69] S. B. Wilkins, N. Stojić, T. A. W. Beale, N. Binggeli, C. W. M. Castleton, P. Bencok, D. Prabhakaran, A. T. Boothroyd, P. D. Hatton, and M. Altarelli, "Resonant soft x-ray scattering investigation of orbital and magnetic ordering in $La_{0.5}Sr_{1.5}MnO_4$," *Phys. Rev. B*, vol. 71, p. 245102, Jun 2005.

[70] U. Staub, V. Scagnoli, A. M. Mulders, M. Janousch, Z. Honda, and J. M. Tonnerre, "Charge/orbital ordering vs. jahn-teller distortion in $La_{0.5}Sr_{1.5}MnO_4$," *EPL (Europhysics Letters)*, vol. 76, no. 5, p. 926, 2006.

[71] C. W. M. Castleton and M. Altarelli, "Orbital ordering in the manganites: Resonant x-ray scattering predictions at the manganese L_2 and L_3 edges," *Phys. Rev. B*, vol. 62, pp. 1033–1038, Jul 2000.

[72] A. Mirone, S. Dhesi, and G. van der Laan, "Spectroscopy of $La_{0.5}Sr_{1.5}MnO_4$ orbital ordering: a cluster many-body calculation," *The European Physical Journal B*, vol. 53, p. 23, 2006.

[73] E. Muybridge, *Animals in Motion*. Dover Publications, 1957.

[74] H. E. Edgerton and J. R. Killian, *Moments of Vision: The Stroboscopic Revolution in Photography*. MIT Press, 1984.

[75] M. Eigen, R. Norrish, and G. Porter, "The nobel prize in chemistry 1967," July 1967.

[76] C. V. Shank, R. Yen, and C. Hirlimann, "Time-resolved reflectivity measurements of femtosecond-optical-pulse-induced phase transitions in silicon," *Phys. Rev. Lett.*, vol. 50, pp. 454–457, Feb 1983.

[77] A. Zewail, "The nobel prize in chemistry 1999," July 1999.

[78] N. Anscombe, "Europe leads the way in attosecond research," November 2008.

[79] R. Kusters, J. Singleton, D. Keen, R. McGreevy, and W. Hayes, "Magnetoresistance measurements on the magnetic semiconductor $Nd_{0.5}Pb_{1.5}MnO_3$," *Physica B: Condensed Matter*, vol. 155, no. 1-3, pp. 362–365, 1989.

[80] H. Y. Hwang, S.-W. Cheong, P. G. Radaelli, M. Marezio, and B. Batlogg, "Lattice effects on the magnetoresistance in doped $LaMnO_3$," *Phys. Rev. Lett.*, vol. 75, pp. 914–917, Jul 1995.

[81] A. Asamitsu, Y. Moritomo, Y. Tomioka, T. Arima, and Y. Tokura, "A structural phase transition induced by an external magnetic field," *Nature*, vol. 373, pp. 407–409, Feb 1995.

[82] V. Kiryukhin, D. Casa, J. P. Hill, B. Keimer, A. Vigliante, Y. Tomioka, and Y. Tokura, "An x-ray-induced insulator-metal transition in a magnetoresistive manganite," *Nature*, vol. 386, pp. 813–815, Apr. 1997.

[83] M. Rini, Y. Zhu, S. Wall, R. I. Tobey, H. Ehrke, T. Garl, J. W. Freeland, Y. Tomioka, Y. Tokura, A. Cavalleri, and R. W. Schoenlein, "Transient electronic structure of the photoinduced phase of $Pr_{0.7}Ca_{0.3}MnO_3$ probed with soft x-ray pulses," *Phys. Rev. B*, vol. 80, p. 155113, Oct 2009.

[84] K. Miyano, T. Tanaka, Y. Tomioka, and Y. Tokura, "Photoinduced insulator-to-metal transition in a perovskite manganite," *Phys. Rev. Lett.*, vol. 78, pp. 4257–4260, Jun 1997.

[85] S. Wall, D. Prabhakaran, A. T. Boothroyd, and A. Cavalleri, "Ultrafast coupling between light, coherent lattice vibrations, and the magnetic structure of semicovalent $LaMnO_3$," *Phys. Rev. Lett.*, vol. 103, p. 097402, Aug 2009.

[86] T. Ogasawara, M. Matsubara, Y. Tomioka, M. Kuwata-Gonokami, H. Okamoto, and Y. Tokura, "Photoinduced spin dynamics in $La_{0.6}Sr_{0.4}MnO_3$ observed by time-resolved magneto-optical kerr spectroscopy," *Phys. Rev. B*, vol. 68, p. 180407, Nov 2003.

[87] B. Koopmans, M. van Kampen, J. T. Kohlhepp, and W. J. M. de Jonge, "Ultrafast magneto-optics in nickel: Magnetism or optics?," *Phys. Rev. Lett.*, vol. 85, pp. 844–847, 2000.

[88] Y. Shen, *The Principles of Nonlinear Optics*. Wiley, New York, 1984.

[89] K. Bennemann, ed., *Nonlinear Optics in Metals*. Clarendon, Oxford, 1998.

[90] M. Fiebig, D. Fröhlich, B. B. Krichevtsov, and R. V. Pisarev, "Second harmonic generation and magnetic-dipole-electric-dipole interference in antiferromagnetic cr_2o_3," *Phys. Rev. Lett.*, vol. 73, p. 2127, 1994.

[91] P. Beaud, S. L. Johnson, E. Vorobeva, U. Staub, R. A. D. Souza, C. J. Milne, Q. X. Jia, and G. Ingold, "Ultrafast structural phase transition driven by photoinduced melting of charge and orbital order," *Phys. Rev. Lett.*, vol. 103, p. 155702, Oct 2009.

[92] J. H. Jung, K. H. Kim, T. W. Noh, E. J. Choi, and J. Yu, "Midgap states of $La_{1-x}Ca_xMnO_3$ doping-dependent optical-conductivity studies," *Phys. Rev. B*, vol. 57, pp. R11043–R11046, May 1998.

[93] S. Larochelle, A. Mehta, N. Kaneko, P. K. Mang, A. F. Panchula, L. Zhou, J. Arthur, and M. Greven, "Nature of e_g electron order in $La_{1-x}Sr_{1+x}MnO_4$," *Phys. Rev. Lett.*, vol. 87, p. 095502, Aug 2001.

[94] A. Cavalleri, T. Dekorsy, H. H. W. Chong, J. C. Kieffer, and R. W. Schoenlein, "Evidence for a structurally-driven insulator-to-metal transition in VO_2 : A view from the ultrafast timescale," *Phys. Rev. B*, vol. 70, p. 161102, Oct 2004.

[95] K. Yamamoto, T. Kimura, T. Ishikawa, T. Katsufuji, and Y. Tokura, "Raman spectroscopy of the charge-orbital ordering in layered manganites," *Phys. Rev. B*, vol. 61, pp. 14706–14715, Jun 2000.

[96] G. Cerullo, M. Nisoli, and S. D. Silvestri, "Generation of 11 fs pulses tunable across the visible by optical parametric amplification," *Appl. Phys. Lett.*, vol. 71, no. 25, pp. 3616–3618, 1997.

[97] C. Kübler, H. Ehrke, R. Huber, R. Lopez, A. Halabica, R. F. Haglund, and A. Leitenstorfer, "Coherent structural dynamics and electronic correlations dur-

ing an ultrafast insulator-to-metal phase transition in VO_2," *Phys. Rev. Lett.*, vol. 99, p. 116401, Sep 2007.

[98] http://www.diamond.ac.uk/.

[99] M. P. Cox, B. Boussier, S. Bryan, B. F. Macdonald, and H. S. Shiers, "Commissioning of the diamond light source storage ring vacuum system," *Journal of Physics: Conference Series*, vol. 100, no. 9, p. 092011, 2008.

[100] L. Emery, ed., *Recent Operational Data on Continuous Top-Up Operation at the Advanced Photon Source*, Proceedings of the 2001 Particle Accelerator Conference, 2001. p. 2599.

[101] A. A. Zholents and M. S. Zolotorev, "Femtosecond x-ray pulses of synchrotron radiation," *Phys. Rev. Lett.*, vol. 76, pp. 912–915, Feb 1996.

[102] J. Feikes, K. Holldack, P. Kuske, and G. Wuestefeld, "Sub-picosecond electron bunches in the bessy storage ring," *Proceedings of EPAC 2004, Lucerne, Switzerland*, 2004.

[103] R. W. Schoenlein, S. Chattopadhyay, H. H. Chong, T. E. Glover, P. A. Heimann, C. V. Shank, A. A. Zholents, and M. S. Zolotorev, "Generation of Femtosecond Pulses of Synchrotron Radiation," *Science*, vol. 287, no. 5461, pp. 2237–2240, 2000.

[104] S. Khan and et. al., "Layout of a femto-second x-ray source at bessy 2," *PAC03, Portland (USA)*, p. 836, 2003.

[105] K. Holldack, N. Pontius, E. Schierle, T. Kachel, V. Soltwisch, R. Mitzner, T. Quast, G. Springholz, and E. Weschke, "Ultrafast dynamics of antiferromagnetic order studied by femtosecond resonant soft x-ray diffraction," *Appl. Phys. Lett.*, vol. 97, no. 6, p. 062502, 2010.

[106] D. Robin, E. Forest, C. Pellegrini, and A. Amiry, "Quasi-isochronous storage rings," *Phys. Rev. E*, vol. 48, pp. 2149–2156, Sep 1993.

[107] M. Abo-Bakr, J. Feikes, K. Holldack, G. Wüstefeld, and H.-W. Hübers, "Steady-state far-infrared coherent synchrotron radiation detected at bessy 2," *Phys. Rev. Lett.*, vol. 88, p. 254801, Jun 2002.

[108] Merz, M, P. Reutler, B. Büchner, D. Arena, J. Dvorak, Y.U. Idzerda, S. Tokumitsu, and S. Schuppler, "O1s and Mn2p NEXAFS on single-layered $La_{1-x}Sr_{1+x}MnO_4$ crystal field effect versus orbital coupling mechanism," *Eur. Phys. J. B*, vol. 51, no. 3, pp. 315–319, 2006.

[109] A. Oleaga, A. Salazar, D. Prabhakaran, and A. T. Boothroyd, "Critical behavior of $La_{1-x}Sr_xMnO_3$ ($\leq x \leq 0.35$) by thermal diffusivity measurements," *Phys. Rev. B*, vol. 70, p. 184402, Nov 2004.

[110] Y. Okimoto, Y. Tomioka, Y. Onose, Y. Otsuka, and Y. Tokura, "Optical study of $Pr_{1-x}Ca_xMnO_3$ in a magnetic field: Variation of electronic structure with charge ordering and disordering phase transitions," *Phys. Rev. B*, vol. 59, pp. 7401–7408, Mar 1999.

[111] M. Matsubara, Y. Okimoto, T. Ogasawara, Y. Tomioka, H. Okamoto, and Y. Tokura, "Ultrafast photoinduced insulator-ferromagnet transition in the perovskite manganite $Gd_{0.55}Sr_{0.45}MnO_3$," *Phys. Rev. Lett.*, vol. 99, p. 207401, Nov 2007.

[112] C. Stamm, T. Kachel, N. Pontius, R. Mitzner, T. Quast, K. Holldack, S. Khan, C. Lupulescu, E. F. Aziz, M. Wietstruk, H. A. Durr, and W. Eberhardt, "Femtosecond modification of electron localization and transfer of angular momentum in nickel," *Nature Mater.*, vol. 6, pp. 740–743, Oct. 2007.

[113] H. Ehrke, R. Tobey, S. Wall, S. A. Cavill, M. Frst, V. Khanna, T. Garl, N. Stojanovic, D. Prabhakaran, A. Boothroyd, M. Gensch, A. Mirone, P. Reutler, A. Revcolevschi, S. S. Dhesi, and A. Cavalleri, "Transient electronic order in photo-stimulated $La_{0.5}Sr_{1.5}MnO_4$," *Phys. Rev. Lett. submitted*, 2010.

[114] D. Polli, M. Rini, S. Wall, R. W. Schoenlein, Y. Tomioka, Y. Tokura, G. Cerullo, and A. Cavalleri, "Coherent orbital waves in the photo-induced insulator-metal dynamics of a magnetoresistive manganite," *Nature Mater.*, vol. 6, pp. 643–647, Sept. 2007.

[115] W. Ackermann and et. al., "Operation of a free-electron laser from the extreme ultraviolet to the water window," *Nature Photon.*, vol. 1, pp. 336–342, June 2007.

[116] A. L. Cavalieri, D. M. Fritz, S. H. Lee, P. H. Bucksbaum, D. A. Reis, J. Rudati, D. M. Mills, P. H. Fuoss, G. B. Stephenson, C. C. Kao, D. P. Siddons, D. P. Lowney, A. G. MacPhee, D. Weinstein, R. W. Falcone, R. Pahl, J. Als-Nielsen, C. Blome, S. Düsterer, R. Ischebeck, H. Schlarb, H. Schulte-Schrepping, T. Tschentscher, J. Schneider, O. Hignette, F. Sette, and K. Sokolowski-Tinten, "Clocking femtosecond x rays," *Phys. Rev. Lett.*, vol. 94, p. 114801, Mar 2005.

[117] F. Tavella, N. Stojanovic, G. Geloni, and M. Gensch, "Few-femtosecond timing at fourth-generation x-ray light sources," *Nature Photon.*, 2011. Private Communication.

[118] K. J. Thomas, J. P. Hill, S. Grenier, Y.-J. Kim, P. Abbamonte, L. Venema, A. Rusydi, Y. Tomioka, Y. Tokura, D. F. McMorrow, G. Sawatzky, and M. van Veenendaal, "Soft x-ray resonant diffraction study of magnetic and orbital correlations in a manganite near half doping," *Phys. Rev. Lett.*, vol. 92, p. 237204, Jun 2004.